Study of Narrow-Band Spectral Characteristics of Stimulated Electromagnetic Emission (SEE) During Second Electron Gyro-Harmonic Heating

Alireza Samimi

Dissertation submitted to the Faculty of the
Virginia Polytechnic Institute and State University
in partial fulfillment of the requirements for the degree of

Doctor of Philosophy
in
Electrical Engineering

Wayne A. Scales, Chair
Scott Bailey
Michael Ruohoniemi
Timothy Pratt
Eric R Sharpe

August 14, 2013
Blacksburg, Virginia

Study of Narrow-Band Spectral Characteristics of Stimulated Electromagnetic Emission (SEE) During Second Electron Gyro-Harmonic Heating

Alireza Samimi

(ABSTRACT)

Stimulated Electromagnetic Emissions SEEs may provide important diagnostic information about space plasma composition, energetics, and dynamics during active experiments in which ground-based high powered radio waves are transmitted into the ionosphere. The nonlinear plasma processes producing this secondary radiation are not well understood particularly for some recent observations where the transmitter (pump) frequency is near the second harmonic of the electron gyro-frequency. New, more comprehensive, experimental observations of spectral features within 1kHz of the pump wave frequency are reported here in order to begin more careful comparisons of the experimental observations and a possible theoretical underpinning which is also provided. The experimental observations typically show two distinct types of secondary radiation spectra which are a) discrete narrowband harmonic spectral structures ordered by the ion gyro-frequency, so-called stimulated ion Bernstein Scatter (SIBS) and, b) broadband spectral structure with center frequency near 500 Hz and similar spectral bandwidth named ion acoustic parametric decay (IAPD). A theoretical model is provided that interprets these spectral features as resulting from parametric decay instabilities in which the pump field ultimately decays into high frequency upper hybrid/electron Bernstein and low frequency neutralized ion Bernstein and/or obliquely propagating ion acoustic waves at the upper hybrid interaction altitude. Detailed calculations of the threshold level, growth rate, unstable wavenumber and frequency bandwidth of the instabilities are provided for comparisons with experimental observations. An assessment of the effect of the critical instability parameters are provided including pump electric field strength, proximity of the pump frequency to the electron gyro-frequency and pump electric field geometry. The model shows quite reasonable agreement with the experimental observations.

Next, a two dimensional Particle-In-Cell Monte-Carlo Collision computational model (PIC-MCC) is employed in order to consider nonlinear aspects such as 1) electron acceleration through wave-particle heating, 2) more complex nonlinear wave-wave processes and 3) temporal evolution of electron irregularities through nonlinear saturation. The simulation results show that the IB associated parametric decay is primarily associated with electron acceleration perpendicular to the geomagnetic field. More gyro-harmonic lines are typically associated with more intense heating. Heating is reduced when the pump frequency is sufficiently close to $2f_{ce}$. The IA associated parametric decay instability is primarily associated with electron tail heating along the magnetic field and heating is reduced when the pump frequency is sufficiently close to $2f_{ce}$. Characteristics of caviton collapse behavior become prevalent in this case. Results are discussed within the context of some recent experimental observations. Further discussions are provided of connections with past observed SEE spectral features and potential new diagnostic information provided by these newly categorized spectra.

Dedication

This work is dedicated to my kind parents.

Acknowledgments

I would like to express my deepest gratitude to my advisor, Dr. Wayne A. Scales, who patiently helped me throughout this research by his valuable advice, guidance and encouragement. Without his support this work would not be accomplished.

I would like to thank Dr. Paul Bernhardt, Dr. Stanley Briczinski at Naval Research Laboratory and all the people at HAARP facilities for their help in conducting the experiments and recording the data.

I thank Dr. Scott Bailey, Dr. J. Michael Ruohoniemi, Dr. Timothy Pratt and Dr. Eric R. Sharpe for serving in my advisory committee.

I thank John K. Harris for helping me to learn parallel programming and his continues support in the past four years. More than a colleague, he is a great friend.

I thank all my great friends at the Center for Space Science and Engineering Research (Space@VT) and Virginia Tech; specially my great roommate David Okoth.

I would like to express my thanks and sincere love to my parents and my brothers and sister back in my home country. Their encouragements and sincere supports are the main reason I am at the current position.

Contents

List of Figures

List of Tables

Chapter 1

Introduction

The ionosphere of Earth has been accepted as a conducting layer in the scientific community from 1901 when for the first time Marconi transmitted radio signal across the Atlantic. Radio broadcasting across the globe using the ionosphere as a reflector has grown rapidly. The high power Luxemburg radio station became operational in 1933. Then, it was reported in Eindhoven Holland that while radio receivers were tuned to Beromunster station, they could hear Luxemburg station in the background [*Tellegen*, 1933]. This phenomenon was called cross modulation. The first scientific explanation was that the high power Luxemburg station changes the density and temperature of the electrons in the ionosphere [*Bailey and Martyn*, 1934]. The modification of the electron temperature and density are proportional to the amplitude of the transmitted wave. In other words, the conductivity of the ionosphere that directly depends on the density of the electrons was proportional to the amplitude of the Luxemburg station. The signal of the Luxemburg station was AM modulated. Therefore, the amplitude of the reflected signal of Beromunster station was again AM modulated by the Luxemburg radio signal [*Bailey and Martyn*, 1934]. It was the beginning of a new era of ionospheric modification by the strong radiowaves. Since then, modification of the ionosphere was subject of many studies. There are several review papers on different aspects of the modification experiment [*Robinson*, 1989; *Leyser*, 2001; *Gurevich*, 2007]. The main theme of the ionospheric modification is that the injected electromagnetic (EM) wave exerts force on the charged particles (i.e., electrons and ions). This force accelerates the charged particles and increases their temperature. The temperature enhancement increases pressure gradient and generates depletion in the electron density [*Bernhardt et al.*, 1989a]. It may cause self focusing of the EM wave and increase the wave intensity [*Bernhardt et al.*, 1989a]. Also, the nonlinear ponderomotive force may trigger a parametric decay instability or an oscillating two stream instability [*Porkolab*, 1978] which ultimately converts the EM pump wave to new electrostatic (ES) plasma waves [*Porkolab*, 1978; *Huang and Kuo*, 1994]. The new ES waves may trap in the density cavities [*Isham et al.*, 1987]. These new ES waves increase the electron velocity and collision frequency. Acceleration of the electrons to high energies increases electron-neutral elastic and inelastic collision frequencies that may modify

the ionization ratio or produce artificial airglow [*Gustavsson et al.*, 2006; *Pedersen et al.*, 2010; *Bernhardt et al.*, 1989]. The EM pump wave also modifies the heat conduction and the diffusion process in the ionosphere [*Robinson*, 1988; 1989a, b]. Since the ionosphere is an infinite plasma medium, it is an ideal laboratory to study plasma waves and nonlinear wave-wave and wave-particle interactions. During the ionospheric heating, artificial irregularities, instabilities and airglow are generated [*Gurevich*, 2007]. Investigation of these artificial phenomena under the controlled experiments provides guidelines for understanding the physics of the natural phenomena [*Fialer*, 1974]. Furthermore, creating or ruining the ionospheric communication channels for applications such as over-the-horizon radar is another purpose of the the modification experiment [*Pedersen et al.*, 2010]. The most important factors that affect the ionospheric modification include: location of the heating facility (high power transmitter), i.e., equatorial, low, mid or high latitude region; solar activity; time of the day [*Gordon and Carlson*, 1974]; the frequency of the transmitter specifically its proximity to the harmonics of the electron gyro-frequency [*Honary et al.*, 1999; *Carozzi et al.*, 2002; *Gustavsson et al.*, 2006]; the mode of the propagation, i.e. extraordinary or ordinary transmission [*Frolov et al.*, 1999; *Gustavsson et al.*, 2009; *Hysell et al.*, 2011]; the strength of the injected wave and the angle of the propagation [*Mishin et al.*, 2001]. The main experimental observations may be divided into the following broad categories [*Robinson*, 1989; *Gurevich*, 2007; *Leyser*, 2001]:

1. Large scale plasma temperature and density changes.

2. Generation of small scale field aligned irregularities (FAIs).

3. Induced anomalous absorption of high frequency (HF) radio signals.

4. Artificially induced diffusive HF scatter (spread F).

5. Artificially stimulated scintillations.

6. Artificially enhanced airglow and particle acceleration.

7. Enhanced ion and plasma lines in the incoherent scatter radar spectra.

8. Nonlinear radio wave reflectivity and cross modulation effect.

9. Stimulated electromagnetic emission.

It is out of the scope of this dissertation to speak about all the aforementioned observations. The focus of this study is on the narrow-band spectral features of the stimulated electromagnetic emission (SEE) excited during the second electron gyro-harmonic heating.

1.1 Brief History of Ionospheric Modification Experiments

Russian scientists in 1961 started a classified project that aimed to lighten the night sky in Moscow [*Gurevich*, 2007]. The idea was to accelerate charged particles in the ionosphere to generate an artificial airglow. Although those experiments were not successful, they resulted in observing numerous new phenomena during active modification experiment. The active modification of the ionosphere opened a new window to understanding the ionosphere and the different types of irregularities that occur. In the United States, the active modification experiment started in 1970 in Platteville, Colorado. It was observed that the strong EM wave of the heater, generated artificial field aligned irregularities (FAIs) in the ionosphere. Characteristics of the artificial FAIs were similar to the natural field aligned irregularities [*Fialer*, 1974]. Thus the initial motivation of the active experiments in the USA was to study the natural FAIs by creating the artificial FAIs under the controlled experiments [*Fialer*, 1974]. It should be mentioned that the generation of the artificial FAIs was not predicted. It took a while after the experimental observations until an acceptable explanation was provided [*Grach et al.*, 1978; *Das and Fejer*, 1979].

1.1.1 Stimulated Electromagnetic Emission

Stimulated Electromagnetic Emission (SEE) is a secondary electromagnetic (EM) wave generated in the Earth's ionosphere in response to the strong high frequency (HF) electromagnetic pump wave [*Leyser*, 2001]. The SEE exhibits a frequency shift relative to the transmitter frequency. The temporal evolution and the frequency spectral characteristics of the SEE can provide diagnostic information about the ionosphere. The generation of the SEE was first predicted theoretically by *Stenflo and Trulsen* [1978]. Later *Thidé et al.* [1982] observed the SEE for the first time during the heating experiments conducted at the European Incoherent SCATter Scientific Association (EISCAT) facilitates at Tromsø Norway. Parametric decay instability of the plasma waves in the ionosphere has been introduced as a potential generation mechanism of the SEE [*Stubbe et al.*, 1984]. The general picture of the parametric decay instability is as follows: the pump EM wave with the frequency ω_0 imposes electrons to oscillate at the same frequency, the low frequency fluctuations of the ions with frequency ω_1 can beat with the oscillating electrons and generate high frequency oscillation at $(\omega_0 \pm \omega_1)$ [Porkolab, 1978]. On the other hand, the new high frequency electron wave can beat with the pump EM wave and generate low frequency oscillation at ω_1. If this positive feedback loop is large enough to overcome losses of the new low frequency and high frequency decay modes, the parametric decay instability grows [*Porkolab*, 1978; *Kou*,]. The energy of the pump wave is invested in the decay modes [*Kou*].

Figure 1.1 shows the schematic of the heating experiment during which the SEE is generated. A strong EM wave transmitted in the Ordinary mode (O-mode) contributes to the
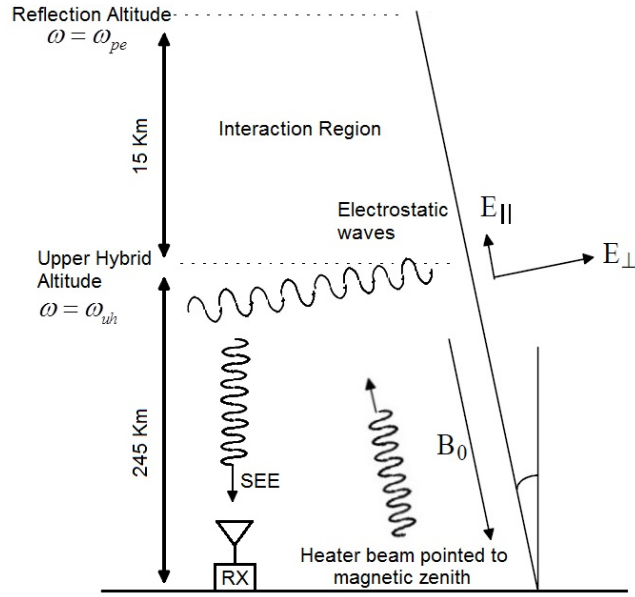
Figure 1.1: Schematic of the heating experiment resulting in generation of the stimulated electromagnetic emission. [*Hussein,* 1997]

parametric decay instability in the source region. The upper hybrid resonance altitude or the O-mode reflection altitude are suggested as the source region of the SEE [*Stubbe et al.*, 1984; *Huang and Kuo*, 1994; *Frolov et al.*, 1999]. In the O-mode transmission, the EM wave propagates across the magnetic field and its electric field component is along the background magnetic field [*Chen*, 1984]. The SEE has not been reported during extraordinary (X-mode) transmission [*Stubbe et al.*, 1984; *Leyser*, 2001]. It is observed that simultaneous transmission in the O-mode and the X-mode suppresses spectral features of the SEE [*Frolov et al.*, 1999].

Figure 1.2 shows the frequency power spectrum of the signal received from the ionosphere during heating experiment. It exhibits several classical SEE spectral characteristics. This experiment was conducted at the High Frequency Active Auroral Research Program (HAARP) facilities in the summer of 2012. The left panel shows SEE characteristics observed during the third electron gyro-harmonic heating. These SEE spectral features are: 1) a sideband at 1.5 kHz downshifted relative to the transmitter frequency called the downshifted peak (DP); 2) two sidebands at 10 kHz and 18 kHz downshifted relative to the transmitter frequency called the first and the second downshifted maximum (DM, 2DM); 3) a structure at 8 kHz upshifted relative to the transmitter frequency called upshifted maximum (UM); and 4) a very broad structure with 20 kHz bandwidth that maximizes at 20 kHz above the transmitter frequency called the broad upshifed maximum (BUM) [*Leyser*, 2001]. Note that the DM feature is associated with the artificial FAIs [*Huang and Kuo*, 1994]. The right panel shows the DM and UM with maximum at approximately ±6 kHz shift relative to the
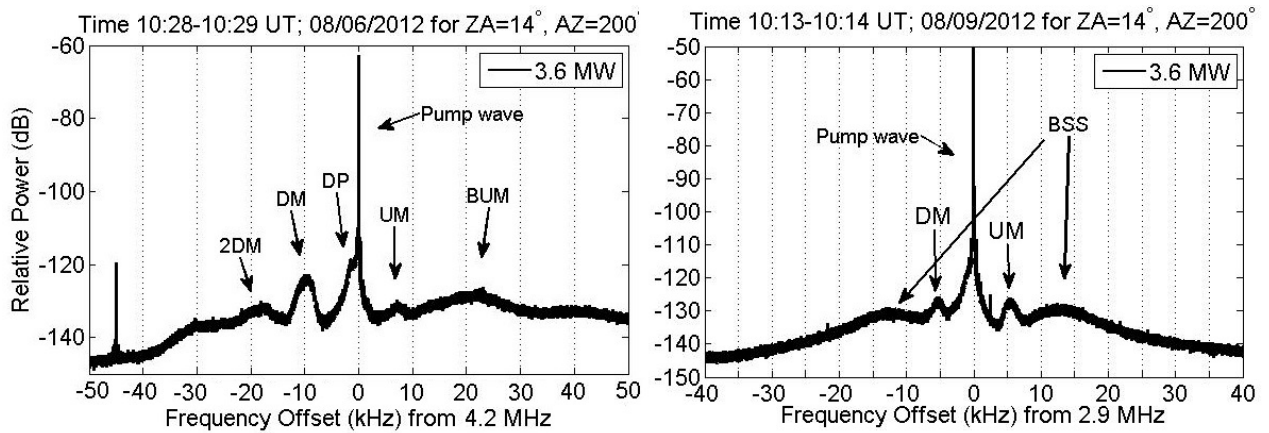
Figure 1.2: Frequency power spectrum of the SEE recorded at HAARP facilities in July 2012. The transmitter beam points toward the magnetic zenith. The left panel shows the first and second downshifted maximum (DM, 2DM), the downshifted peak (DP), the upshifted maximum (UM), the broad upshifted maximum (BUM) observed during heating near the third electron gyro-harmonic frequency. The right panel shows the DM, UM and the broad symmetric structure (BSS) recorded during heating near second electron gyro-harmonic.

transmitter frequency and another prominent SEE feature called broad symmetric structure (BSS) observed during second electron gyro-harmonic heating. The BSS consists of two broad sidebands symmetrically downshifted and upshifted relative to the pump frequency. The BSS peaks at around 14 kHz. The bandwidth of each sideband is approximately 20 kHz. The BSS appears in the power spectrum when the transmitter frequency is approximately 15 kHz - 30 kHz above the harmonics of the electron gyro-frequency in the interaction region [*Leyser*, 2001].

Figure 1.3 shows sensitivity of the classic SEE characteristics to the transmitter frequency. These frequency power spectrums were recorded during a frequency stepping experiment near the third harmonic of the electron gyro-frequency conducted at HAARP facilities in July 2011. As the transmitter frequency approaches the third electron gyro-harmonic frequency, the DM and 2DM features are suppressed. When the transmitter frequency goes above the third electron gyro-harmonic, the BUM appears in the power spectrum. This sensitivity can be used to estimate the strength of the geomagnetic field in the interaction region [*Leyser et al.*, 1992; *Leyser*, 2001]. Recently, it has been observed that heating near harmonics of the electron gyro-frequency can increase the ionization ratio and produce new ionized layers in the ionosphere below the reflection altitude. The new artificial ionospheric layers move downward. At lower altitudes electron gyro-frequency is higher. Slow upward frequency sweep helps in sustaining the artificial layers for a longer period of time [*Pedersen et al.*, 2010; 2011]. It is discovered that the BUM and a new SEE charactersic called downshifted mass (Dmass) are associated with the artificial ionospheric layers [*Grach et al.*, 2012; *Bernhardt*,

private communication, 2013]. Note that the Dmass feature observed during second electron gyro-harmonic heating is the same as the ion acoustic parametric decay (IAPD) feature that will be introduced in more detail in this study. The frequency offset of the BUM relative to the pump frequency is sensitive to the altitude of the artificial ionospheric layers [*Grach et al.*, 2012;*Bernhardt, private communication*, 2013]. Therefore, the SEE characteristics can be employed to detect the artificial ionospheric layers. These experimental observations show the critical role of the SEE as an inexpensive diagnostic tool for probing the ionosphere. Understanding the generation mechanism of the SEE features and their association with the particle acceleration can shed light on the physics of the irregularities in the ionosphere.

In general there are two kinds of contribution of the EM pump wave in the parametric decay instabilities that generate SEE. In the first kind, the electromagnetic (EM) pump wave is directly involved in the decay process and generates new EM and electrostatic (ES) waves. For example; the decay of the pump field into an ion acoustic (IA) wave and a scattered EM wave is involved in the stimulated Brillouin scatter process [*Norin et al.*, 2009]. On the other hand, for other SEE features, the EM wave undergoes conversion to another ES wave which then decays into new ES waves that are then converted back to EM waves. For instance, parametric decay of an upper hybrid/electron Bernstein (UH/EB) pump wave into another UH/EB wave and a lower hybrid (LH) wave [*Zhou et al.*, 1994; *Bernhardt et al.*, 1994] is proposed for generation of the downshifted maximum (DM) feature. The downshifted peak (DP) is considered to be generated through the decay of an electron Bernstein (EB) pump field into another EB and an IA wave [*Huang and Kuo*, 1995]. A thermal oscillating two-stream instability (OTSI) could be responsible for the conversion of the EM wave into an ES upper hybrid (UH) pump wave [*Grach et al.*, 1978; *Das and Fejer* , 1979; *Dysthe et al* , 1983; *Huang and Kuo*, 1994]. The conversion process may be followed by an explosive growth through a wave trapping process so called resonance instability [*Inhester*, 1982; *Dysthe et al* , 1982; *Vaskov and Gurevich*, 1984].

Since the ionosphere is an infinitely large medium in which a wide variety of the plasma waves can be generated and sustained, numerous SEE spectral features are expected to be seen due to the parametric decay instability. The frequency shift of the SEE depends upon the frequency proximity of the pump wave to the harmonics of the electron gyro-frequency, i.e. $n\Omega_{ce}$, the angle of the pump electric field relative to the magnetic field in the interaction region and the strength of the pump field. The pump field strength depends on the transmitter power and the absorption of the EM pump wave in the ionosphere during the experiment [*Leyser*, 2001; *Tereshchenko et al.*, 2006].

1.2   Objectives

Recent experimental observations of SEE during the second electron gyro-harmonic heating show two distinctly different but physically related spectral features which are: 1) discrete narrowband structures ordered by local ion gyro-frequency called stimulated ion Bernstein
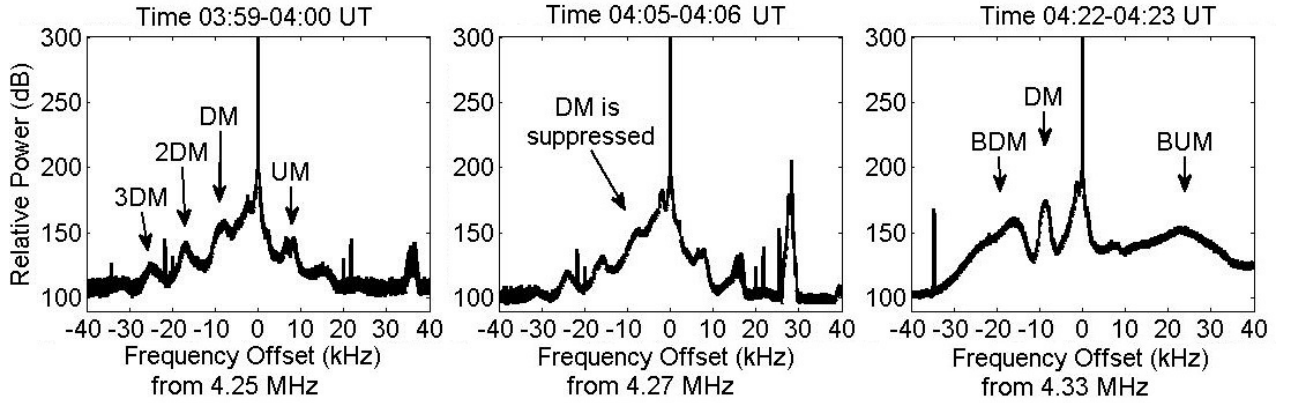
Figure 1.3: Classical SEE features, the Downshifted Maximum (DM), the Upshifted Maximum (UM), the Broad Downshifted Maximum (BDM) and the Broad Upshifted Maximum (BUM) obtained during heating near the third electron gyro-harmonic frequency. The transmitter beam points toward the magnetic zenith. Note that as the pump frequency approaches the third electron gyro-harmonic frequency, i.e. 4.28 MHz, the prominent DM feature is suppressed. The experiment conducted in July 2011 at the HAARP facility at Alaska.

scatter (SIBS) structures, 2) broadband structures that maximize around 500 Hz downshifted relative to the pump frequency called ion acoustic parametric decay (IAPD) structure [*Bernhardt et al.*, 2011; *Samimi et al.*, 2012; 2013]. The first observation of the structures ordered by the ion gyro-frequency near 45 to 50 Hz in the SEE spectrum was reported by *Thidé et al.* [1983]. These SIBS structures were observed during the extraordinary transmission (X-mode) on 2.759 MHz that is very close to the local second electron gyro-harmonic frequency. Parametric decay of the extraordinary EM wave into the UH wave and ion Bernstein (IB) was proposed for the generation mechanism of the aforementioned structures [*Sharma et al.* 1993]. However, the reported structures might be instrumental and due to the power supply modulation [*Thidé et al.*, 1983; *Bernhardt et al.*, 2011]. In Europe, the frequency of the power supply is 50 Hz. Since these SEE characteristics were observed during X mode transmission in the reported experiments, they are subject to debate. A clearer SEE spectrum containing the SIBS structures was observed during the heating in the ordinary (O-mode) transmission on 2.85 MHz [*Bernhardt et al.*, 2011]. The spectrum may show up to sixteen discrete spectral lines and is distinctly different from magnetized stimulated Brillouin scatter (MSBS) involving decay into electrostatic ion cyclotron waves in which only one spectral line downshifted by ion gyro-frequency is observed [*Bernhardt et al.*, 2009]. Brillouin scatter is an electromagnetic parametric process of direct conversion of the EM wave into the high frequency EM sideband and low frequency ES wave in the long wavelength regime ($k_\perp \rho_{ci} < 1$ where $k_\perp$ is the perpendicular wavenumber and ρ_{ci} is the ion gyro-radius). The process here, as will be discussed, involves conversion of the EM wave first into an ES upper hybrid/electron Bernstein (UH/EB) wave, then an electrostatic parametric process (short wavelength regime

$k_\perp \rho_i > 1$), and finally backscattering into the EM wave observed as SEE. Cascading during Brillioun scatter has been observed to produce additional lines (one or maximum two) but not a large number as observed in these experiments. Also, the amplitude of these lines greatly decreases with harmonic number with offset from the pump frequency unlike the observations to be described here. It should be noted that our very recent experiments show that magnetized Brillouin scatter is clearly suppressed for the pump frequency near the second gyro-harmonic (also third) while these gyro-features are enhanced, again consistent with theory [*Fu et al.*, 2013]. A more careful comparison of these two processes is beyond the scope of the this study.

Parametric decay of the EM pump wave into EB and IB in the reflection altitude has been proposed as a generation mechanism of the SIBS structures [*Bernhardt et al.*, 2011]. Neglecting the damping rates and by using an analytical expression, threshold electric field intensity required for this process was estimated to be 250 V/m [*Bernhardt et al.*, 2011].

In this study, new observations of the SIBS structures and the ion acoustic parametric decay (IAPD) feature are presented. Furthermore, experimental evidences regarding simultaneous excitation of the SIBS structures and the MSBS are provided. For the first time, temporal evolution of these structures is considered in some detail. Experimental data is provided that exhibits SIBS structures in the SEE spectrum for heating at low 0.8 MW power corresponding to 63 MW effective radiated power (ERP) at 2.80 MHz.

The objective of this study is to investigate the generation mechanism of the aforementioned narrow-band SEE characteristics in terms of the parametric decay instability. The effect of the pump field strength, the pump field frequency proximity to second electron gyro-harmonic, the angle of the pump electric field relative to the geomagnetic field on the development of the parametric decay instability is investigated in detail. Moreover, understanding the nonlinear wave-particle interactions during the development of the decay instability that generates the SEE characteristics is critical. Acceleration of the electrons may cause collisional excitation of the artificial airglow [*Bernhardt et al.*, 1989a]. It may also increase the ionization ratio of the neutral particles and generate the artificial layers. Study of the wave-particle interaction during the development of the decay instability is the first step to understand the possible association of the aforementioned phenomena. In summary, the purposes of this research are as follows:

- To provide an analytical framework to explain the generation mechanism of the newly discovered narrow-band spectral characteristics of the SEE observed during the heating near the second electron gyro-harmonic frequency.

- To provide fundamental parameters that characterize these types of spectra that may have critical diagnostic information of the heated plasma using the analytical model.

- To study the nonlinear physical processes such as 1) electron acceleration through wave-particle heating, 2) more complex nonlinear wave-wave processes and 3) temporal evolution of electron irregularities through nonlinear saturation.

This dissertation is organized as follows. In Chapter 2, the procedure of the conducted experiments are stated, then experimental observations are provided. In Chapter 3, an analytical model is used to estimate the direction and strength of the pump electric field in the interaction region. In Chapter 4, parametric decay of the pump wave into an UH/EB wave and a group of neutralized IB waves and/or an oblique IA wave is discussed as a responsible generation mechanism of the aforementioned narrow-band SEE characteristics. The impact of 1) the pump field strength, 2) the pump field frequency proximity to the electron gyro-harmonic frequency, and 3) angle of the pump field relative to the geomagnetic field on the SEE spectrum are considered. The threshold of the electric field strength is calculated and compared to the previous estimation. In Chapter 5, the computational model is presented. Association of the electron acceleration along and across the magnetic field with the IB and IA parametric decay instabilities is discussed. Sensitivity of heating to the pump frequency is investigated. In Chapter 6, summary and conclusions are provided.

Chapter 2

Experimental Observations

In the previous chapter, the stimulated electromagnetic emissions (SEEs) and some of the diagnostic information that can be obtained from them were explained. Except for the HAARP facilities, other heating facilities around the globe do not have the capability to transmit near the second electron gyro-harmonic. Therefore, the second electron gyro-harmonic heating has not been studied thoroughly. Initial experiments that were performed at Platteville Colorado in 1970 showed that the artificial field aligned irregularities (FAIs) are suppressed during heating near the third or higher harmonics of the electron gyro-frequency (i.e. $n\Omega_{ce}$ for $n \geq 3$) [*Fialer*, 1974]. In contrast, transmission near the second harmonic of the electron gyro-frequency, i.e. $2\Omega_{ce}$, results in enhancement of the FAIs [*Fialer*, 1974]. New experiments also confirm this opposite behavior of the FAIs [*Hysell and Nossa*, 2009]. Furthermore, recent experiments show that artificial airglow is enhanced during heating near $2\Omega_{ce}$. Otherwise, heating near the higher harmonics, i.e. $n\Omega_{ce}$ for $n \geq 3$, suppresses the artificial airglow [*Djuth et al.*, 2005; *Kosch*, 2007]. Therefore, the second electron gyro-harmonic heating is still subject of interest. This study is focused on the SEE characteristics within 1 kHz of the transmitter frequency observed during the second electron gyro-harmonic heating. In two consecutive summer schools at 2011 and 2012, several sets of experiments were designed and performed at the HAARP facilities at Alaska. The goal of the experiments in 2011 was to investigate the effect of the transmitter parameters such as the transmitter power, the angle of the propagation, the transmission duty cycle and the frequency proximity of the transmitter to the harmonics of the electron gyro-frequency. In 2012, in addition to the aforementioned goals, the association of the SEE characteristics, the field aligned irregularities (FAIs) and the artificial airglow were considered. Details of the procedure of all the conducted experiments are explained in Appendix A. In this chapter, only those experiments during which the SEE characteristics that are the subject of interest of this study are explained.

2.1   Experimental Procedure

A 30 m cross dipole antenna and a receiver with around 90dB dynamic range were set up by Virginia Tech and Naval Research Laboratory (NRL) 10 km South West of the HAARP site (63.09°N Lat., -145.15°E Long.) in Gakona, Alaska. The receiver uses a mixer to shift the received signal by the transmitter frequency. Then, the signal is sampled using in-phase and quadrature-phase (I and Q) technique. The sampling frequency in most of the experiments were 250 kHz. However, if the spectrum over a wider frequency range was required, this sampling frequency would be set to higher values such as 500 kHz. The spectrograph of the acquired data is calculated by utilizing the Blackman window filtering and then calculating the fast Fourier transform (FFT) of the signal. The power spectrum is calculated by taking average of the frequency components over the whole heating cycle. For the investigation of the time evolution of the frequency spectral components, the average is taken over a shorter period of time such as 5 seconds intervals. The frequency resolution of the power spectrums that exhibit discrete structures ordered at harmonics of ion gyro-frequency are 0.95 Hz. This spectral feature is called stimulated ion Bernstein scatter (SIBS). In the cases where the high frequency resolution is not required, it is reduced to 3.8 Hz. All the experiments were carried out in the O-mode transmission. Except the experiments that were designed to study the effect of the transmission beam angle on the SEE characteristics, in the all other experiments the heater beam was pointed to magnetic zenith with a zenith angle of 14 degrees and an azimuth of 202 degrees in 2011 and 200 degrees in 2012. Discrete SIBS structures in the SEE spectra were observed during the experiments that aimed to study the effect of the heating cycle and the transmitter power. These experiments were conducted in the night-time on July 21, 2011, from 10:01 UT- 11:01 UT (02:01-03:01 local time). The reflection altitude was roughly around 250 km according to the measurements of the digital ionosonde at HAARP. The geomagnetic field strength above HAARP is estimated to be $B_0 = 50524.8$ nT using the IGRF model. Correspondingly, the electron gyro-frequency is at $f_{ce} = 1.412$ MHz and ion gyro-frequency is at $f_{ci} = 48.07$ Hz. In the first 6 minutes of the experiment, the power spectrum of the received signal does not show usable SEE data. Examination of the digital ionosonde measurements shows that the ionosphere was absent from 9:30UT to around 10:05UT. In the first set of experiments the heater duty cycle was increased in 30 sec steps starting from 30 sec on-30 sec off cycle and continued to 240 sec on-240 sec off cycle. The discrete SIBS structures appeared in the spectrum of the experiments in which the heater duty cycle was more than 90 sec on-90 sec off. Furthermore, the power spectrum of the experiments with longer duty cycles shows sharper discrete structures. Although, this experiment may imply correlation between the generation of the discrete ion gyro-harmonic structures and the heater duty cycle, occasionally, the power spectrum of some of the experiments that were carried out on July 22, 2011, between 06:00 UT-07:00 UT for which the heater duty cycle was 30 sec on-60 sec off also shows sharp discrete ion gyro-harmonic structures. These structures downshifted from the heater frequency correspond to the 6th-13th harmonics of the ion-gyro frequency, respectively. Additionally, as it was mentioned before, the ionosphere was absent until around 10:05 UT. On the other hand, the

first three experiments for which the heater duty cycle was 30 s on-30 s off, 60 s on-60 s off and 90 s on-90 s off were conducted from 10:01UT-10:07UT. Thus, correlation between the heating cycle and generation of the ion gyro-harmonic structures is still not understood. It is subject to more experimental investigation in the future in order to reach a final conclusion. In addition to the aforementioned experiments, effect of the heater duty cycle on the discrete SIBS structures was examined again on July 23, 2011 from 04:36 UT-04:55 UT. Although during this experiment the ionosphere was relatively quiet and the critical frequency was around 5 MHz, but no SIBS structure was seen in the SEE spectrum. One of the SEE spectra during this experiment shows the IAPD feature that will be explained in the next section.

In the second set of experiments heater duty cycle was 120 s on-120 s off. The heater power was reduced in 1dB steps to find the threshold level for generation of SIBS structures. The minimum heater power for which the SIBS structures formed was $P_{heater} = 0.8$ MW (63 MW ERP). In order to see SIBS structures in the SEE spectrum of the experiments corresponding to low transmitter power such as 1 MW or 0.8 MW, the FFT should be taken in between transients produced by the HAARP transmitter at turn on and turn off. Occasionally, during another experiment that was initially designed to study the spectrum of the magnetized stimulated Brillouin scatter (MSBS), the broadband spectral feature with embedded discrete ion gyro-harmonic structure was observed. Further details of this experiment are presented in the next section.

2.2 Experimental Results

2.2.1 Stimulated Ion Bernstein Scatter (SIBS) Feature

Spectra showing the discrete structures ordered by ion gyro-frequency so called stimulated ion Bernstein scatter (SIBS) structures were obtained during the experiments conducted on July 21, 2011 from 10:11 UT-11:01 UT. Figure 2.1 shows the power spectrum of the acquired signal for $P_{heater} = 1.4$ MW (111 MW ERP), $P_{heater} = 0.8$ MW (63 MW ERP)and $P_{heater} = 0.4$ MW (31 MW ERP), respectively. The heater duty cycle was 120 s on-120 s off. The transmitter frequency was tuned near the local second electron gyro-harmonic at $f_{heater} =$2.8 MHz. The SIBS structures are weaker at the lower heater power and the threshold is $P_{heater} \cong 0.8$ MW. The observed structures are shifted below the pump frequency by approximately half harmonics of the ion gyro-frequency. This leads us to believe that the structures are produced by a parametric decay process involving neutralized ion Bernstein waves as will be described later. Figure 2.2 shows the power spectrum taken over 5 s intervals during the heating process in which the heater power was 1.4 MW. This provides the temporal evolution of the spectrum. The corresponding spectrogram is shown in Figure 2.3. Almost all the SIBS structures appear above the noise level of the spectrum approximately 6 s after the heater was turned on. Thus, it can be inferred that the pump field decays into different
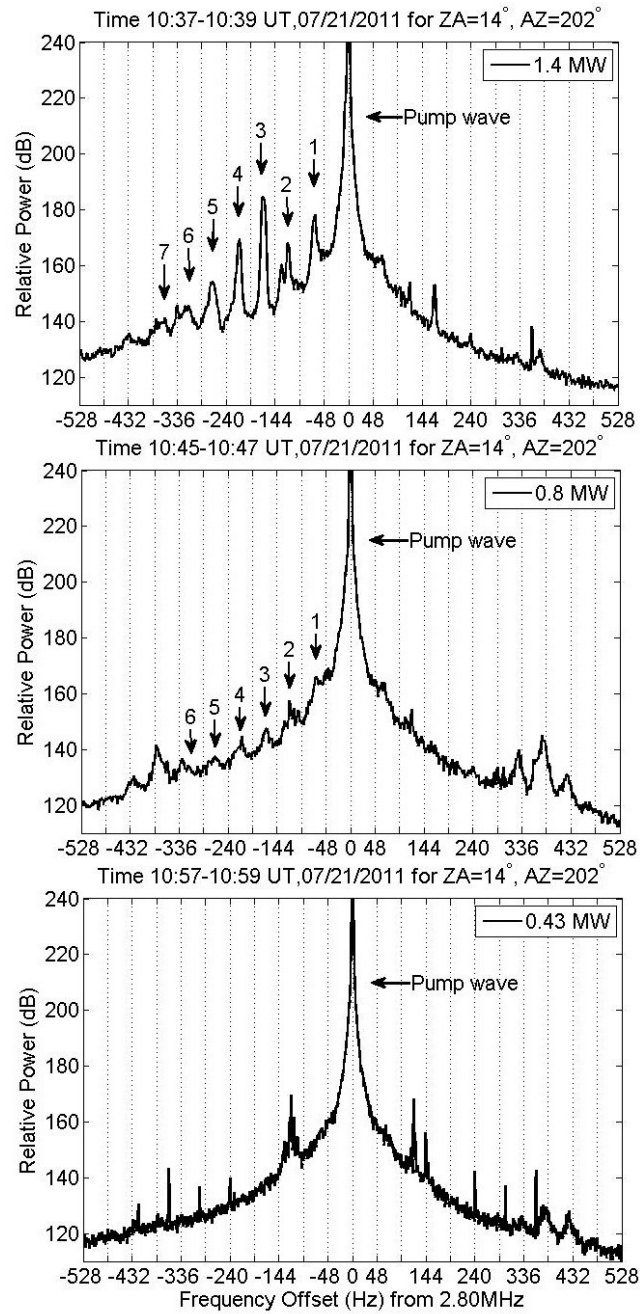
Figure 2.1: SEE spectra recorded at HAARP showing SIBS structures for $P_{heater} = 1.4$MW, $P_{heater} = 1.0$MW, $P_{heater} = 0.43$MW. Heater duty cycle was 120 s on 120 s off. The power spectrum in the bottom panel corresponding to $P_{heater} = 0.43$MW does not show SEE feature indicating heater power is below the threshold level. The heater frequency was tuned to 2.80 MHz, close to the local second electron gyro-harmonic frequency. Dotted lines are at the ion gyro-frequency. Note that the SIBS structures are downshifted relative to the pump frequency.

neutralized IB modes simultaneously. Note that the 3rd, 4th and 5th structures have the fastest growth rate respectively.

The SIBS structures were observed during the third electron gyro-harmonic heating as well [*Mahmoudian et al.*, 2013]. The SIBS structures observed during $3\Omega_{ce}$ heating are upshifted relative to the transmitter frequency. The focus of this study as it was stated before, is on the characteristic of the SIBS structures excited during $2\Omega_{ce}$ heating. However one example of the experimental observation of the SIBS structure is presented here because of the useful information that can be inferred from it.

Figure 2.4 shows two power spectra with different bandwidth for $f_0 = 4.2$ MHz and $P_{heater} = 3.6$ MW. The left panel shows the SEE characteristics within 50 kHz of the transmitter frequency and the right panel shows SEE features within 500 Hz of the transmitter frequency. Both of the spectra are from same experiment and same time. This experiment was conducted on August 6, 2012 at 10:28 UT. The reflection altitude was near 350 km. The heater was on for 60 s and then the frequency was swept continuously with the FM modulation over a 240 s period. The discrete SIBS structures that are clearly shown in the right panel, were observed during the first minute of the experiment. The SIBS structures are upshifted relative to the pump frequency. In addition to the discrete SIBS structures, the power spectrum (left panel) exhibits all the classic SEE characteristics: the downshifted peak (DP), Downshifted Maximum (DM), second Downshifted Maximum (2DM) and the Broad upshifted Maximum (BUM). It implies that all these spectral features have same source. The theoretical explanations for generation of these SEE characteristics consider electrostatic (ES) upper hybrid/electron Bernstein (UH/EB) wave as the pump wave [*Huang and Kuo*, 1994 a, b; *Zhou et al.*, 1995]. The UH/EB wave as mentioned before is generated by the thermal oscillating two stream instability (OTSI) and producs FAIs in the interaction region that are detectable by the coherent scatter radar [*Grach et al.*, 1978; *Das and Fejer* , 1979; *Dysthe et al* , 1983; *Huang and Kuo*, 1994].

2.2.2   Ion Acoustic Parametric Decay (IAPD) Feature

In addition to the discrete stimulated ion Bernstein scatter (SIBS) structures, occasionally a broadband spectral feature was observed within 1 kHz of the pump frequency during the heating experiments near the second electron gyro-harmonic frequency. Due to the physics of the generation mechanism, this spectral characteristic will be called ion acoustic parametric decay (IAPD) feature. The IAPD feature may be observed alone or with embedded discrete SIBS structures. Figure 2.5 shows the broadband feature for the experiment in which the heater was transmitting only for 22 s at $f_{heater} = 2.85$ MHz on 23 July 2011. The IAPD feature appeared in the power spectrum immediately after the heater turn-on. According to the digital ionosonde data, the reflection altitude was 160 km. The IAPD feature peaks at -436.7 Hz downshifted from the pump frequency. Furthermore, an upshifted broadband sideband peaks at +432 Hz, but weaker than the downshifted one, is also distinguishable.
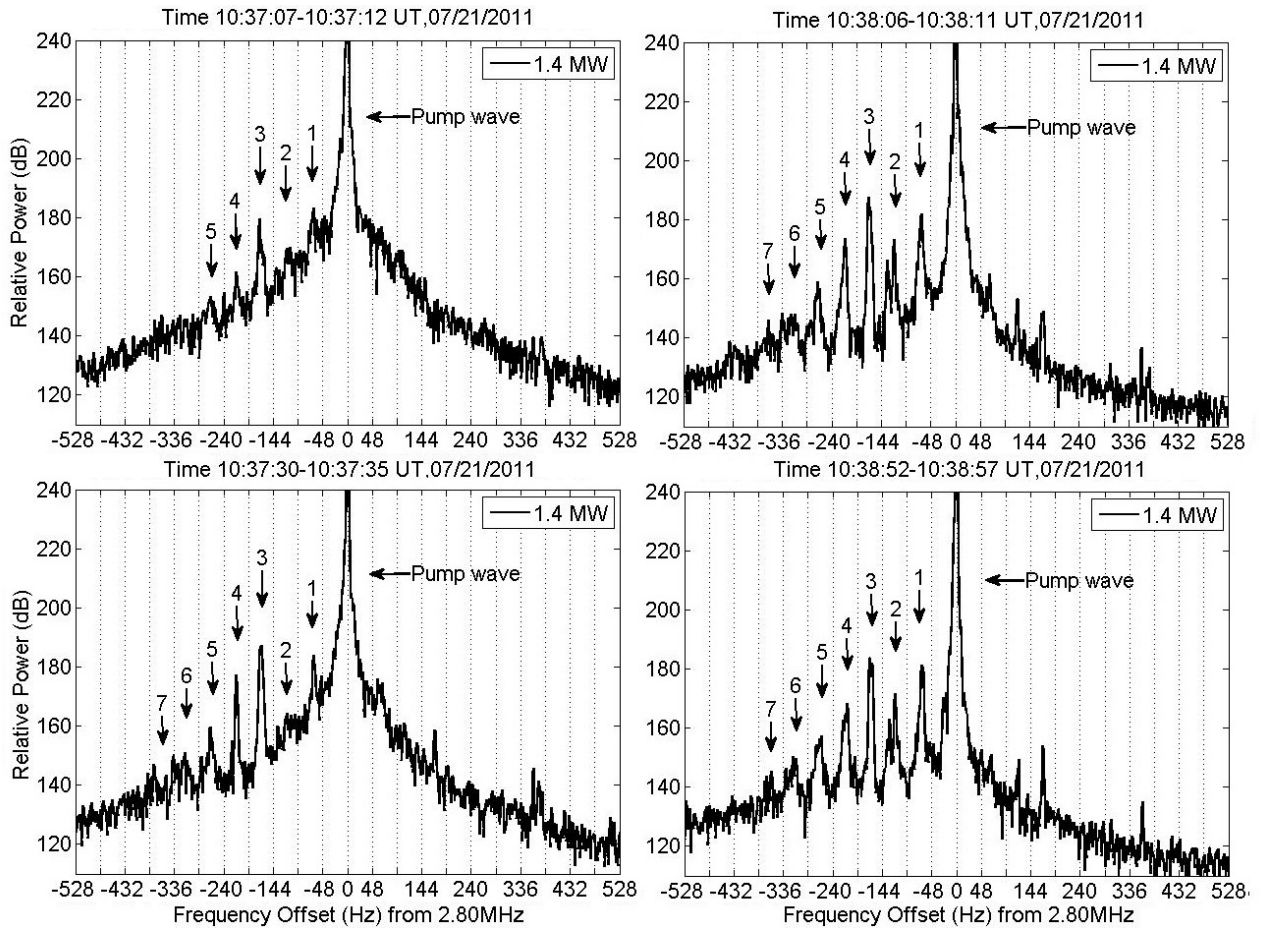
Figure 2.2: SEE spectra taken over 5 s intervals during 120 s heating demonstrates temporal evolution of the SIBS structures. Note structures start to appear above the noise level approximately 6 s after the heater turn-on. Dotted lines are at the ion gyro-frequency. Note that the 3rd, 4th and 5th have the fastest growth initially; and all the SIBS structures are downshifted relative to the pump frequency.
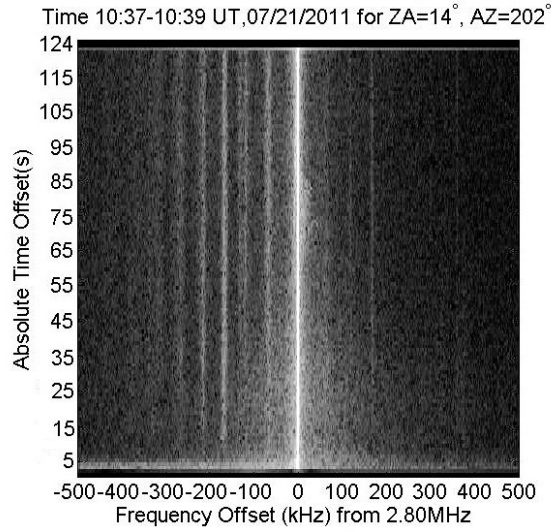
Figure 2.3: Spectrograph of the SEE structures in Figure 2.2. The strong line in the center with zero frequency offset is the pump wave and the discrete ion gyro-harmonic structures are downshifted relative to the pump frequency.
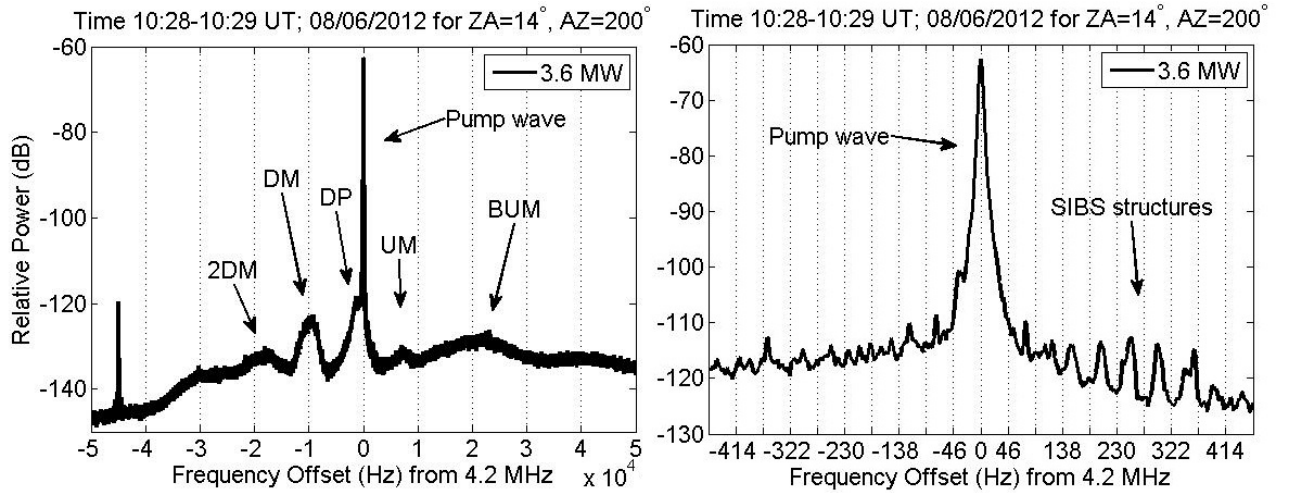
Figure 2.4: The SEE spectral features observed when the transmitter frequency is near third electron gyro-harmonic. The left panel shows the first and second downshifted maximum (DM), the downshifted peak (DP), the upshifted maximum (UM), the broad upshifted maximum (BUM). The right panel shows upshifted stimulated ion Bernstein scatter (SIBS) structures. Note that the reflection altitude at this time was 350 km and the corresponding local ion gyro-frequency $f_{ci} = 46$ Hz.
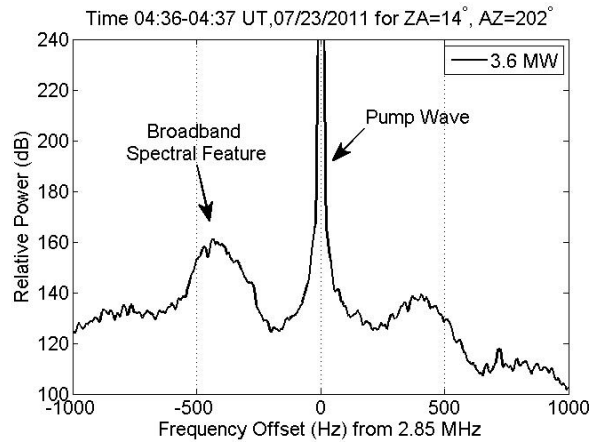
Figure 2.5: Experimental observation of the IAPD spectral feature during which the heater frequency was 2.85 MHz and heating cycle was 22 s. Note that the IAPD feature is downshifted relative to the pump frequency.

A second broadband spectral feature which peaks at ±797 Hz on both sides of the heater frequency is also observed. Similarly, the downshifted sideband is stronger than the upshifted counterpart. Figure 2.6 displays the first downshifted IAPD spectral feature with embedded discrete SIBS structures corresponding to the 8th-10th harmonics of the ion gyro-frequency. The IAPD feature peaks at -450 Hz relative to the pump frequency and seems to form right after the turn-on. The second downshifted broadband feature is also recognizable. This experiment was conducted on 22 July 2011 in which the heater cycle was 30 s on at f_{heater} = 2.77 MHz. The reflection altitude was estimated to be 210 km. The ion gyro-frequency is estimated f_{ci} =48.9 Hz. It should be noted that at the time of this experiment, the ionosphere was almost absent and the digital ionosonde does not give accurate estimation of the reflection altitude. In this experiment, the first upshifted IAPD feature is very weak and the second one does not exist.

2.2.3   Possible Connection with Magnetized Stimulated Brillouin Scatter (MSBS)

During the power stepping experiment conducted on 21 July 2011, in addition to the discrete SIBS structures, another spectral line approximately 57 Hz downshifted relative to the pump field was observed for $P_{heater} \geq 1.8$ MW. The characteristics of this spectral line are distinctly different from the SIBS structures. The threshold transmitter power that was required to generate this emission line was almost by a factor of two higher than the threshold level of the SIBS structures. Its amplitude is noticeably larger. Its bandwidth is relatively narrower. It develops a few seconds later than other structures and its growth rate is faster. It usually
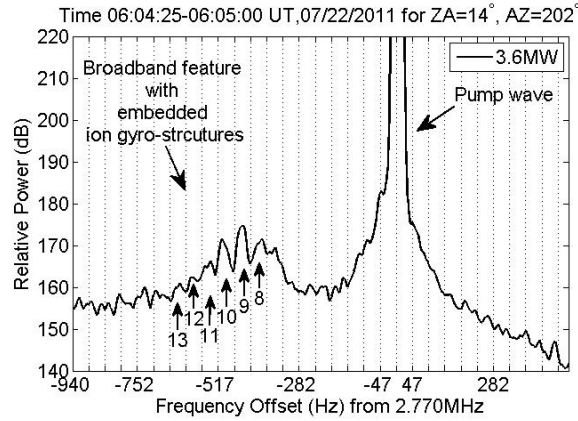
Figure 2.6: Experimental observations of IAPD feature with embedded SIBS structures during which the heater frequency was 2.77 MHz and heating cycle was 30 s. Dotted lines are at the ion gyro-frequency. Note that the spectral features are downshifted relative to the pump frequency.

damps out after a few tens of seconds. Figure 2.7 shows the high resolution power spectrum for $P_{heater} = 1.8$ MW (143 MW ERP), $P_{heater} = 1.4$ MW (111 MW ERP) and $P_{heater} = 0.4$ MW (31 MW ERP) respectively. Note only the SIBS structure of the previous figures is observed for $P_{heater} = 1.4$ MW. Both spectral features can be seen for $P_{heater} = 1.8$ MW. The frequency resolution of the power spectrum was increased to 0.48 Hz (i.e., Fourier transform was taken over a longer period of time) to distinguish the first two spectral lines. Furthermore, the power spectrums were taken over a time interval from a few seconds after the transmitter turn-on to a few seconds before the turn-off. The heater duty cycle was 120 s on and 120 s off. The power spectrums of the SEE for transmission powers higher than $P_{heater} = 1.8$ MW are similar indicating that the threshold for both spectral features has been exceeded. Figure 2.8 is the spectrogram of the SEE acquired for $P_{heater} = 2.33$ MW (229 MW ERP). It is one of the best examples that clearly demonstrates growth and decay of the narrow spectral line near f_{ci}. This emission line is 57 Hz downshifted relative to the pump. The stronger amplitude of this spectral line relative to the all other discrete SIBS structures may imply direct involvement of the EM pump wave in the magnetized stimulated Brillouin Scatter (MSBS) process. In other words, the pump EM wave directly decays to an ES low frequency decay mode and a backscattered EM wave. By comparing the acquired power spectrums with the previous experimental observations of the MSBS emission lines [*Bernhardt et al.*, 2010], it may be inferred that the low frequency decay mode is electrostatic ion cyclotron (EIC) wave. Further comments will be made on this shortly.

Figure 2.8 also shows that the second broader spectral line, very close to the first one, appears in the spectrogram earlier after the transmitter turn-on. This second spectral line with approximately 67 Hz frequency shift relative to the pump frequency is of course the first of the ion gyro-harmonic structures as in the previous data figures.
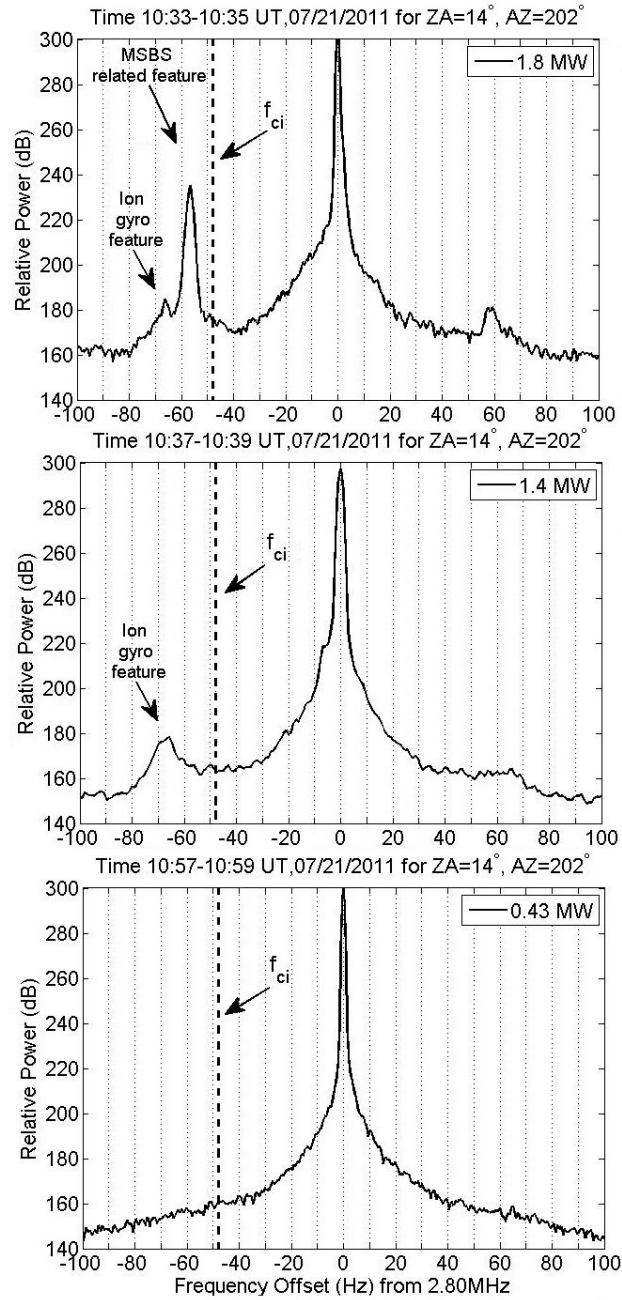
Figure 2.7: Possible experimental observation of the electrostatic ion cyclotron (EIC) emission line, downshifted relative to the pump frequency, generated through MSBS and the first mode of the discrete ion gyro-harmonic structures shown in Figure 2.1. The heater frequency was 2.8 MHz and transmitter beam points to the magnetic zenith. Note that threshold level of the narrow emission line is near 1.8 MW which is by a factor of two higher than the threshold level of the ion gyro-harmonic structures (near 1.4 MW).
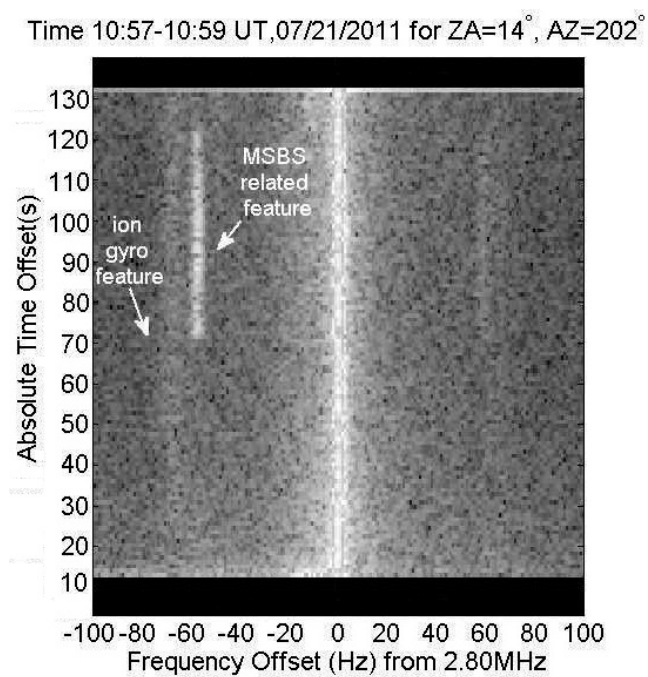
Figure 2.8: The Spectrogram of the SEE for $P_{heater} = 2.33$ MW. It clearly shows that the first spectral line develops late and damps out around 15 s before the heater turn-off. Its bandwidth is narrower than other structures.

2.2.4 Summary

In this chapter, experimental observations of the SIBS structures, the IAPD structure and the IAPD structure with embedded SIBS structures are provided. The experimental observations imply that the growth rate of the IAPD feature is faster than the SIBS structures. All the SIBS structures start to appear in the power spectrum at the same time which implies simultaneous generation rather than cascading. The growth rate of the 3rd, 4th and 5rd SIBS structures are faster than the rest of the structures. The threshold excitation transmitter power for SIBS structures was estimated to be $P_{heater} = 0.8$ MW. Furthermore, a new spectral line at 57 Hz downshifted relative to the transmitter frequency (slightly less than the frequency shift of the first SIBS structure), was reported during heating $P_{heater} \geq 1.8$ MW. The amplitude of this new spectral line is stronger than the SIBS structures and its bandwidth is narrower. This spectral line may be produced through the magnetized stimulated Brillouin scatter (MSBS) process.

Chapter 3

Wave Propagation in the Ionosphere

There are two fundamental types of the electromagnetic waves (EM) in plasma and ionosphere that propagates across the magnetic field: the ordinary wave is called O-mode and the extraordinary wave is called X-mode [*Chen*, 1984]. In the O-mode propagation, the electric field is along the magnetic field while in the X-mode propagation, it is perpendicular to the magnetic field. Equation 3.1 and 3.2 describe dispersion relation of the O-mode and the X-mode respectively [*Chen*, 1984].

$$\omega^2 = \omega_{pe}^2 - c^2 k^2 \tag{3.1}$$

$$\frac{c^2 k^2}{\omega^2} = 1 - \frac{\omega_{pe}^2}{\omega^2} \frac{\omega^2 - \omega_{pe}^2}{\omega^2 - \omega_{UH}^2} \tag{3.2}$$

where k is wavenumber, ω is the wave angular frequency, ω_{pe} is the electron plasma angular frequency and ω_{UH} is the upper hybrid angular frequency. The O-mode has one cutoff frequency at $\omega = \omega_{pe}$ and the X-mode has two cutoff frequencies obtained from Equation 3.3 [*Chen*, 1984].

$$1 - \frac{\omega_{pe}^2}{\omega^2} = \pm \frac{\Omega_{ce}}{\omega} \tag{3.3}$$

where Ω_{ce} is the electron cyclotron angular frequency. Note that because of the variable electric permittivity (due to variable electron density), the direction of the propagation and the direction of the electric and magnetic components of the pump EM is changing while it propagates in the ionosphere. Thus, in the ionosphere, the O-mode and X-mode are defined according to the direction of the electric field at the reflection altitude. Figure 3.1 shows how the O-mode and the X-mode propagate in the ionosphere at high latitudes. According to the theoretical investigations, the SEE source region is either the upper hybrid resonance altitude or the O-mode reflection altitude. As can be seen in Figure 3.1, the X-mode wave

reflects below the upper hybrid resonance altitude. Therefore, it is clear why the SEE and other phenomena such as the FAIs and airglow are not observed during X-mode propagation.

The generation mechanism of the stimulated ion Bernstein scatter (SIBS) structures is proposed as a three-step process. First the EM pump field is converted to an ES UH/EB wave. A thermal oscillating two stream instability (OTSI) (also called thermal parametric instability) that may be followed by the resonance instability is known as the conversion mechanism that creates field aligned irregularities (FAIs) in the interaction region [*Grach et al.*, 1978; *Das and Fejer* , 1979; *Dysthe et al* , 1983; *Huang and Kuo*, 1994; *Inhester*, 1982; *Dysthe et al* , 1982; *Vaskov and Gurevich*, 1984]. In the next step, as will be discussed in the next section, the ES UH/EB wave decays into another ES UH/EB mode and several neutralized IB modes or an oblique ion acoustic (IA) wave. In the last step, the newly generated ES UH/EB mode which exhibits frequency shift equal to the frequency of the neutralized IB or oblique IA decay modes (matching condition) is back converted to the EM wave. It is important to estimate the electric field strength in the interaction region (upper hybrid altitude) to access the viability of generation of the OTSI. In the ionosphere the refractive index is a function of height. Thus, the ionosphere is modeled as a horizontally stratified medium. By considering cold plasma approximation and using fluid equations in which the electrons are moving and ions are motionless background particles, the refractive index is approximated by

$$
\begin{aligned}
n_{O/X}^2 \;=\; & 1 - \frac{X}{2D}\Big\{2(1+iZ)(1+iZ-X) - Y^2\sin^2\theta \\
& \mp [Y^4\sin^4\theta + 4(1+iZ-X)^2 Y^2\cos^2\theta]^{1/2}\Big\}
\end{aligned}
\tag{3.4}
$$

where O and X in the subscript represent ordinary and extraordinary modes, $X = \omega_{pe}^2/\omega^2$, $Y = \Omega_{ce}/\omega$, $Z = \nu/\omega$, ν is the electron neutral collision frequency, and θ is the magnetic dip angle. D is defined

$$
D = [1+iZ-X]\{[1+iZ]^2 - Y^2\} - XY^2\sin^2\theta
\tag{3.5}
$$

Exact EM wave equations in the ionosphere were derived by *Försterling* [1942]. It is shown that in a slowly varying medium, Förstrling equations for the ordinary mode can be simplified into [*Budden* 1966]

$$
\frac{\partial F_O}{\partial z} + k^2 n_O^2 F_O = 0
\tag{3.6}
$$

The electric field in the ionosphere is given by

$$
E_O = (\rho_X, 1, \rho_X\rho_{L,O})F_O/\sqrt{\rho_X^2 - 1}
\tag{3.7}
$$

where

$$
\begin{aligned}
\rho_{O/X} \;=\; & \frac{i}{2(1+iZ-X)Y\cos\theta}\Big\{Y^2\sin^2\theta \\
& \pm [Y^4\sin^4\theta + 4(1+iZ-X)^2 Y^2\cos^2\theta]^{1/2}\Big\}
\end{aligned}
\tag{3.8}
$$
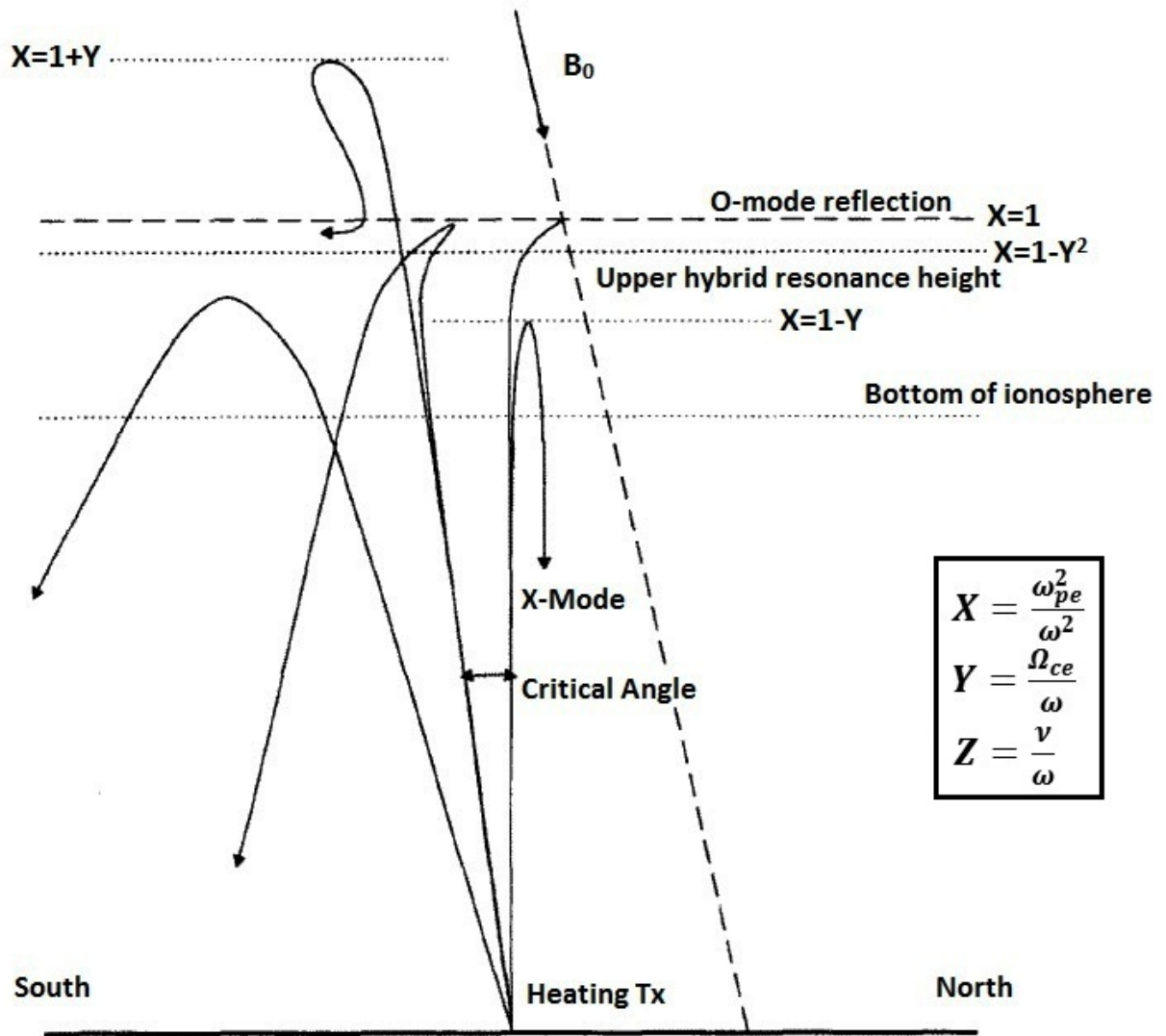
Figure 3.1: Scehmatic of X-mode and O-mode wave propagation in the ionosphere. [*Rietveld et al.*, 1993]
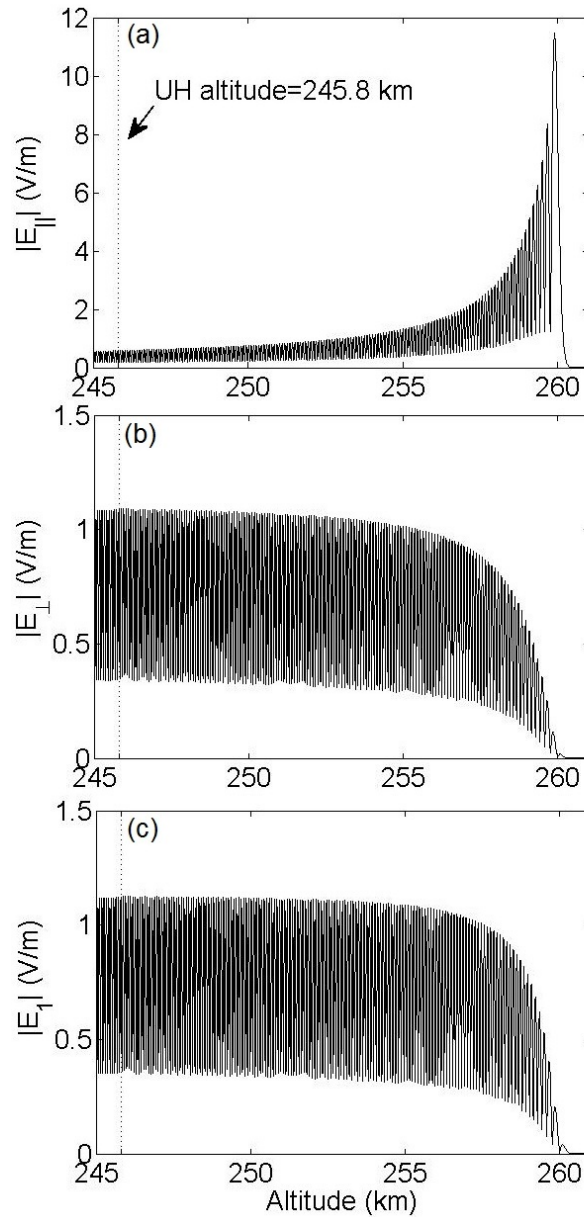
Figure 3.2: The electric field amplitude a) along the magnetic field, $E_\parallel$, b) perpendicular to the magnetic field, $E_\perp$, and c) the east-west component E_1. The transmission frequency is 2.8 MHz and the magnetic dip angle is assumed to be 14°. The bottom of the ionosphere (reference point) is assumed to be at z=200 km in which the electric field intensity 1 V/m is considered. The ionosphere density is estimated according to the digital ionosonde evaluation on July 21, 2011 during which the discrete SIBS structures are observed

and

$$\rho_{L,O} = \frac{iY \sin\theta}{1 + iZ - X}(n_O^2 - 1). \tag{3.9}$$

All these equations can be found in *Lundborg and Thidé* [1985,1986]. Far from the reflection altitude, the WKB method can be used to calculate the electric field with an acceptable approximation. However, close to the reflection altitude, the uniform approximation method provides a more precise solution to the wave equation. Details of this method can be found in the two consecutive papers by *Lundborg and Thidé* [1985,1986]. We employed the uniform approximation method to estimate the electric field strength and its direction in between the upper hybrid and the reflection altitude. Since the heater frequency is far below the critical frequency, the monotonically increasing electron density model is used. The digital ionosonde data is used to approximate the electron density profile. Two cases are considered. The first case corresponds to the nighttime experiment on July 2011 during which the discrete SIBS structures are observed. The second case the electric field is evaluated during the daytime experiment on July 23, 2011 when the IAPD structure is observed. The ionosphere profiles are obtained from Figure A.1 (Appendix A). Figure 3.2 displays results of the first case. The upper hybrid altitude z_{uh} =245.8 km and the reflection altitude $z_{reflection}$ =260 km. The electric field intensity at the reference point is 1 V/m. The reference point is chosen at z_r =200 km using the digital ionosonde estimation of the F layer profile. According to this calculation, the relative intensity of the perpendicular electric field in the upper hybrid altitude is 1.08 V/m and the parallel component is 0.58 V/m, thus, the electric field is 28.2° off-perpendicular to the geomagnetic field in the upper hybrid altitude. The relative intensity of the total electric field in the upper hybrid altitude is $|E_{UH}|/|E_{z=200km}|$ =1.67 V/m. On the other hand, slightly below the reflection altitude, at z =259.9 km, intensity of the perpendicular electric field is 0.08 V/m and the parallel component is 11.47 V/m, therefore, the electric field is parallel to the geomagnetic field. If we assume that the bottom of the ionosphere is at the reference point which is z =200 km, the electric field intensity in the upper hybrid altitude is $|E| = 1.67\sqrt{\eta_0 PG/4\pi z^2}$ where η_0=377Ω is the impedance of free space, P is the heater power and $G = 19$ dB is the antenna gain [*Bernhardt et al.*, 2011]. The electric field intensity at the upper hybrid altitude corresponding to $P_{heater} = 0.8$ MW and $P_{heater} = 3.6$ MW are $|E|$ =0.36 V/m and $|E|$ =0.77 V/m, respectively.

Results of the second case are shown in Figure 3.3. In this case according to the digital ionosonde data (i.e. bottom panel of Figure A.1 of Appendix A), the E layer is formed. The electron neutral collision frequency in the E layer is higher than the F layer that increases the attenuation of the EM pump wave. For simplicity we considered same electron-neutral collision frequency ($\nu_e = 400 \ s^{-1}$) for the both E and F layer. The reference point is approximated at z_r =80 km, the upper hybrid altitude z_{uh} =139.2 km and the reflection altitude is approximately $z_{reflection}$ =150 km. The relative intensity of the perpendicular electric field in the upper hybrid altitude is 0.32 V/m and the parallel component is 0.24 V/m, thus, the electric field is 36.8° off-perpendicular to the geomagnetic field in the upper hybrid altitude. The relative intensity of the total electric field in the upper hybrid altitude

is $|E_{UH}|/|E_{z=80km}|$ =0.52 V/m. Similar to the previous case, slightly below the reflection altitude, at z =149.9 km, the electric field is along the magnetic field and the intensity of the perpendicular electric field is 0.04 V/m and the parallel component is 7.4 V/m. In this case the electric field intensity at the upper hybrid altitude for the full power heating, i.e., P_{heater} = 3.6 MW is $|E| = 0.52\sqrt{\eta_0 PG/4\pi z^2} = 0.6V/m$. Note that although the reflection altitude is around 100 km lower than the previous case, since the ionosphere is denser during the daytime, 1) the electric field is more off-perpendicular to the geomagnetic field in comparison to the previous case; 2) the intensity of the electric field is also less than the former case. Therefore, it is more difficult to exceed the threshold excitation level during the daytime experiment. The next question is if the estimated electric field intensities are strong enough to excite the OTSI or thermal parametric instability (TPI). The OTSI and the TPI terminologies are used interchangeably in the manuscripts. We will use same terminology that each author has used. Previous studies of the OTSI shows that the threshold level could be as low as $|E|$ =0.1 V/m [*Huang and Kuo* 1995]. *Grach* [1979] theoretically showed that below the reflection altitude the threshold electric field intensity required to excite the TPI near $2\Omega_{ce}$ is less than near higher harmonics, i.e. $n\Omega_{ce}$ for $n \geq 3$. This prediction is consistent with the experimental evidences that for second electron gyroharmonic heating, FAIs are stronger than for higher gyro-harmonics [*Fialer*, 1974; *Djuth et al.*, 2005; *Kosch*, 2007; *Hysell and Nossa*, 2009]. Since FAIs are generated by the TPI, it implies that the threshold electric field intensity may be even lower than $|E|$ =0.1 V/m near $2\Omega_{ce}$. Note that excitation of the TPI affects the electric field intensity above the upper hybrid altitude. This effect is not considered in the current calculations. Furthermore, the attenuation of the EM wave in the D region is neglected in the calculations.

3.1   Summary

In this chapter, X-mode and O-mode propagation in the ionosphere were discussed very briefly. The strength and direction of the O-mode pump electric field in between the upper hybrid resonance altitude and the reflection altitude were estimated. The ionosphere profile that was used in the calculations was obtained from the digital ionosonde data recorded at HAARP during the time periods over which the SIBS and IAPD SEE features were observed. It was shown that at the upper hybrid layer, the pump electric field is almost perpendicular to the magnetic field. Comparison of the results of the calculation of the electric field direction showed that the electric field is closer to perpendicular to the geomagnetic field when the SIBS is observed.
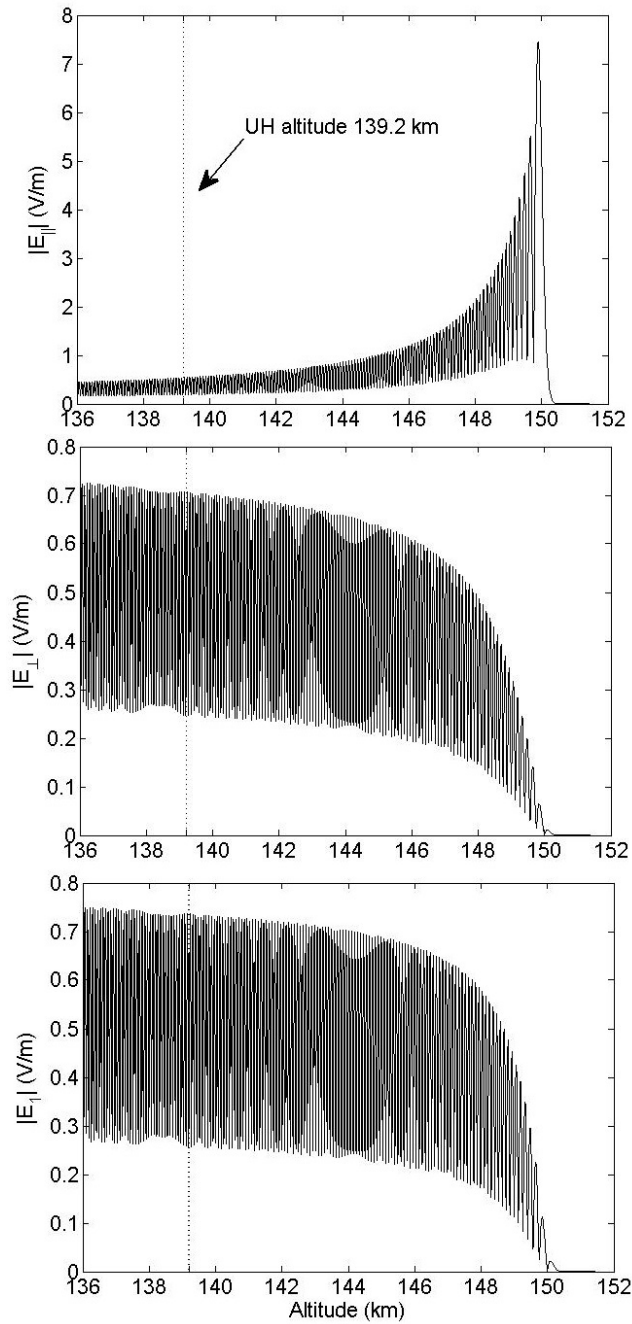
Figure 3.3: The electric field amplitude a) along the magnetic field, $E_{\|}$, b) perpendicular to the magnetic field, $E_{\perp}$, and c) the east-west component E_1. The transmission frequency is 2.85 MHz and the magnetic dip angle is assumed to be $14°$. The bottom of the ionosphere (reference point) is assumed to be at z=80 km in which the electric field intensity 1 V/m is considered. The ionosphere density is estimated according to the digital ionosonde evaluation on July 23, 2011 during which the IAPD structures are observed

Chapter 4

Theory

Parametric decay instability is a wave coupling process in which a pump wave decays into two new wave modes with new frequencies and wavenumbers. The wavenumber and frequency of the pump wave and the decay products match in the parametric instability, i.e.,

$$\overrightarrow{k_0} = \overrightarrow{k_1} + \overrightarrow{k_s}$$
$$\omega_0 = \omega_1 + \omega_s \tag{4.1}$$

where subscripts 0, 1 and s represent parameters of the pump field, the high frequency decay mode and the low frequency decay mode respectively. The matching condition is equivalent to the conservation of momentum and energy [*Chen*, 1984]. Note that the frequency and wavenumber of each decay mode is related by the dispersion relation. Figure 4.1 shows a diagram of the parametric decay instability in which the pump wave is an upper hybrid wave. The high frequency decay mode is another UH wave. The low frequency mode is an ion acoustic wave. Natural ion fluctuations oscillating at ω_s beat with the electrons that are oscillating at the pump wave frequency (ω_0) and excite new high frequency electron wave at $\omega_0 - \omega_s$. The new electron wave beats with the pump wave and generates a low frequency wave at ω_s. A positive feedback loop is formed. If the feedback is large enough, the parametric decay instability grows exponentially [*Porkolab*, 1978]. Parametric decay instability is explained in detail in Appendix B using the fluid model and more complicated kinetic equations in the magnetized plasma. Here, the generation mechanism of the narrow-band SEE characteristics that were introduced in Chapter 2 is explained in terms of the parametric decay instability. The effects of the pump field frequency proximity to the second electron gyro-harmonic, the pump field strength, the angle of the pump electric field vector and the angle of propagation of the decay products are investigated in detail. The minimum electric field intensity required for development of the process is estimated.

Parametric decay of the UH/EB pump wave into another UH/EB and neutralized IB wave has been introduced as a viable process for generation of the SIBS structures [*Scales et al.*, 2011]. The neutralized ion Bernstein wave propagates slightly off-perpendicular to the
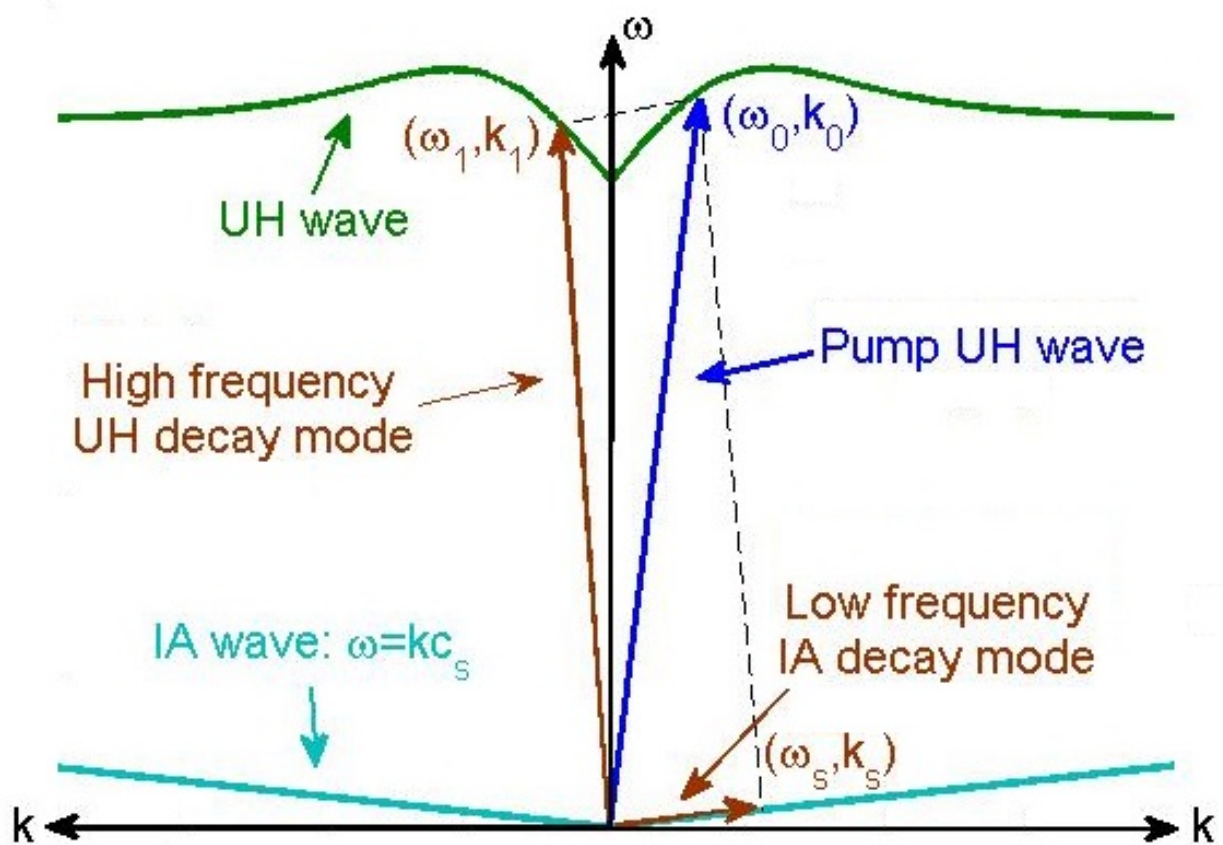
Figure 4.1: Diagram of the parametric decay of an upper hybrid pump wave into another upper hybrid and an ion acoustic wave.

background magnetic field exhibiting Boltzmann (neutralizing) electron behavior along the magnetic field and has different dispersive properties to the pure Bernstein mode which propagates exactly perpendicular to the magnetic field [*Chen*, 1984]. The other low frequency decay mode may also be an oblique ion acoustic (IA) wave for the IAPD spectral feature. It should be noted that the neutralized IB and IA modes are intimately related in the sense that the mode surfaces are connected at oblique angles (e.g. *Kindel and Kennel* [1971], and *André* [1985]). This fact is critical in interpretation of some of the SEE spectral structure. By enforcing wavenumber and frequency matching conditions (Equation 4.1), the general dispersion relation describing weak coupling is [*Porkolab*, 1974]

$$\varepsilon(\omega_s) + \frac{\beta_e^2}{4}\chi_i(\omega_s)\left\{\frac{\varepsilon_e(\omega_s)}{\epsilon_e(-\omega_1^*)} - 2\right\} = 0 \tag{4.2}$$

where $\varepsilon(\omega) = 1 + \chi_e(\omega) + \chi_i(\omega)$, and $\varepsilon_e(\omega) = 1 + \chi_e(\omega)$. The susceptibility of the jth species is given by

$$\chi_j(\omega) = \frac{1}{k^2\lambda_{Dj}^2}\left\{\frac{1 + \zeta_{j0}\sum\limits_{n=-\infty}^{\infty}\Gamma_n(b_j)Z(\zeta_{jn})}{1 + \frac{i\nu_j}{k_\parallel v_{tj}}\sum\limits_{n=-\infty}^{\infty}\Gamma_n(b_j)Z(\zeta_{jn})}\right\} \tag{4.3}$$

where $b_j = k_\perp^2\rho_j^2$, k is the wavenumber, $k_\perp$ ($k_\parallel$) is the component of k perpendicular (parallel) to the magnetic field B, ρ_j is the gyro-radius, $\zeta_{jn} = (\omega + i\nu_j - n\Omega_n)/k_\parallel v_{tj}$, Ω_n is the gyro-frequency, v_{tj} is the thermal velocity, ν_j is the collision frequency, $\Gamma_n(b_j) = I_n(b_j)\exp(-b_j)$, Z is the Fried Conte function, I_n is the modified Bessel function of the first kind of order n, λ_{Dj} is the Debye length and β_e the coupling coefficient, proportional to the pump field E_0, is given by

$$\beta_e = \frac{e}{m_e}\left\{\left(\frac{E_{0\parallel}k_\parallel}{\omega_0^2} + \frac{E_{0x}k_x + E_{0y}k_y}{\omega_0^2 - \Omega_{ce}^2}\right)^2 + \frac{(E_{0x}k_y - E_{0y}k_x)^2\Omega_{ce}^2}{\omega_0^2(\omega_0^2 - \Omega_{ce}^2)^2}\right\}^{1/2} \tag{4.4}$$

and $k_\perp^2 = k_x^2 + k_y^2$. The pump wave is modeled using the dipole approximation, i.e., $k_0 = 0$. It should be noted that a more refined approach would be to assume the pump wavenumber is that of the field aligned irregularities generated from the Oscillating Two Stream Instability OTSI [*Huang and Kuo*, 1995]. The simplified theory provided here will be shown to be adequate for initial interpretation of the experimental observations. A more refined framework will be the subject of future investigation.

The Bernstein modes propagate almost perpendicular to the magnetic field, therefore, it is assumed the parametric decay process occurs at the upper hybrid altitude in which, as it was shown before, the electric field is almost perpendicular to the geomagnetic field; also the double resonance condition is assumed for second gyro-harmonic heating i.e. $\omega_0 \approx \omega_{uh} =$

Figure 4.2: Dispersion relation of the low frequency decay mode (solid lines) and corresponding parametric decay instability growth rate (dashed lines) for $\theta_E = 4°$, $\omega_0 = 2\Omega_{ce} - 10\Omega_{ci}$, $\nu_i = 3$ Hz, $\nu_e = 400$ Hz a) $v_{osc}/v_{te} = 0.35$ b) $v_{osc}/v_{te} = 0.4$ c) $v_{osc}/v_{te} = 0.6$ d) $v_{osc}/v_{te} = 0.7$ obtained from equation 4.2. Note that as the pump strength increases more harmonics are destabilized.

$2\Omega_{ce}$. The full dispersion relation is solved numerically for various parameter regimes. In all the calculations oxygen ions are assumed, the electron to ion temperature ratio $T_e/T_i = 3$, the ion-neutral collision frequency $\nu_i = 3$ Hz and the electron-neutral collision frequency $\nu_e = 400$ Hz except where noted. The electric field is assumed to be slightly off-perpendicular to the background magnetic field and the off-perpendicular angle is denoted by θ_E. The pump field strength is described by the electron oscillating velocity $v_{osc} = eE_0/m_e\omega_0$ where e is the electron charge. With no pump field, $v_{osc} = 0$, the solution of 4.2 will yield the normal modes. It is instructive to note the frequency shift of the spectral features from the pump frequency is essentially determined by the low frequency decay modes. To reiterate, there are two primary low frequency decay modes in this case. The first is the neutralized ion Bernstein mode otherwise known as the electrostatic ion cyclotron harmonic wave e.g. [*Kindel and Kennel*, 1971]. These have the dispersion relation

$$\omega \approx n\Omega_{ci}[1 + \frac{T_e}{T_i}\Gamma_n(k_\perp^2\rho_i^2)] \tag{4.5}$$

for the nth harmonic. The perpendicular wavelength is determined roughly from $k_\perp\rho_{ci} \sim n$ and the parallel wavelength from $k_\parallel/k_\perp \sim 0.1$. It is noted that the frequency shift above the gyro-harmonic is determined by the ratio of T_e/T_i. The oblique IA wave is the other low frequency decay mode and has the dispersion relation approximated by

$$\omega \approx k_\perp c_s \tag{4.6}$$

where $c_s = \sqrt{KT_e/m_i}$ is the sound speed and K is Boltzmann constant. Figure 4.2 demonstrates the influence of the electron oscillating velocity on the ion gyro-harmonic structures for $\theta_E = 4°$ and $\omega_0 = 2\Omega_{ce} - 10\Omega_{ci}$. It shows the dispersion relation of the low frequency decay mode (shift of the destabilized wave from the pump frequency) and the corresponding growth rate (i.e. $\omega_s = \omega + j\gamma$). Of course in this case, the dispersion relation is that of the neutralized ion Bernstein modes otherwise known as electrostatic ion cyclotron harmonic waves as stated earlier. The left vertical axis is normalized frequency (solid curves); the right is normalized growth rate (dashed curves) and the horizontal axis is the perpendicular normalized wave number. As the electric field strength increases, the number of destabilized modes also increases, the most excited mode changes from the second mode to the fourth mode. For this parameter regime, the second mode has the lowest threshold level. A more comprehensive study of the threshold level for $\nu_i = 1$ Hz, $\nu_e = 400$ Hz, $\omega_0 = 2\pi(2.8 \times 10^6)$ rad/s, $\theta_E = 4°$ and $\omega_0 = 2\Omega_{ce} - 25\Omega_{ci}$ is shown in Figure 4.3. The third mode has the lowest threshold level. According to these calculations, the threshold electric field intensity for generation of fourteen ion gyro-harmonic structures by consideration of the damping rates is as low as 14 V/m. This electric field intensity is approximately by a factor of twenty less than the threshold level that was estimated for generation of ion gyro-harmonic structures in the reflection altitude [*Bernhardt et al.*, 2011]. It is determined that for the higher ion-neutral collision frequencies, e.g. $\nu_i \sim 3$ Hz, the first and second modes are stable. The corresponding growth rate for $v_{osc}/v_{te} = 0.6$ ($|E_0| = 12$ V/m) is displayed versus frequency in Figure 4.4.
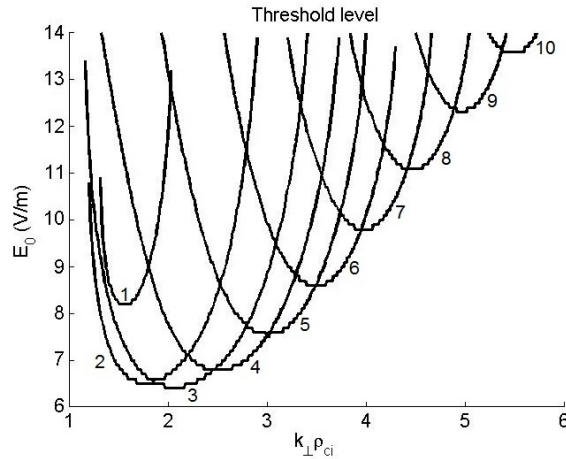
Figure 4.3: Threshold electric field intensity required for generation of each harmonic for $\theta_E = 4°$, $\omega_0 = 2\Omega_{ce} - 25\Omega_{ci}$, $\nu_i = 1Hz$ and $\nu_e = 400$ Hz obtained from equation 4.2.

For these parameters, maximum growth occurs in relatively narrow frequency bands with downshifts approximately at $(n + \frac{1}{2})\Omega_{ci}$ where n represents harmonic number. Although the third and second harmonics have the lowest threshold levels respectively, the fourth and fifth harmonics have higher growth rates if the pump field exceeds threshold. Figure 4.5 considers effect of the pump offset frequency relative to the second electron gyro-harmonic frequency on the destabilized modes, for $v_{osc}/v_{te} = 0.6$ and $\theta_E = 4°$. Below the second electron gyro-harmonic frequency, as the offset frequency of the pump field increases, the most excited mode shifts toward the higher modes. Furthermore, as the frequency offset increases, the lower harmonics (first, second, etc) become stable (unless the ion-neutral collision frequency is somewhat lower). Whereas, above the second electron gyro-harmonic frequency, the most excited mode is either the first or the second mode. The maximum growth rate was obtained when the pump frequency was slightly above the second electron gyro-harmonic frequency $\omega_0 \approx 2\Omega_{ce} + 20\Omega_{ci}$. As the offset frequency relative to $\omega_0 \approx 2\Omega_{ce} + 20\Omega_{ci}$ increases, growth rate amplitude decreases so that at around $\pm 90\Omega_{ci}$ offset, all the decay modes are stable and the parametric decay instability does not occur. It should also be mentioned that for higher θ_E and lower ion-neutral and electron-neutral collision frequencies, at bigger offset frequencies such as $\pm 120\Omega_{ci}$, still a few of the modes can be destabilized. However, the angle of the pump field and collisional effects does not make a big difference in the maximum allowed offset frequency. The effect of θ_E on the low frequency decay mode is demonstrated in Figure 4.6 for $v_{osc}/v_{te} = 0.5$ and $\omega_0 = 2\Omega_{ce} - 20\Omega_{ci}$. As θ_E increases, the number of the destabilized harmonics also increases. Moreover, at higher θ_E, highly oblique IA waves with dispersion relation $\omega \approx k_\perp c_s$ is destabilized instead of discrete neutralized IB modes. The growth rate is almost by a factor of two higher. By comparing experimental observations and results of the growth rate calculations, it can be concluded that the IAPD spectral feature most likely involves this decay mode. The simultaneous occurrence of the IAPD
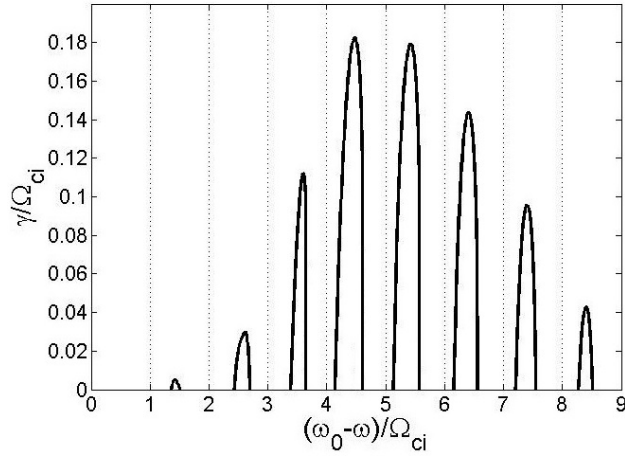
Figure 4.4: Growth rate versus frequency of the destabilized modes for $\theta_E = 4°$, $\omega_0 = 2\Omega_{ce} - 25\Omega_{ci}$, $\nu_i = 1$ Hz, $\nu_e = 400$ Hz and $v_{osc}/v_{te} = 0.6$ ($|E_0| = 12$ V/m) obtained from equation 4.2.

spectral feature and the discrete SIBS structure corresponds to the transition of the low frequency decay mode from the neutralized IB modes to oblique IA mode which exhibits growth in a broad frequency band (Figure 4.6 for $\theta_E = 7°$). Figure 4.7 shows growth rate versus frequency which is to some extent similar to the power spectrums obtained from the experimental measurements (see Figure 2.5 and 2.6). The parameter regime that is used in these calculations are exactly same as Figure 4.6 (c) and (d). The top panel (Figure 4.7 (a)) clearly displays the discrete SIBS structures embedded in the IAPD feature for $\theta_E = 7°$. The bottom panel (Figure 4.7 (b)) shows the IAPD spectral feature obtained for $\theta_E = 8°$. Note, if v_{osc} is reduced, e.g. $v_{osc}/v_{te} = 0.4$, again, instead of the IAPD feature, discrete SIBS spectral characteristic will be excited as in Figure 4.4. This indicates that the threshold electric field intensity that is required to excite SIBS structures is lower than that for the broadband spectral feature effectively. It should be noted that the broadband structures tend to develop when $\gamma/\Omega_{ci} \sim 1$ since the ions are then unmagnetized.

In all the calculations that were presented so far, it was assumed that the angle of propagation of the decay modes, i.e. θ_k, is similar to the angle of the pump electric field ($\theta_k = \theta_E$). However, for a certain angle of the Electric field, still neutralized IB modes can be destabilized in the parameter regime where $k_\parallel/k_\perp \sim 0.1$ [*Kindel and Kennel*, 1971]. Also, the oblique IA mode can propagate at larger off-perpendicular angles. Figure 4.8 shows the growth rate and the dispersion relation of the destabilized mode at two different propagation angles for $v_{osc}/v_{the} = 0.6$, $\theta_E = 13.4°$, $\omega = 2\Omega_{ce} - 5\Omega_{ci}$, $T_e/T_i = 1$. Except for changing the threshold excitation level of the parametric decay instability, collision does not affect the results. Thus, in the current calculations collisions are not included. Five of the neutralized IB modes are destabilized at $\theta_k = 8.4°$. Therefore, for the electric field angles near perpendicular to the
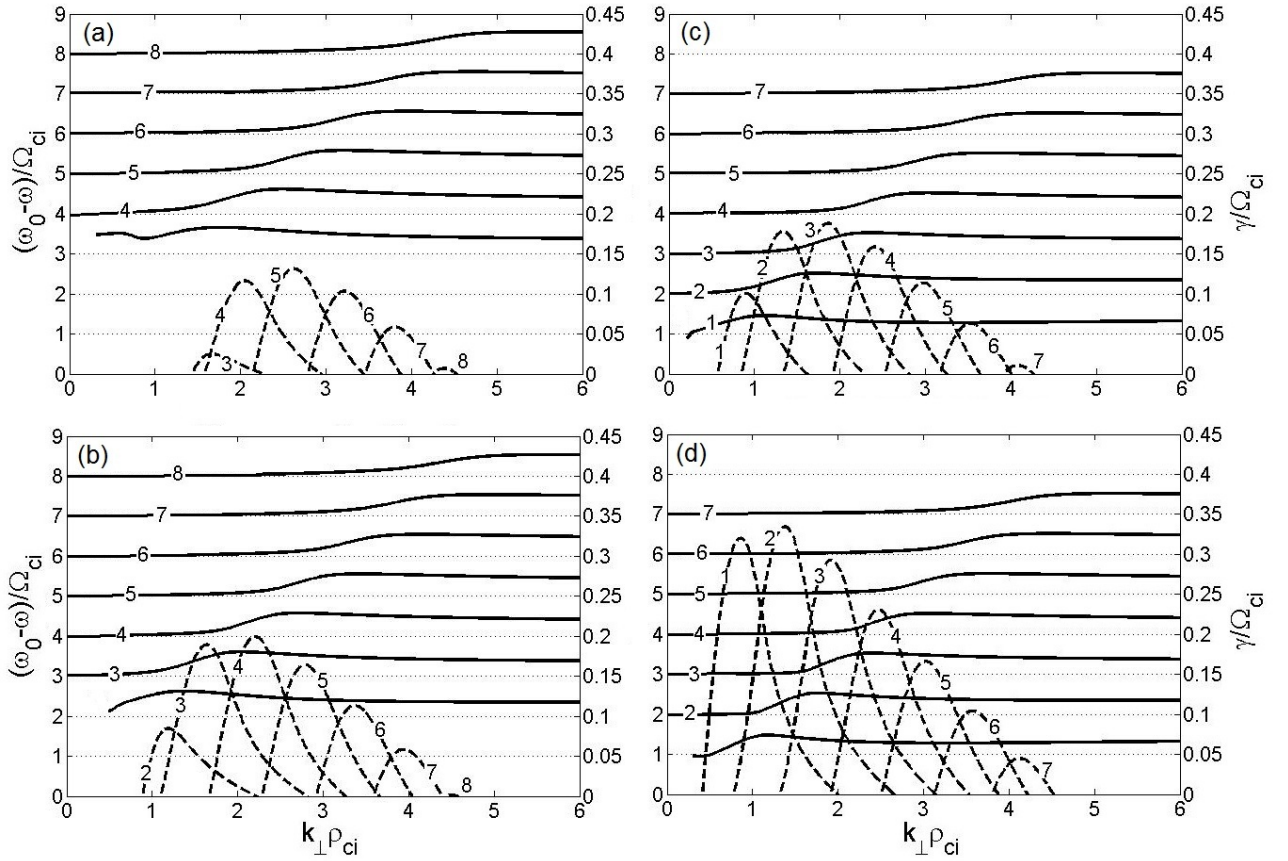
Figure 4.5: Dispersion relation for the low frequency decay mode (solid lines) and corresponding parametric decay instability growth rate (dashed lines) for $\theta_E = 4°$, $v_{osc}/v_{te} = 0.6$, $\nu_i = 3$ Hz, $\nu_e = 400$ Hz, a) $\omega_0 = 2\Omega_{ce} - 30\Omega_{ci}$, b) $\omega_0 = 2\Omega_{ce} - 15\Omega_{ci}$, c) $\omega_0 = 2\Omega_{ce} - \Omega_{ci}$, d) $\omega_0 = 2\Omega_{ce} + 5\Omega_{ci}$ obtained from equation 4.2. Note that increase of the offset frequency below $2\Omega_{ce}$ moves the most excited harmonic to the higher modes.
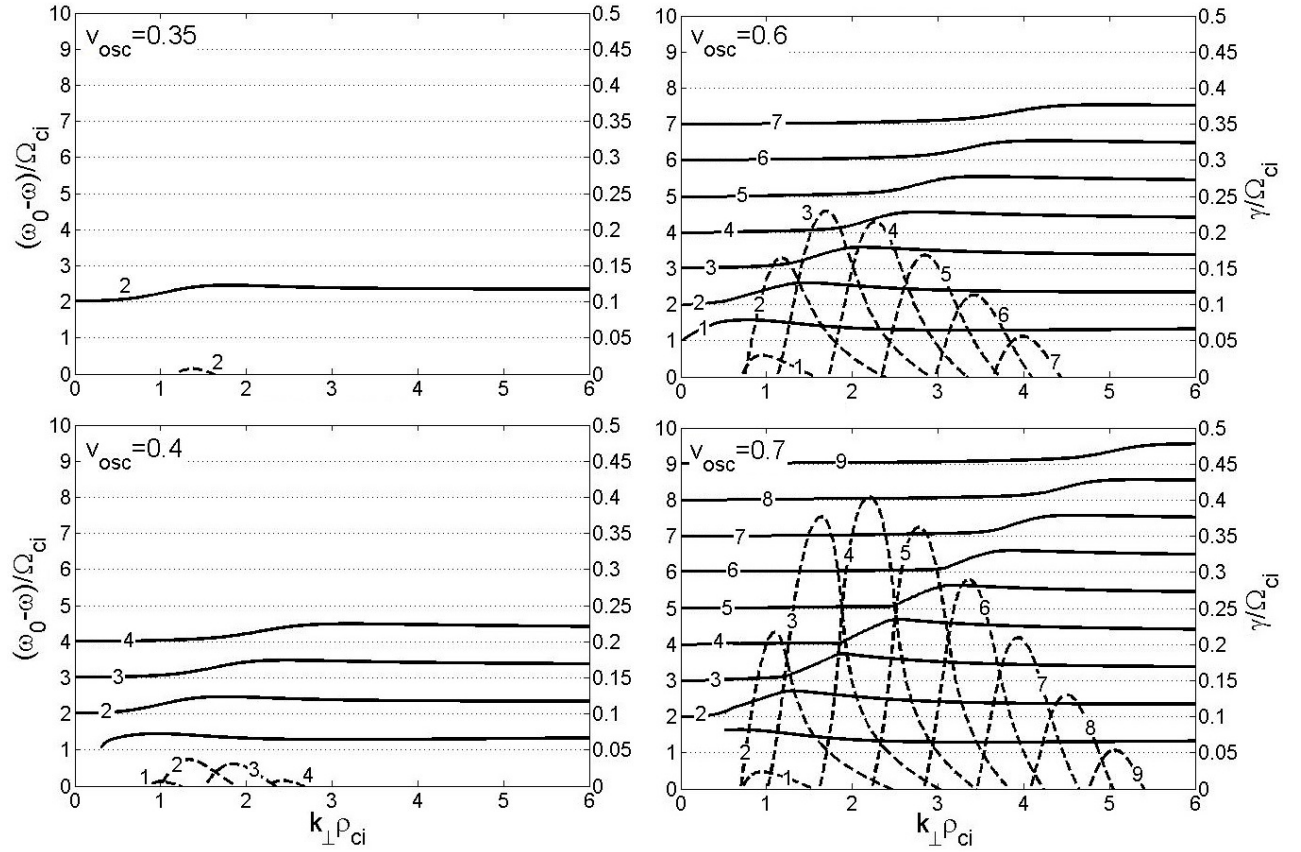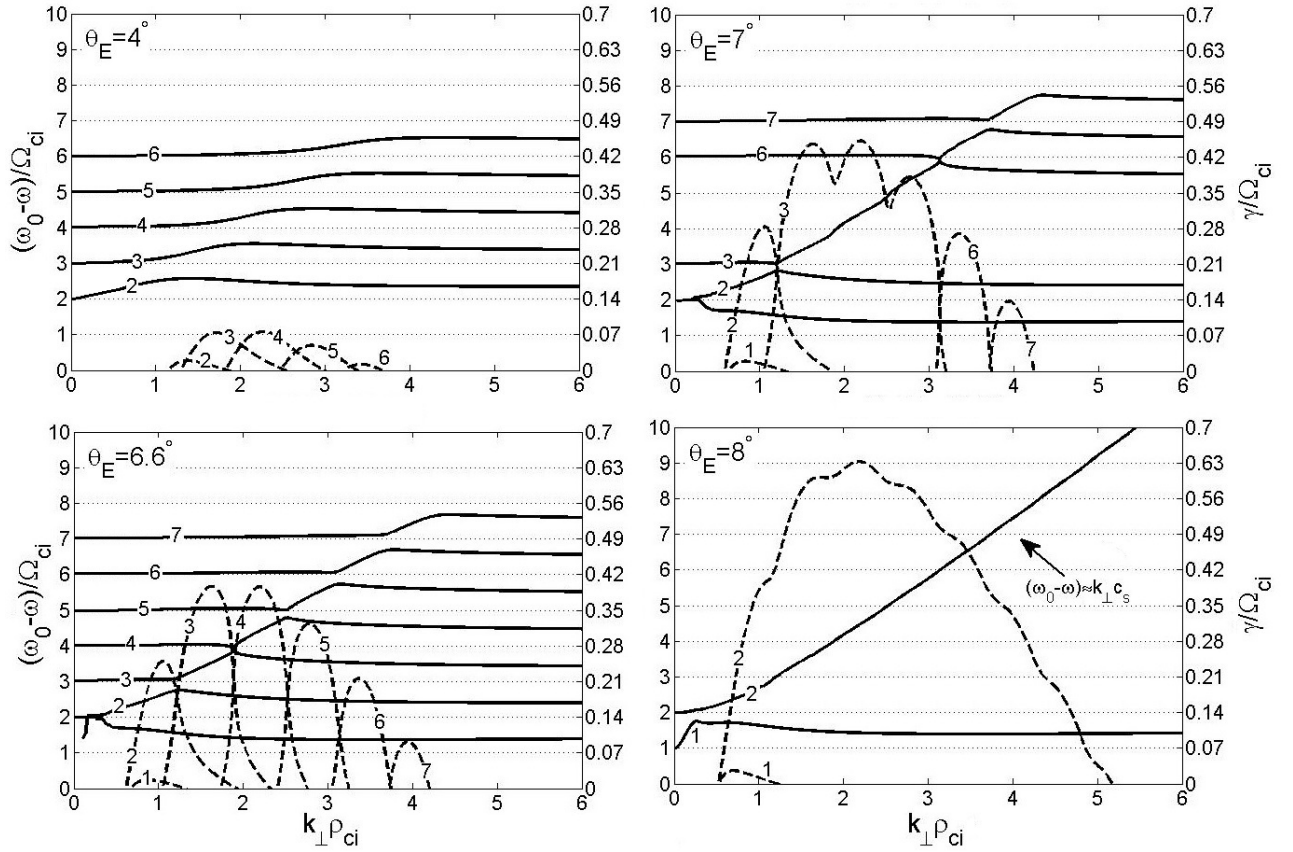
Figure 4.6: Dispersion relation for the low frequency decay mode (solid lines) and corresponding parametric decay instability growth rate (dashed lines) for $\omega_0 = 2\Omega_{ce} - 20\Omega_{ci}$, $\nu_i = 3$ Hz, $\nu_e = 400$ Hz, $v_{osc}/v_{te} = 0.5$, a) $\theta_E = 4°$ b) $\theta_E = 6.6°$ c) $\theta_E = 7°$ d) $\theta_E = 8°$ obtained from equation 4.2 that demonstrates transition of the low frequency decay product from neutralized ion Bernstein to an oblique ion acoustic mode.
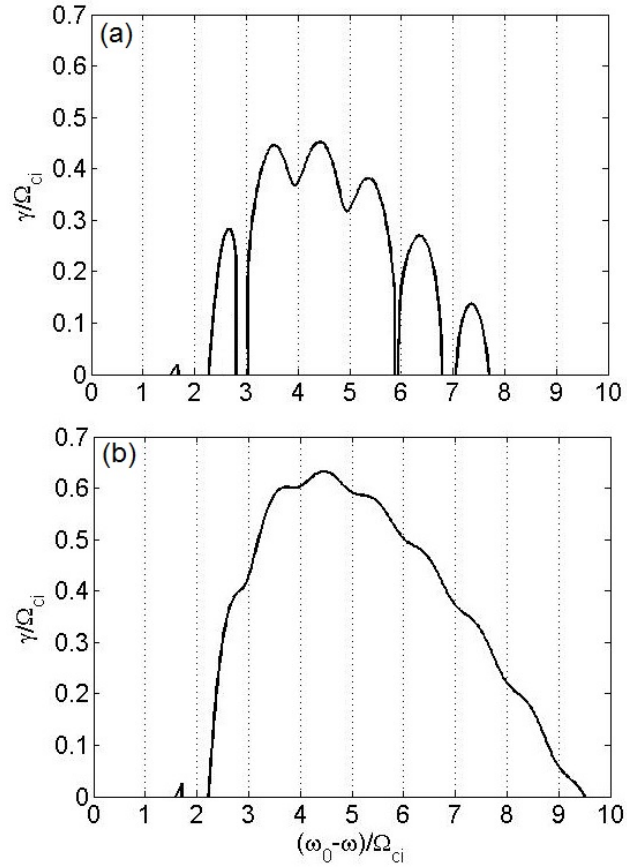
Figure 4.7: Growth rate versus frequency of the destabilized modes for $\omega_0 = 2\Omega_{ce} - 20\Omega_{ci}$, $\nu_i = 3$ Hz, $\nu_e = 400$ Hz, $v_{osc}/v_{te} = 0.5$, a) $\theta_E = 7°$ b) $\theta_E = 8°$ obtained from equation 4.2. Note, as θ_E increases, first, the SIBS structures embed in the IAPD feature and then just the IAPD spectral feature is excited
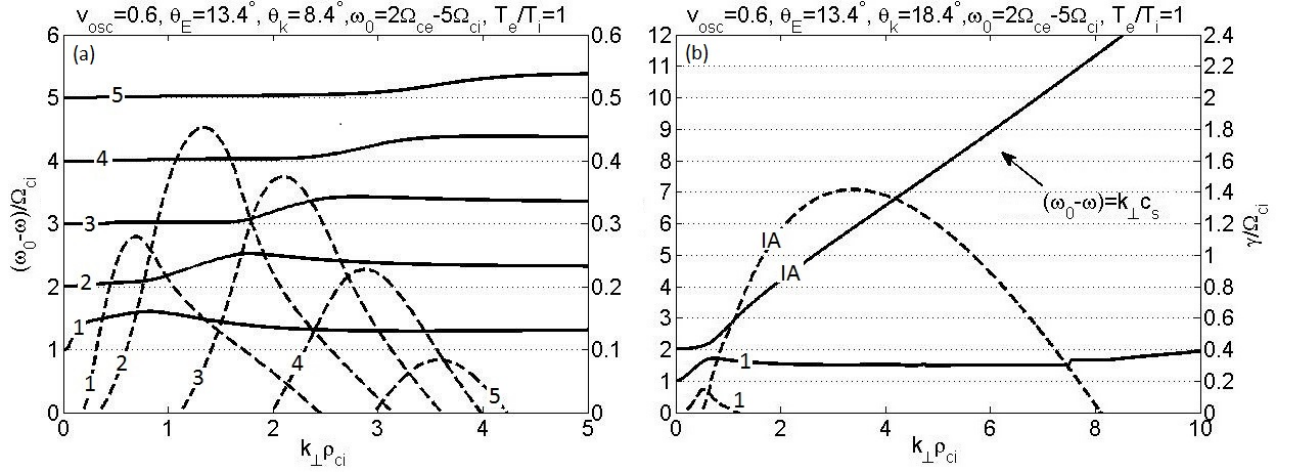
Figure 4.8: Dispersion relation for the low frequency decay mode (solid lines) and corresponding parametric decay instability growth rate (dashed lines) for $\omega_0 = 2\Omega_{ce} - 5\Omega_{ci}$, $v_{osc}/v_{te} = 0.6$, $T_e/T_i = 1$, $\theta_E = 13.4°$, a) $\theta_k = 8.4°$ b) $\theta_k = 18.4°$ obtained from equation 4.2. The neutralized ion Bernstein waves are destabilized near perpendicular to the magnetic field and the oblique IA mode propagates at larger off-perpendicular angles in comparison to the angle of the electric field ($\theta_k > \theta_E$).

magnetic field, (i.e. $\theta_E < 7°$) the neutralized IB modes are mostly destabilized in the same direction ($\theta_k \approx \theta_E$). The oblique IA mode has a large growth rate at $\theta_k = 18.4°$. It is critical to determine at which angle the oblique IA has the fastest growth rate. Figure 4.9 demonstrates maximum growth rate of the oblique IA mode at different propagation angles for $v_{osc}/v_{the} = 0.6$, $\theta_E = 13.4°$, and $\omega = 2\Omega_{ce} - 5\Omega_{ci}$. The growth rate of the oblique IA decay mode maximizes at $\theta_k = 18.4°$ for $T_e/T_i = 1$. However, for higher electron temperatures, i.e. $T_e/T_i > 1$ the oblique IA wave is mostly destabilized at larger off-perpendicular angles ($\theta_k = 25.4°$ for $T_e/T_i = 2$). Enhancement of the electron temperature reduces ion Landau damping. During ionospheric heating, the electron temperature enhances. Thus, according to the results of the analytical model the oblique IA decay mode may propagate at large off-perpendicular angles relative to the geomagnetic field.

4.0.1 Summary

In this chapter, the generation mechanism of the SIBS and IAPD SEE spectral features were considered in terms of the parametric decay of the pump field into an upper hybrid/electron Bernstein (UH/EB) wave and neutralized ion Bernstein (IB) waves and/or an oblique ion acoustic (IA) wave. It was shown that a stronger pump electric field destabilizes larger number of the neutralized IB modes and ultimately an oblique IA wave. The first or the second neutralized IB modes has the fastest growth rate when the pump field frequency
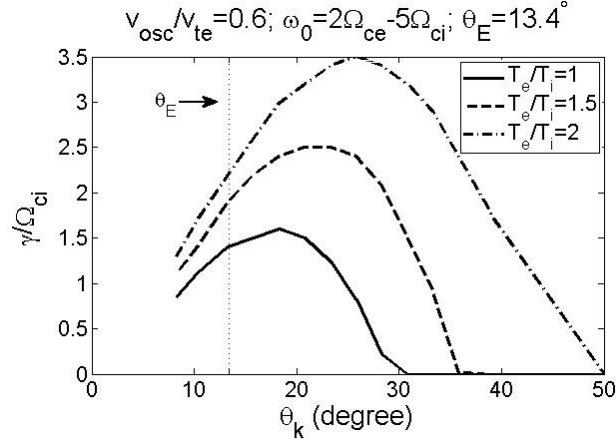
Figure 4.9: Maximum growth rate of the oblique IA decay mode versus their propagation angle for $\omega_0 = 2\Omega_{ce} - 5\Omega_{ci}$, $v_{osc}/v_{te} = 0.6$, $\theta_E = 13.4°$ obtained from equation 4.2. The growth rate is calculated for $T_e/T_i = 1$, $T_e/T_i = 1.5$ and $T_e/T_i = 2$. Note that the oblique IA mode is mostly destabilized at the propagation angles larger than the angle of the electron field ($\theta_k > \theta_E$). As electron temperature increases, the oblique IA mode propagates at larger off-perpendicular angles relative to the geomagnetic field.

is above $2\Omega_{ce}$. On the other hand, below $2\Omega_{ce}$ as the offset frequency of the pump field increases, the higher neutralized IB modes (e.g. 4th, 5th or even the higher ones) have the fastest growth rate. As the frequency offset of the pump field increases, the growth rate reduces and ultimately the parametric decay instability does not develop for offset frequencies larger than $\pm 120\Omega_{ci}$. In general, the maximum growth rate of the neutralized IB modes occur slightly (approximately $5\Omega_{ci}$) above $2\Omega_{ce}$. The minimum electric field intensity required to excite the IB parametric decay instability is as low as 5.5 V/m. The threshold excitation level of the IA parametric decay instability is higher than the IB parametric decay. However, the IA decay instability has the larger growth rate. As the electric field becomes more off-perpendicular to the geomagnetic field, the IA parametric decay is excited instead of the IB decay instability. It was also shown that for a certain angle of the electric field, the IB decay instability can still develop under the parameter regime where $k_\parallel / k_\perp \sim 0.1$. The oblique IA decay wave may propagate at large off-perpendicular angles relative to the geomagnetic field.

Chapter 5

Computational Model

In Chapter 4, the theory of the generation mechanism of the SIBS and IAPD structures in the SEE spectrum was discussed. However, this model does not provide any information about important aspects of nonlinear evolution including wave-particle heating and more strongly nonlinear wave-wave processes. Such important aspects may be linked to experimental observations of the artificial airglow or artificial ionospheric layers. Particle-in-Cell (PIC) plasma computational models e.g. [*Birdsall and Langdon*, 1991] are tools that can begin to at least qualitatively answer some of these unanswered questions and shed light on the nonlinear aspects of the generation mechanism of the aforementioned SEE features in their source region. Procedure of the PIC computational method is shown in Figure 5.1. First the charged particles are distributed in the simulation box. In the current model only two species, i.e. electrons and ions are considered. Then the simulation cycle starts. In each cycle, the electric field is interpolated to each particle position. Next, a new velocity and position of each particle is calculated using the Lorentz force equation. Then, the velocity and position of each particle is modified according to the type of collision they incur. In the next step, the electric charge at each grid point is calculated by weighting charge of each particle to the neighboring grid points. Finally, the electric potential and the corresponding electric field intensity at each grid point is calculated. The total electric field at each grid point is a superposition of the electric field due to the charged particles and the external pump electric field. This cycle iterates. Clearly in the PIC model the interaction of the pump wave and the charged particles that may trigger the development of new instabilities such as parametric decay instability can be investigated. Note that, in order to make the PIC modeling computationally feasible, a reduced mass is used for ions. As the ion mass increases the ion gyro-frequency becomes smaller, therefore, it takes a huge amount of computational time to resolve one ion gyro-period in the simulation.

A 1.5 dimensional PIC model was used previously to study the generation mechanism of a number of the classic SEE features such as Downshifted Maximum (DM), Upshifted Maximum (UM), Downshifted Peak (DP) [*Scales et al*, 1995; *Hussein et al.*, 1997], and the Broad
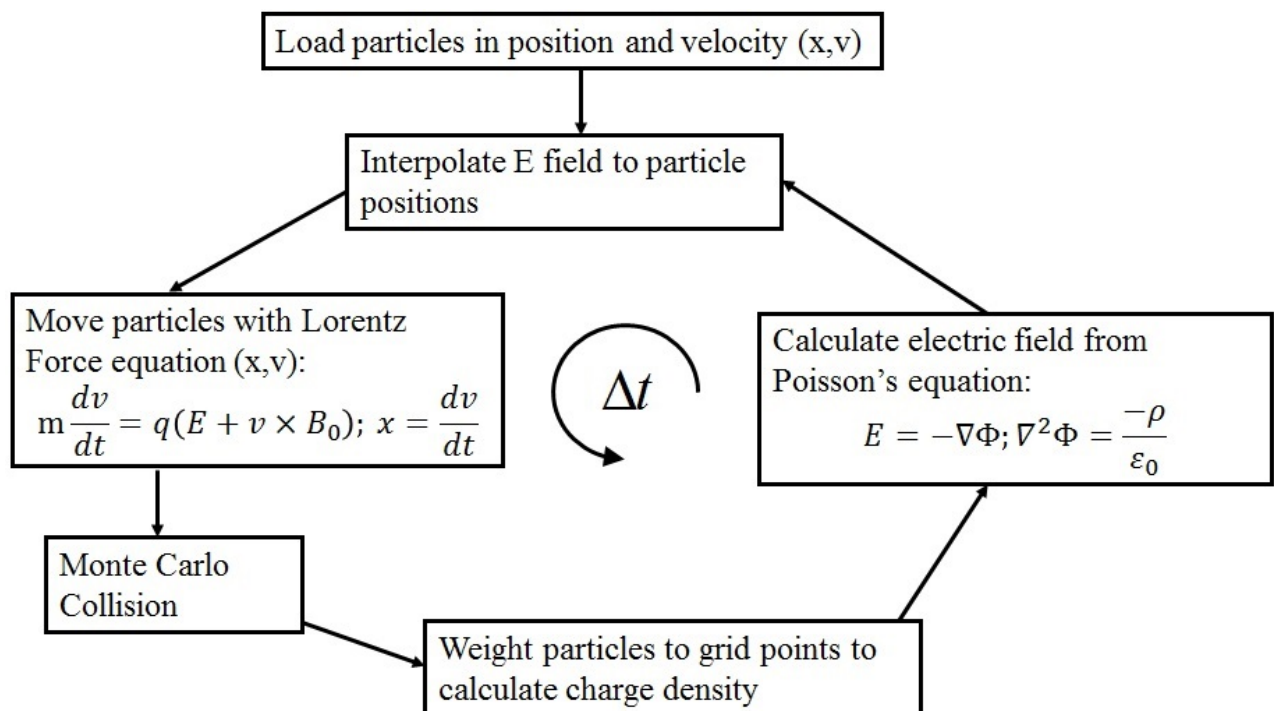
Figure 5.1: Procedures of the electrostatic particle-in-cell Monte Carlo (PIC-MCC) computational model [*Courtesy of Dr. Wayne A. Scales*].
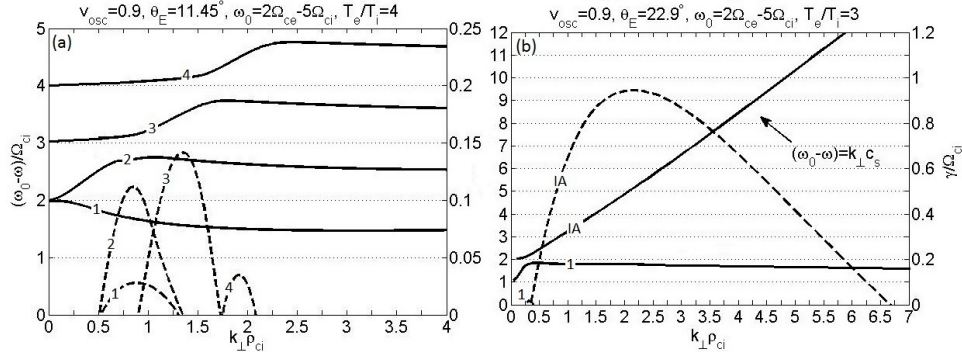
Figure 5.2: The dispersion relation (i.e. frequency versus wavenumber) and the corresponding growth rate of the low frequency decay mode obtained from equation 4.2 for $\omega_0 = 2\Omega_{ce} - 5.0\Omega_{ci}$, $v_{osc}/v_{te} = 0.9$, $m_i/m_e = 400$ a) $\theta_E = 11.4°$, $T_e/T_i = 4$; b) $\theta_E = 22.9°$, $T_e/T_i = 3$. Note for larger θ_E, ion acoustic decay instability is preferentially excited over ion Bernstein decay instability (which produces SIBS).

Upshifted Maximum (BUM) [*Hussein et al.*, 1998; *Scales and Xi*, 2001; *Xi et al*, 2001]. A 2.5 dimensional PIC model was used to study heating experiments near $2f_{ce}$ and look at the generation process of the above mentioned spectral features of the SEE [*Samimi et al*, 2012a]. Preliminary results of the simulation showed significant wave-particle heating along the magnetic field [*Samimi et al*, 2012a]. This work will provide a more comprehensive study of the nonlinear evolution.

In the simulation model that will be described in the next section because of the restrictions of the computational time, an artificial ion-electron mass ratio $m_i/m_e = 400$ is used instead of the real ion-electron mass ratio, i.e. $m_i/m_e = 16 \times 1836$. This small ion-electron mass ratio provides acceptable separation of the electron and ion timescales and will not qualitatively alter the physics. Calculations of the decay instability from equation 4.2 with the scaled simulation parameters are provided here. These calculations are employed as a guidance for the simulations and provide a framework for comparing and justifying the simulation results. The calculations of the decay instability using reduced mass ratio show qualitatively similar behavior to what is obtained using the real ion-electron mass ratio. Figure 5.2 is one example of the calculations that shows the effect of the angle of the electric field relative to the geomagnetic field on the low frequency decay mode for $v_{osc}/v_{te} = 0.9$, $\omega_0 = 2\Omega_{ce} - 5\Omega_{ci}$, a) $T_e/T_i = 4$ and $\theta_E = 11.4°$, b) $T_e/T_i = 3$ and $\theta_E = 22.9°$. These parameters are in the same regime that was used for the calculations of the decay instability in Chapter 4 for the real ion-electron mass ratio. The left vertical axis shows the normalized frequency, the right vertical angle shows the corresponding normalized growth rate and the bottom axis shows the normalized perpendicular wavenumber. The solid lines are the dispersion relation and the dashed lines are the corresponding growth rate. These calculations show that as the pump electric field becomes more off-perpendicular to the background magnetic field the oblique

IA wave responsible for the IAPD structures is excited instead of the neutralized IB waves. It should be noted that the calculations in Figure 5.2 are made with the propagation angle $\theta_k = \theta_E$. Typically, for the IB parametric decay instability, the maximum growth occurs for $\theta_k \approx \theta_E$. However, it should be noted that as was shown in Chapter 4, the IA parametric decay usually has large growth out to very oblique angles relative to the background magnetic field, i.e. $\theta_k \approx 40°$. Increase in the ratio T_e/T_i also allows the propagation to larger off perpendicular angles due to reduction in ion Landau damping. This effect becomes particularly important during electron wave-particle heating as will be seen in the simulations discussed in Section 5.2. The elevation in electron-ion temperature ratio T_e/T_i due to wave-particle heating also has some bearing on the number of SIBS lines observed which is in line with equation 4.2 which will be discussed.

In the experiments described in Chapter 2, frequency sweeping was not available. The preponderance of the observations are such that $f_0 \leq 2f_{ce}$ which implies the emphasis of the simulation investigation here. Although frequency sweeping near $2f_{ce}$ issue is considered to some degree here, a more thorough study is planned for the future as some past experimental work [*Kosch et al.*, 2005; 2007] has specifically considered heating above the gyro-harmonic frequencies ($f_0 > 2f_{ce}$).

5.1   Simulation Model

A periodic two space and three velocity dimensional Particle-In-Cell Monte-Carlo Collision (PIC-MCC) computational model using standard techniques [*Birdsall and Langdon*, 1991] is employed in this study to consider the nonlinear aspects of the generation mechanism in the upper hybrid source region. Since the early time nonlinear evolution of the parametric instabilities is considered and it is assumed the pump field amplitude is of sufficient strength to be above threshold, collisions are neglected. The boundary conditions are periodic. The background magnetic field is assumed to be in the z direction and electric field is slightly off-perpendicular relative to the background magnetic field. θ_E determines this off-perpendicular angle that is the angle of the E field relative to the y axis. In fact, it is the complementary angle to the angle of the electric field relative to the magnetic field. Figure 5.3 shows the schematic of the simulation domain for this local model. The simulation box is elongated in the z direction. The length in y is $l_y = 512\Delta_y$ and in z is $l_z = 2048\Delta_z$ where Δ_y and Δ_z are the grid cell sizes in y and z respectively and for all cases to follow $\Delta_y = \Delta_z$. Also, $\Delta_{y,z} = \lambda_D$ or $2\lambda_D$. In the interaction region $\lambda_D \sim 1cm$ and $v_{te} \sim 2 \times 10^5 m/s$. Particles are distributed uniformly in space and 49 particles per species per grid cell are used in the simulation. The total electric charge at each grid point is calculated using a linear weighting technique. The initial velocity distribution of the electrons and ions is Maxwellian. It is assumed that at the beginning of the simulation both species are at the same temperature, i.e., $T_e = T_i$ unless otherwise noted. The ion-electron mass ratio $m_i/m_e = 400$ is large enough to separate timescales of the electrons and ions. Since in the interaction region,
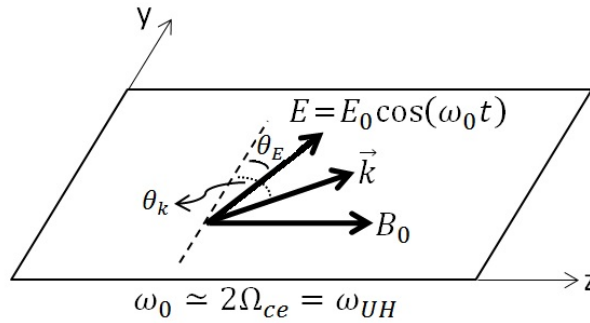
Figure 5.3: Simulation geometry for the local SEE generation model at the upper hybrid layer for second electron gyro-harmonic heating.

the wavelength of the pump field is very large, the dipole approximation ($k_0 \approx 0$) is used to represent the pump electric field, i.e. $\vec{E} = [E_0 \sin(\theta_E)\hat{z} + E_0 \cos(\theta_E)\hat{y}] \cos(\omega_0 t))$. The pump electric field is spatially uniform across the simulation domain. The current collisional model assumes elastic electron-neutral collisions that does not include the dependence of the cross-section on electron energy (e.g. [*Vahedi and Surendra*, 1995]). A more sophisticated collision model, although straightforward to implement, is beyond the scope and intent of the current study, and is planned for future investigation.

5.2 Simulation Results

According to the proposed analytical model of Chapter 4, the IB and IA parametric decay instabilities are responsible for the generation of the SIBS and IAPD in the narrowband SEE spectrum respectively. Several PIC simulations were conducted to study each of these parametric instabilities. In this section, first simulation results of the IB parametric decay instability are discussed. The effect of the pump field strength and the pump field frequency proximity to $2\Omega_{ce}$ on the wave coupling and the particle heating are studied. Next, PIC simulation of the IA parametric decay instability is presented. The possible diagnostic information during the development of this process is discussed. It should be noted that for the simulation runs presented in sections 5.2.1, the electron-neutral collision frequency $\nu_{en} = 0$, although a number of simulations were run including collisional effects within the framework of the model described. The primary impact is to reduce the growth during the exponential growth phase of waves which was observed to be consistent with equation 4.2 as described in Chapter 4. During the nonlinear evolution, this results in a very slight reduction in wave saturation amplitude and particle heating. Therefore no qualitative changes were observed. Due to the emphasis in this investigation, these results have not been described in detail for simplicity.
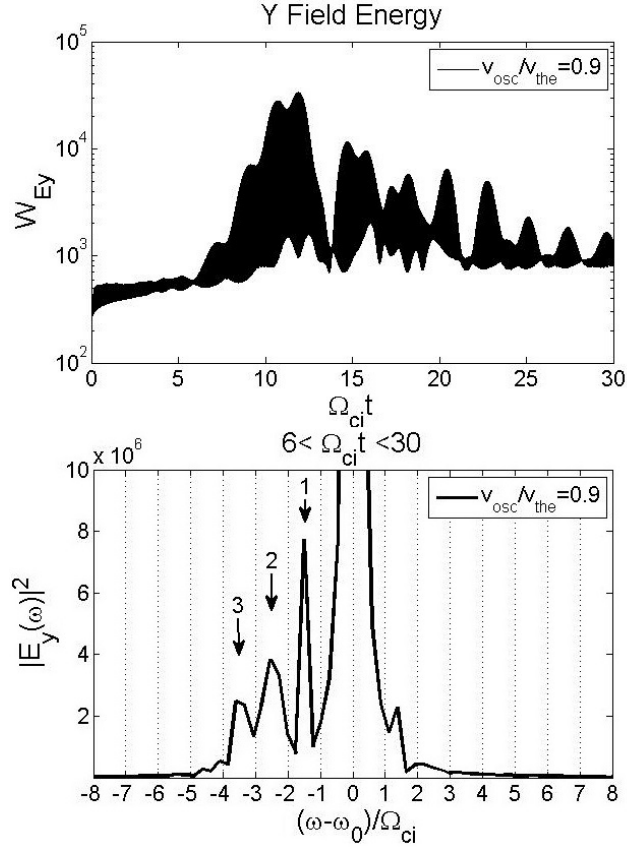
Figure 5.4: Evolution of the IB parametric decay instability electrostatic field energy and the frequency power spectrum of the component of the electric field across the background magnetic field for $\omega_0 = 2\Omega_{ce} - 5.0\Omega_{ci}$, $v_{osc}/v_{te} = 0.9$, and $\theta_E = 11.4°$. The frequency power spectrum shows harmonic spectral features associated with the IB parametric decay instability.
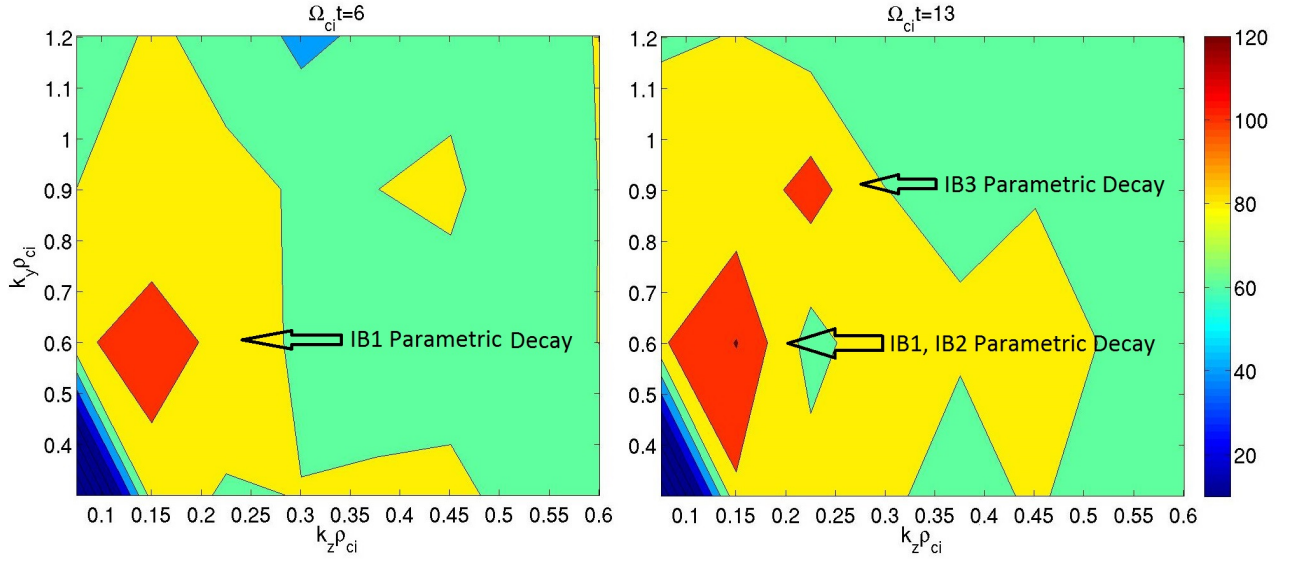
Figure 5.5: Two snapshots of the electric potential wavenumber spectrum for the simulation of Figure 5.4. The left panel corresponds to the time that the parametric decay instability starts to grow. The right panel corresponds to the saturation time. Note that initially the long wavelength mode corresponding to the first ion Bernstein (IB) mode grows and later as the electron temperature increases, the higher IB modes are destabilized.

5.2.1 IB Parametric Decay Instability

For the first simulation case, the pump field parameters are similar to what are used in the analytical calculations of Figure 5.2a, i.e. $v_{osc}/v_{te} \approx 0.9$, $\omega_0 = 2\Omega_{ce} - 5\Omega_{ci}$ and $\theta_E = 11.45°$. Figure 5.4 shows evolution of the electrostatic field energy across the magnetic field i.e. $W_{Ey} = \frac{1}{2}\epsilon_0 \int |E_y|^2 dv$ and the frequency power spectrum of the corresponding electric field component i.e. E_y. The time intervals over which the power spectra are shown are chosen according to the electrostatic (ES) field energy evolution across the magnetic field. The field energy along the magnetic field (not shown) exhibits similar temporal behavior, but is weaker by an order of magnitude. The field energy grows to the saturation state and then starts to slowly decay away. An estimation of the growth rate from the field energy is $\gamma/\Omega_{ci} \approx 0.3$ which is in rough agreement with the analytical model of Section 2 which predicts $\gamma/\Omega_{ci} \approx 0.15$ in Figure 5.2a. Note that in the simulation, the electron temperature increases as the time evolves while in the analytical model, the temperature is constant which most likely accounts for this discrepancy. The frequency power spectrum exhibits three spectral lines ordered by ion gyro-frequency. This result is along the prediction of the analytical model for excitation of the IB waves. Each spectral line is associated with one of the IB modes. Figure 5.5 shows two electric potential wavenumber spectrums ($|\phi(k_x, k_y)|^2$) corresponding to the beginning of the field energy growth ($\Omega_{ci}t = 6$) and its saturation time
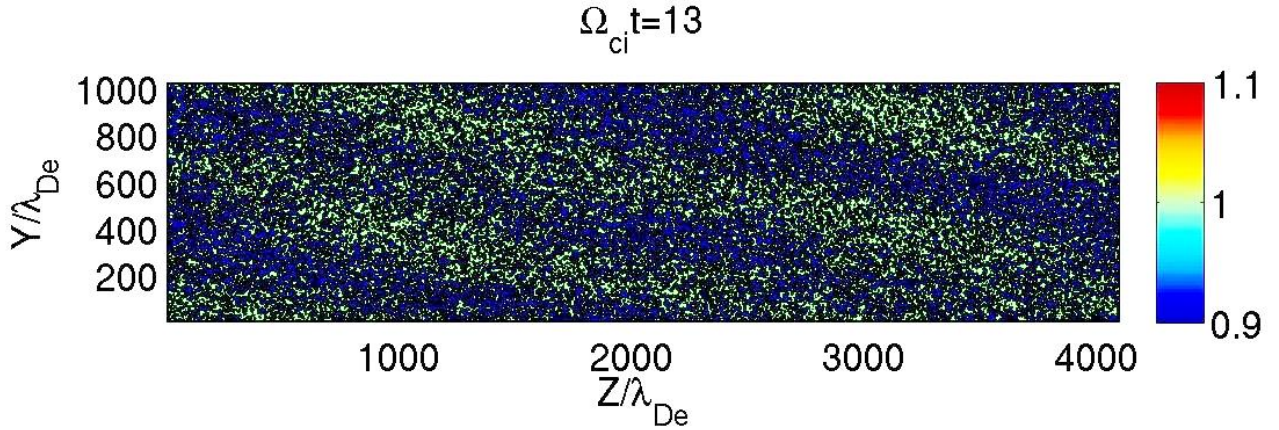
Figure 5.6: Snapshot of the electron density profile at the interaction region at the saturation time for the simulation of Figure 5.4. Note that electron density irregularities due to the IB parametric decay instability propagate approximately along the pump wave vector, i.e. $\theta_k \approx \theta_E$.

($\Omega_{ci}t = 13$) as described in Figure 5.4. Initially the first ($n = 1$) IB mode line develops. As the simulation continues and the electron temperature increases, the wavenumber area over which the instability is developing becomes larger. Slightly shorter wavelength corresponding to the second ($n = 2$) IB mode appears in the wavenumber spectrum. Then the second island that is obvious in the right panel of Figure 5.5 develops. This island represents the third ($n = 3$) IB mode. Modal analysis of these islands confirms the development of the different IB modes at different wavelengths as discussed. The second island connects to the first island at later times. In other words the wavelength of the various IB modes overlap. The wavenumber of the IB modes obtained from the wavenumber spectrum is approximately in the same range that is predicted by the analytical model in Figure 5.2 which is $0.5 < k_\perp \rho_{ci} < 1.5$. Figure 5.6 shows the electron density ($n_e(x, y)$) in the simulation box at the saturation time. The electron density shows four dominant wavefronts in the simulation domain with some additional subtle fine structure corresponding to the higher harmonics. The direction of the propagation of the wavefronts is roughly aligned with the pump electric field vector, i.e. $\theta_k \approx \theta_E$, which is consistent with the equation 4.2. This of course implies the maximum growth of the waves is aligned with the pump field vector. It is also consistent with the location of the IB instability on the wavenumber spectrum. Figure 5.7 shows the field energy evolution across the magnetic field and the frequency power spectrum for $v_{osc}/v_{te} = 0.4$. Rest of the parameters are similar to the previous case, i.e. $\omega_0 = 2\Omega_{ce} - 5\Omega_{ci}$ and $\theta_E = 11.45°$. Comparison of the results of the simulation for $v_{osc}/v_{te} = 0.4$ and $v_{osc}/v_{te} = 0.9$ (Figure 5.4 and Figure 5.7) indicates that the IB parametric decay instability starts to develop for the weaker pump field, i.e. $v_{osc}/v_{te} = 0.4$, later than for $v_{osc}/v_{te} = 0.9$. The growth rate of the field energy $\gamma/\Omega_{ci} \approx 0.17$ for $v_{osc}/v_{te} = 0.4$ is approximately one half of the growth rate for $v_{osc}/v_{te} = 0.9$. Therefore, the growth rate almost linearly scales with the pump field strength.
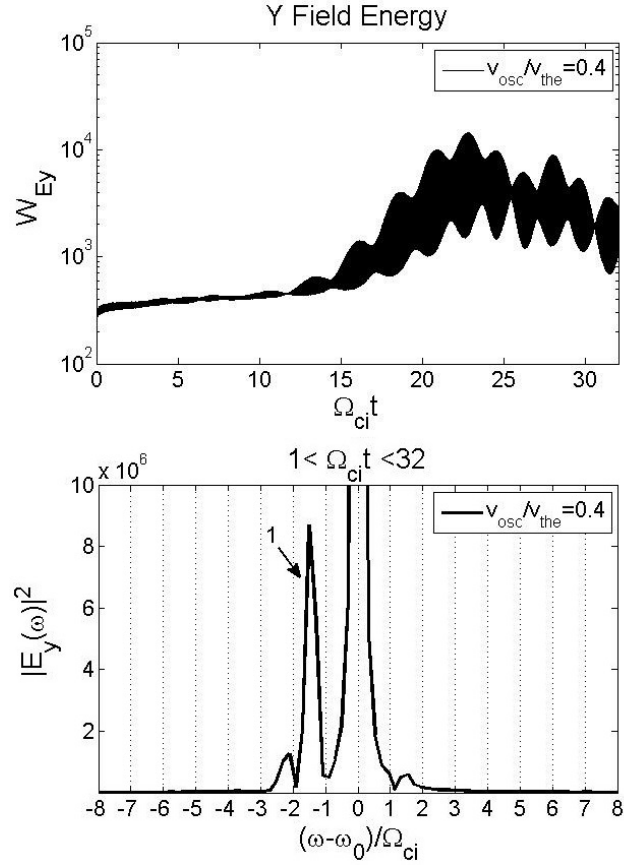
Figure 5.7: Evolution of the IB parametric decay instability electrostatic field energy and the frequency power spectrum of the component of the electric field across the background magnetic field for $\omega_0 = 2\Omega_{ce} - 5.0\Omega_{ci}$, $v_{osc}/v_{te} = 0.4$, and $\theta_E = 11.4°$. The frequency power spectrum shows one spectral line associated with the IB parametric decay instability.

The analytical model of Chapter 4 predicts that for the lower pump field strength, a fewer number of the IB modes are destabilized. The frequency power spectrum for $v_{osc}/v_{te} = 0.4$ (Figure 5.7) only shows one IB mode which is again consistent with the theory.

In the next two simulations, the pump frequency is offset further from the gyro-harmonic frequency ($2\Omega_{ce}$). The analytical model predicts that for heating below $2\Omega_{ce}$, as the offset frequency of the pump field relative to $2\Omega_{ce}$ increases, higher IB modes are destabilized. Recent experimental observation of the SIBS structures is also in agreement with the analytical model [*Mahoudian et al*, 2013]. The higher modes have shorter wavelength. Figure 5.8 shows the field energy across the magnetic field, the electron kinetic energy across the magnetic field and the frequency power spectrum for $v_{osc}/v_{te} = 0.6$ and $\theta_E = 12.8°$. For the simulation shown in the left panels $\omega_0 = 2\Omega_{ce} - 7.5\Omega_{ci}$ and for the one shown in the right panels $\omega_0 = 2\Omega_{ce} - 10\Omega_{ci}$. It is important to note that although the pump field strength is $v_{osc}/v_{te} = 0.6$, the field energy grows larger by an order of magnitude than the previous case for which $v_{osc}/v_{te} = 0.9$. Again this is due to the fact the larger shift in pump frequency from $2\Omega_{ce}$ is more impactful than the reduction in pump amplitude v_{osc}/v_{te} compared to the previous simulation parameters. A rough estimation of the growth rate from the field energy growth is $\gamma/\Omega_{ci} \approx 0.6$ for $\omega_0 = 2\Omega_{ce} - 7.5\Omega_{ci}$ and $\gamma/\Omega_{ci} \approx 1$ for $\omega_0 = 2\Omega_{ce} - 10\Omega_{ci}$. The electron kinetic energy across the field increases at the same time that the field energy is growing and the IB parametric decay instability is developing. Comparison of the evolution of the field energy and the electron kinetic energy indicates that the instability saturates in electron heating across the magnetic field. It should be noted that some parallel electron heating is observed (not shown) with significantly less amplitude than the perpendicular heating and occurs after the waves have saturated in amplitude. At the saturation time of the field energy, the electron kinetic energy across the magnetic field is almost at its maximum. After the time that the field energy saturates, the enhancement of the electron kinetic energy across the field is relatively small. Therefore, it is observed that the perpendicular heating due to the IB parametric decay instability is significantly reduced as the pump frequency approaches $2\Omega_{ce}$. A number of other simulations were performed at other offsets of the pump and this general trend holds. The frequency power spectrum also exhibits fewer of the IB spectral lines for smaller offset frequencies relative to $2\Omega_{ce}$. The results of the simulations shown in Figure 5.8 exhibit up to ten IB spectral lines for $\omega_0 = 2\Omega_{ce} - 10\Omega_{ci}$ in comparison to five IB spectral lines for $\omega_0 = 2\Omega_{ce} - 7.5\Omega_{ci}$. These simulations also show that the excitation of a larger number of harmonics is associated with more heating across the magnetic field.

Figure 5.9 shows the electric potential wavenumber spectrum and the electron density at the saturation time for the simulation of the right panels of Figure 5.8. The wavenumber spectrum shows wave modes with shorter wavelength in comparison to Figure 5.5, i.e. up to $k_\perp \rho_{ci} \approx 10$; $k_\parallel \rho_{ci} \approx 2.3$. The higher IB modes are destabilized at shorter wavelength in comparison to the first or the second mode. Note that all the wave modes appear in the wavenumber spectrum at the same time. It is consistent with the experimental observation and the analytical model of Chapter 4 that predicts simultaneous generation of all of the

Figure 5.8: The field energy across the magnetic field, the electron kinetic energy across the magnetic field and the frequency power spectrum of the component of the electric field across the magnetic field for $\theta_E = 12.8°$ and $v_{osc}/v_{te} = 0.6$. For the simulation shown in the left panels $\omega_0 = 2\Omega_{ce} - 7.5\Omega_{ci}$ and for the ones in the right panels $\omega_0 = 2\Omega_{ce} - 10\Omega_{ci}$. Note that the kinetic energy across the magnetic field grows significantly as the instability is develping and more IB modes are destabilized with a larger shift of the pump frequency below $2\Omega_{ce}$.

Figure 5.9: Snapshots of the electric potential wavenumber spectrum and the electron density at the saturation time for the simulation of left panels of Figure 5.8. Note that electron density irregularities due to the IB parametric decay instability propagate approximately along the pump wave vector, i.e. $\theta_k \approx \theta_E$. Finer structure compared to Figure 5.6 indicates higher harmonic generation.

IB decay modes rather than cascading processes. The electron density also shows long wavelength waves as well as fine structuring at shorter wavelength which is in line with the wavenumber spectrum. The perpendicular wavenumber of the nth harmonic of the IB mode is roughly $k_\perp \rho_{ci} \sim n$ [*Samimi et al.*, 2013]. This is consistent with the frequency power spectrum of the right panel of Figure 5.8 that exhibits ten IB lines and the wavenumber spectrum of Figure 5.9.

5.2.2   IA Parametric Decay Instability

The IA decay instability has the maximum growth rate at propagation angles that are larger than the angle of the pump electric field vector, i.e. $\theta_k \geq \theta_E$. The instability develops at higher electron temperatures more efficiently due to reduction in ion Landau damping. Thus, initial electron to ion temperature ratio $T_e/T_i = 3$ is used in the next set of simulations for enhanced computational efficiency. Also, although not essential, electron-neutral collisions are useful to clarify important aspects of the evolution of the instability and are included here. It is assumed the ratio of electron-neutral to electron-plasma frequency $\nu_{en}/\omega_{pe} = 4 \times 10^{-4}$ throughout this section. Other parameters were chosen similar to the parameters of Figure 5.2b, i.e. $v_{osc}/v_{te} = 0.9$, $\omega_0 = 2\Omega_{ce} - 5\Omega_{ci}$ and $\theta_E = 22.9°$. The corresponding electrostatic field energy along the magnetic field, the electron kinetic energy along the magnetic field and the frequency power spectrum of the electric field along the magnetic field (E_z) are shown in Figure 5.10. The growth rate of the IA parametric decay instability is roughly estimated from the field energy growth is $\gamma/\Omega_{ci} \approx 0.87$. It is close to $\gamma/\Omega_{ci} \approx 0.95$ predicted by the analytical model of Chapter 4 (Figure 5.2b). Note that in the calculations of Figure 5.2b collision is not considered which causes larger growth rate. Comparison of the field energy evolution and the electron kinetic energy indicates that the IA parametric instability saturates in the electron heating along the magnetic field. It should be noted that some perpendicular heating (not shown) small in comparison to the parallel heating also occurs. After the saturation time, the field energy and the electron kinetic energy exhibit two more phases of growth and saturation. This is likely due to the nonlinear caviton collapse [*Weatherall et al.* (1982)] that will be described in more detail shortly. The frequency power spectrum exhibits the IAPD structure approximately $14\Omega_{ci}$ downshifted from the pump frequency. A weak anti-Stokes line above the pump frequency can also be observed. Furthermore, a second structure at approximately $25\Omega_{ci}$ downshifted relative to the pump frequency is recognizable. This has consistencies with the experimental observations reported in Chapter 2.

Figure 5.15 shows the electric potential wavenumber spectrum and the electron density at the saturation time of the IA parametric decay instability. The electron density irregularity wavefronts propagate at $\theta_k \approx 68°$. Therefore these waves propagate significantly off the direction of the pump electric field vector at the upper hybrid layer. Again this is in contrast to the IB decay instability irregularities that would propagate more in alignment with the pump electric field vector. The wavenumber of the IA mode is estimated $k\rho_{ci} \approx 6.7$. The

destabilized IA mode maximizes at $\omega/\Omega_{ci} = 14.2$. The sound speed $c_s/v_{te}(0) \approx 0.061$ is easily estimated from the well-known IA dispersion relation ($\omega = kc_s$). The electron temperature at the same time that the IA decay instability develops $T_e/T_{e0} = 1.52$. The corresponding analytic sound speed $c_s \cong \sqrt{(KT_e + 3KT_i)/m_i} = 0.056v_{te}(0)$ which is in a very good agreement with the phase speed obtained from the frequency and wavenumber spectrum. This calculation validates that the instability observed in the simulation is the IA parametric decay instability as predicted by the theory in Chapter 4. Note that the other strong wave mode at $k_\perp\rho_{ci} \leq 1$ is due to the $n = 1$ IB parametric decay instability. Figure 5.12 shows evolution of the electric potential wavenumber spectrum for the simulation of Figure 5.10. At the beginning of the IA parametric decay ($\Omega_{ci}t = 2$), the high frequency decay mode develops at $k_\parallel\rho_{ci} \sim 5.8$, $k_\perp\rho_{ci} \sim 3.3$. The wavelength of this wavemode reduces as the instability evolves. This high frequency mode intensifies and then weakens while its wavelength reduces. At $\Omega_{ci}t = 10$ this wavemode disappears from the wavenumber spectrum and another wavemode at longer wavelength, i.e. $k\rho_{ci} \approx 4.8$, appears. This wavemode as shown in the bottom panels of Figure 5.12 intensifies while its wavelength reduces. Again the wavemode weakens and ultimately disappears from the wavenumber spectrum at $\Omega_{ci}t = 23$. Another cycle of the wavemode formation, intensification and suppression starts. Each of these cycles correspond to one cycle of the field energy and the electron kinetic energy growth, saturation and decay that is shown in Figure 5.10.

Figure 5.2.2 shows contours of the electric field magnitude $|E|$ on a logarithmic scale right after the electrostatic field energy can be seen to maximize near $\Omega_{ci}t = 15$ in Figure 5.10. Contours are elongated in a direction nearly across the magnetic field due to the highly oblique propagation angle. In a very short period of time (from $\Omega_{ci}t=16$ to $\Omega_{ci}t=17$) the intensity of the electric fields inside the contours increases by approximately twenty percent. The intensified areas of the contours are at the same locations of electron density depletions (not shown). This implies trapping of the electric fields inside the density cavities. At the same time, the electric potential wavenumber spectrum shows intensification of the wavemode shown in Figure 5.12. The electron kinetic energy shown in Figure 5.10 reaches its maximum at approximately this time period which implies transfer of the electrostatic energy trapped in the density cavities to the electron kinetic energy. After the time snapshots of Figure 5.2.2, the electric field magnitude rapidly decays away.

The nonlinear evolution here appears to be characteristic of caviton collapse considered in past works on Langmuir turbulence during heating experiments [e.g. *Weatherall et al.* (1982); *Dubois et al.*, 1990]. Caviton is a soliton like depletion in the electron density [*Dubois et al.*, 1990]. The electrostatic wave is trapped inside the density cavity. The nonlinear ponderomotive force pushes particles out of the cavity and enhances density depletion [*Chen*, 1984]. As the density cavity is deepened, the trapped electrostatic field intensifies. Ultimately the electric field trapped inside the cavity gives its energy to the electrons and accelerates electrons significantly that results in collapse of the caviton [*Dubois et al.*, 1990]. Figure 5.2.2 shows schematic of the described procedure.
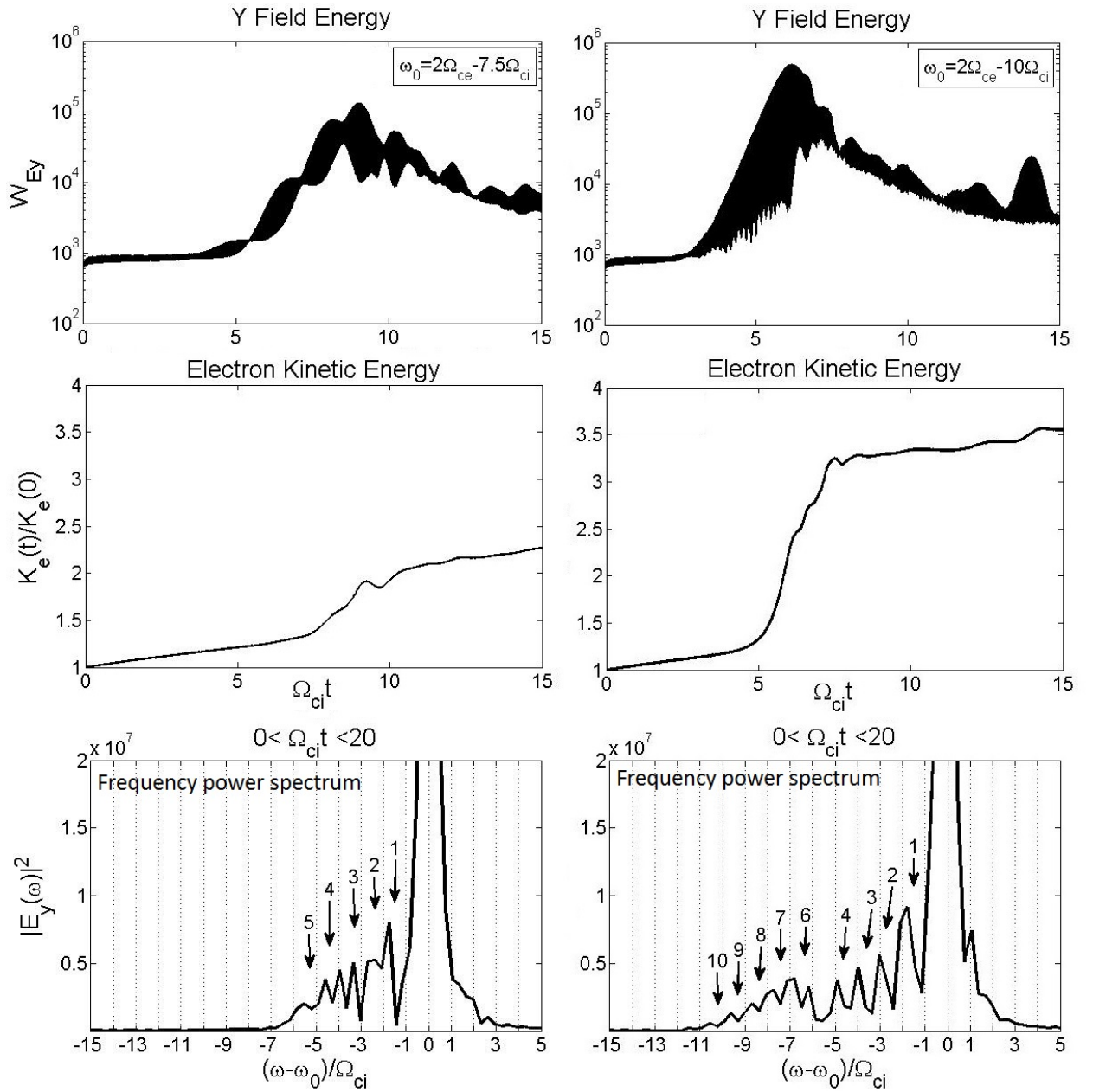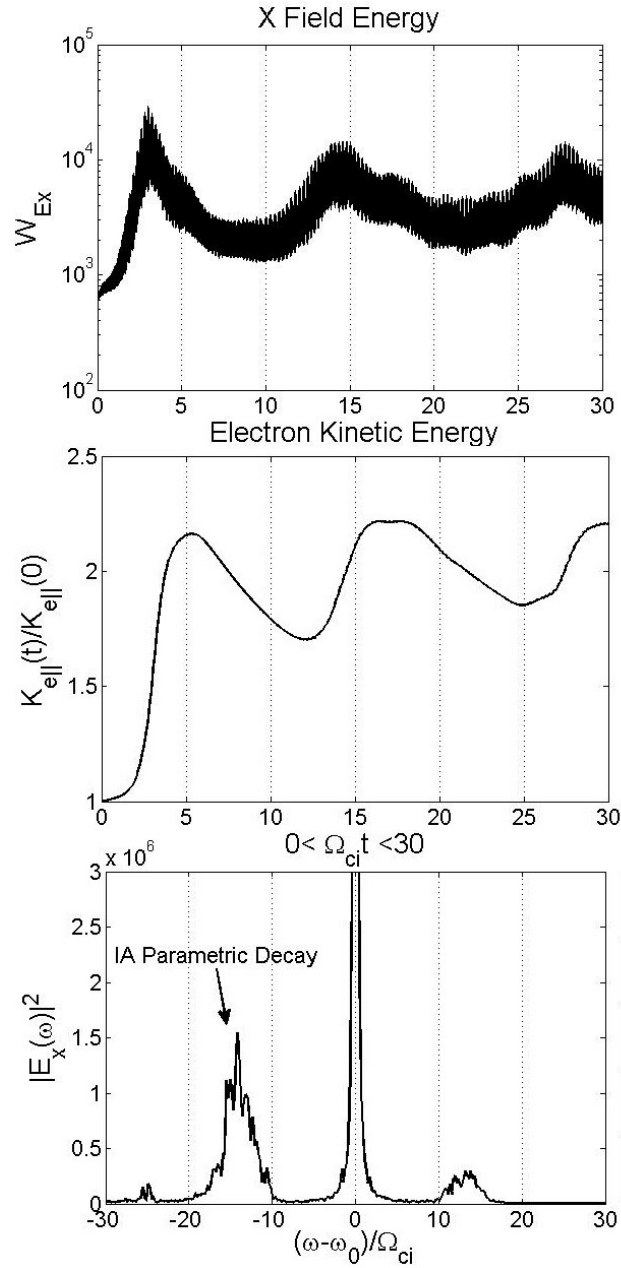
Figure 5.10: The field energy along the magnetic field, the electron kinetic energy along the magnetic field and the frequency power spectrum of the component of the electric field along the background magnetic field for $\omega_0 = 2\Omega_{ce} - 5\Omega_{ci}$, $\theta_E = 22.9°$ and $v_{osc}/v_{te} = 0.9$. The frequency power spectrum exhibits the IAPD feature. Note that the kinetic energy along the magnetic field grows significantly as the instability is developing.
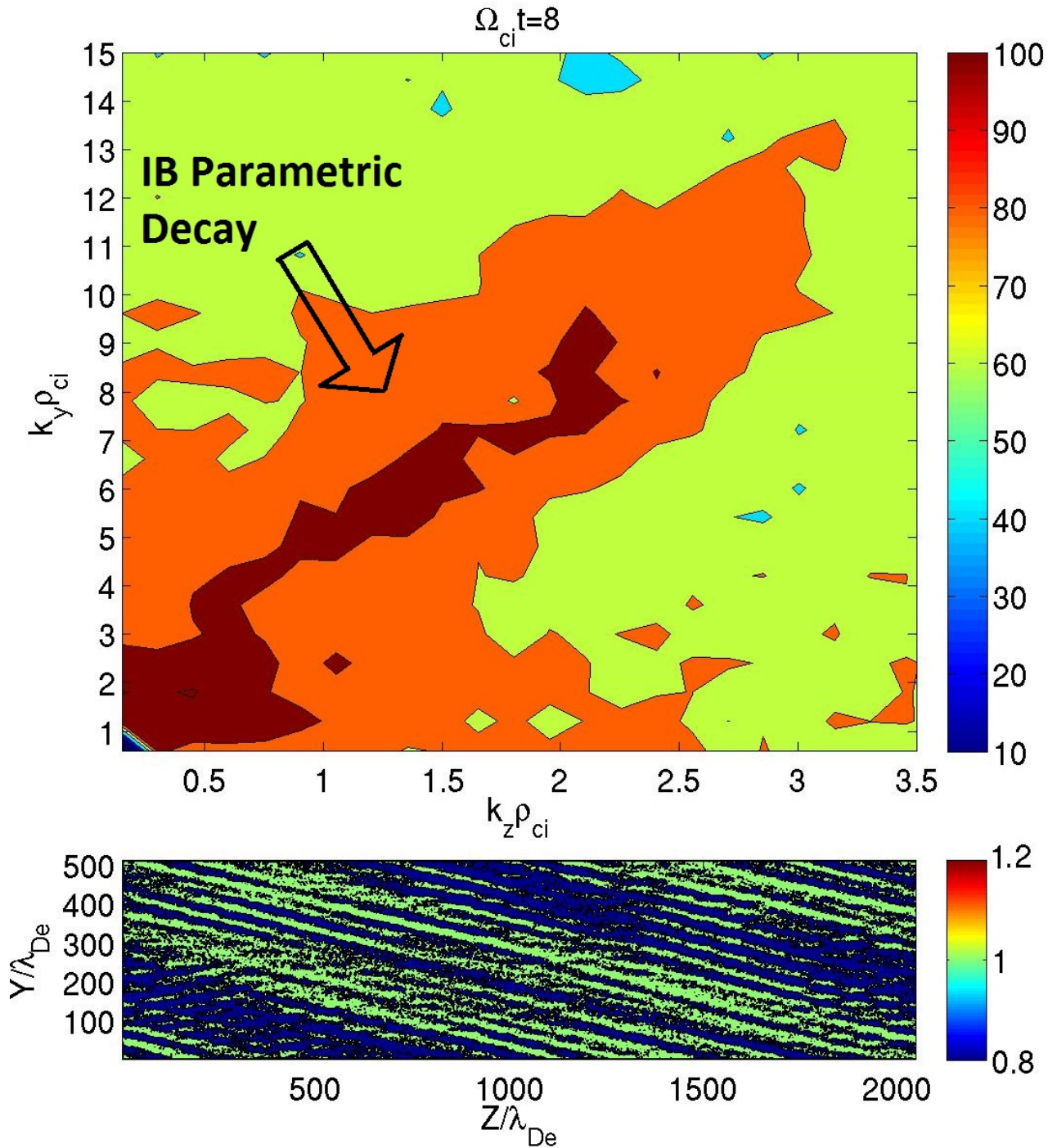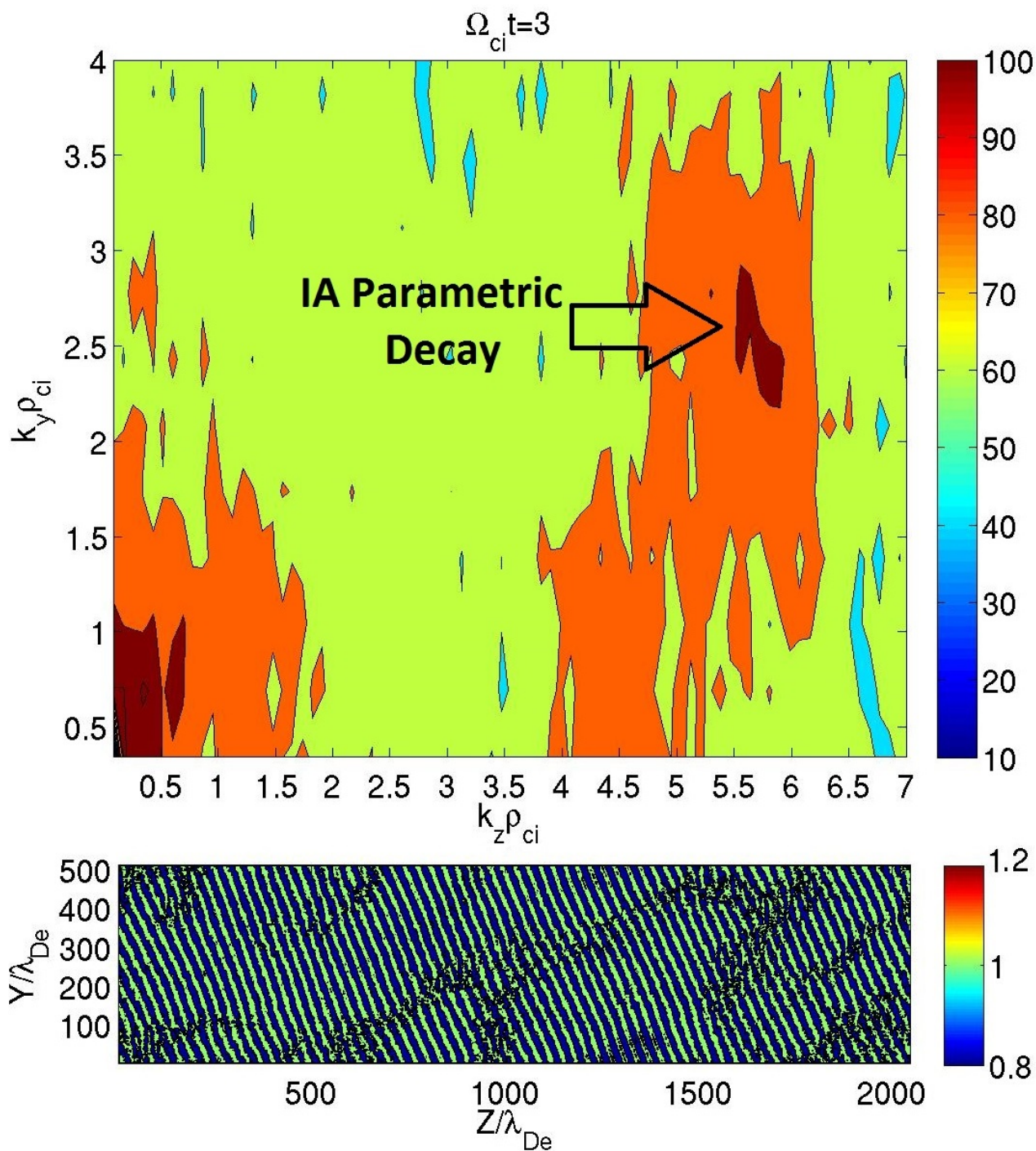
Figure 5.11: Snapshots of the electric potential wavenumber spectrum and the electron density for the simulation of Figure 5.10. Note fine structures indicate electron density irregularities due to the IA parametric decay instability. They propagate at large oblique angle $\theta_k \approx 68°$ relative to the magnetic field $\theta_k >> \theta_E$.
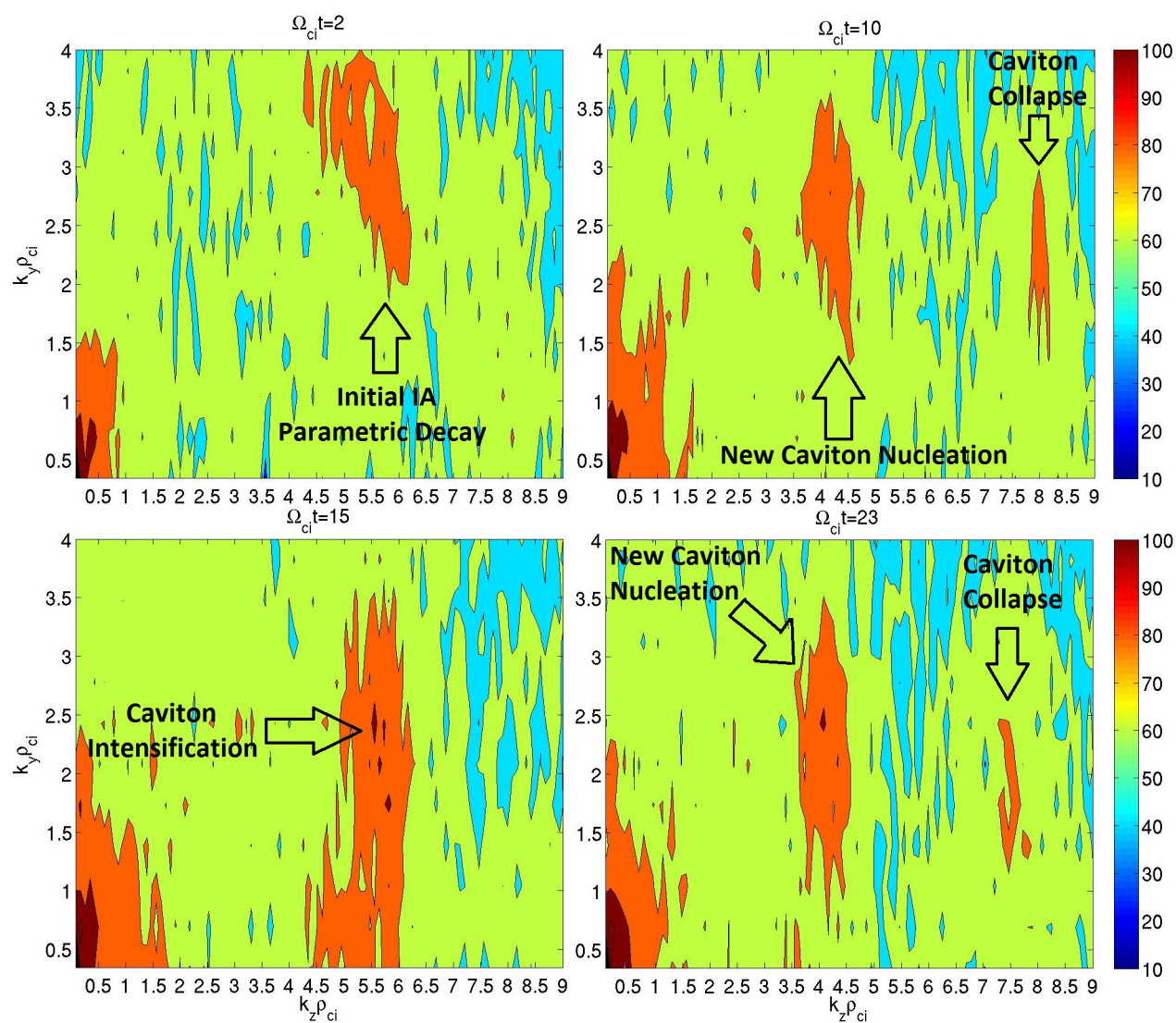
Figure 5.12: Evolution of the electric potential wavenumber spectrum for the simulation of Figure 5.10.
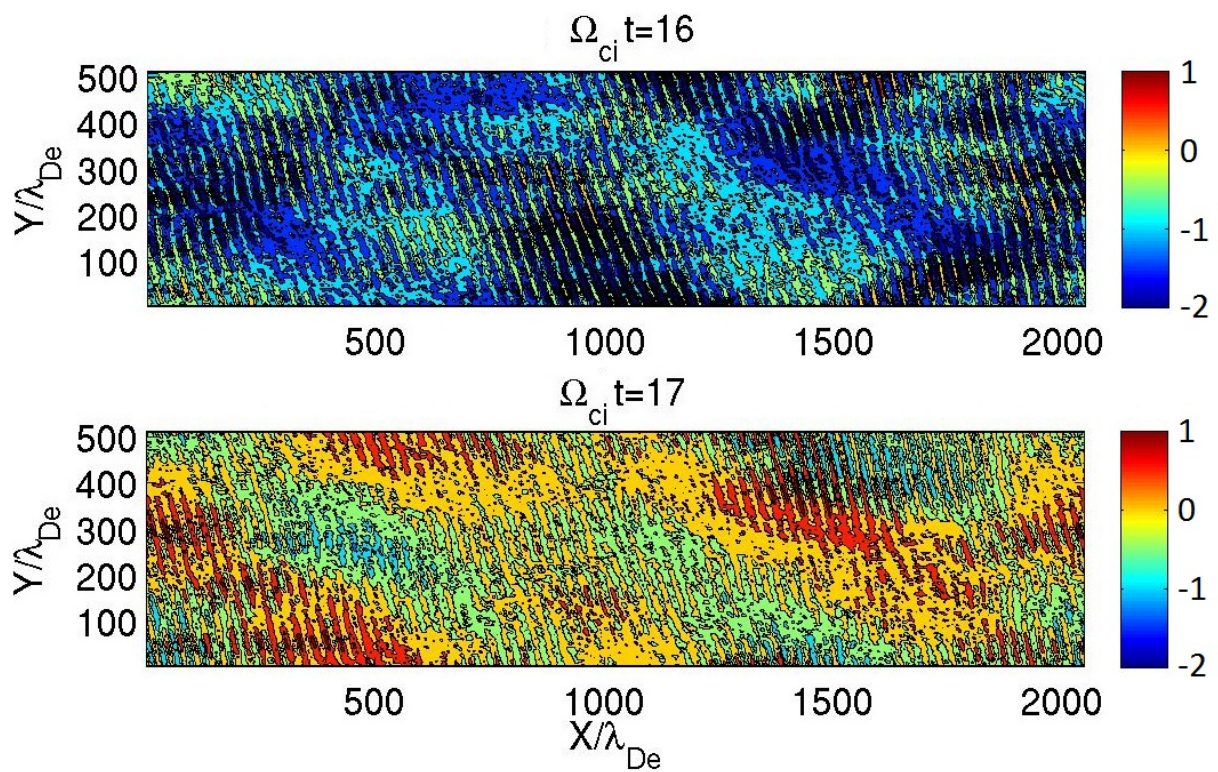
Figure 5.13: Contours of the electric field magnitude prior to a collapse for the simulation of Figure 5.10 showing rapid intensification of the field.
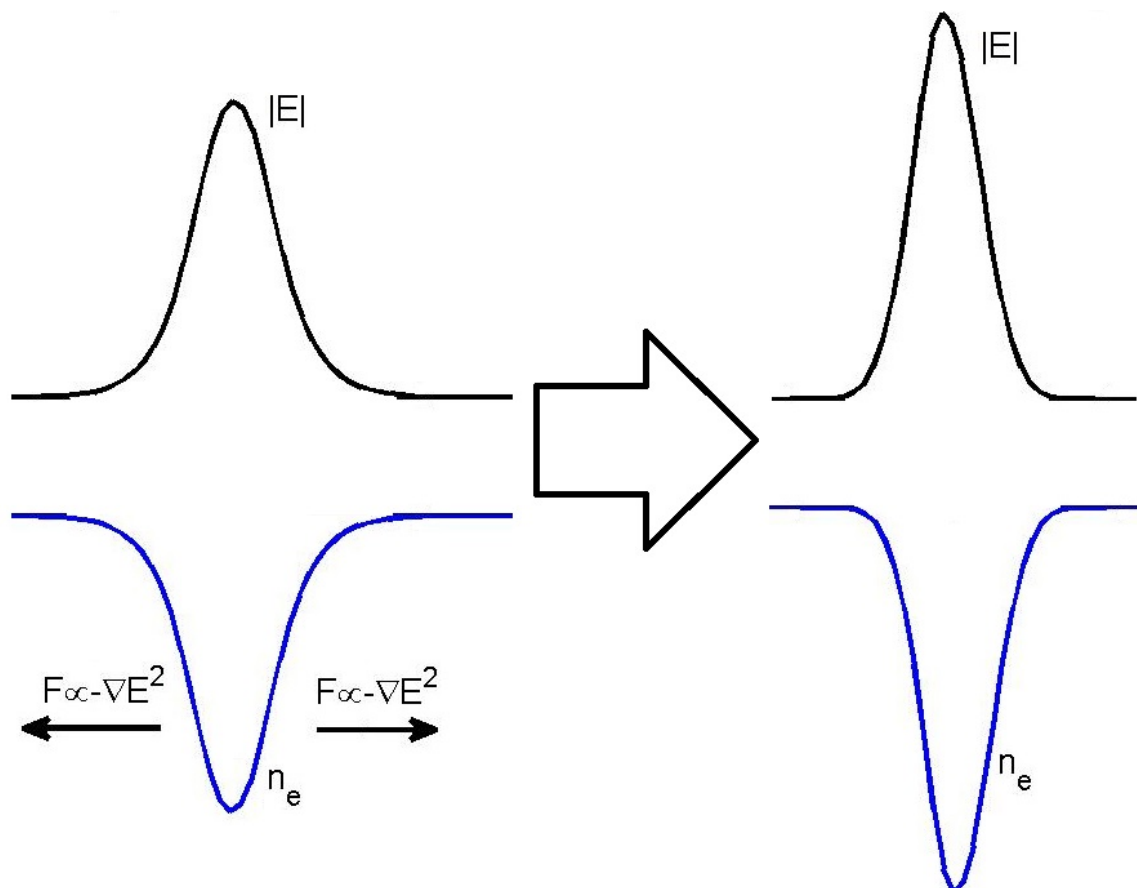
Figure 5.14: Schematic of the caviton and the trapped electric field which results in the nonlinear caviton collapse.

Characteristics observed in the present simulations which support this hypothesis include:
1) After the new cavity is nucleated, its wavelength reduces which implies that the caviton becomes smaller [*Dubois et al.*, 1990]. 2) The corresponding contours of the electric field strength (Figure 5.2.2) indicate that the electric field is intensified inside the caviton [*Weatherall et al.* (1982)]. 3) If the wavenumber of the instability is averaged over a period of time, it is relatively broad [*Dubois et al.*, 1990]. 4) As the wavelength of the new wavemode reduces, the phase speed becomes less than the ion sound speed that can produce caviton collapse [*Nicholson and Goldman*, 1978]. 5) The electrostatic field energy is transferred to the electron kinetic energy along the magnetic field and generates tail heating in the electron velocity distribution function along the magnetic field [*DuBois et al.*, 1993;*Newman et al.*, 1990]. The low frequency power spectrum (not shown) confirms that initially the IA parametric decay instability develops in the simulations just described. The IA parametric instability is expected to possibly play a role in the nucleation of the initial cavitons [*Dubois et al.*, 1990]. Detailed theory of the process just described is out of the scope and intent of the current investigation. However, relevant components will be considered in the future.

Figure 5.15 shows the distribution function of the electron velocity along the magnetic field. It shows strong tail heating in the electron distribution function. The curve of the electron distribution function at $\Omega_{ci}t = 5$ shows enhancement of the number of electrons with $v_z \approx 6v_{te0}$ at the tail of the distribution function. Recent experimental studies show that the IAPD structure is typically observed with the artificially generated ionospheric layers for $2f_{ce}$ heating [*Bernhardt et al.*, 2013]. The significant enhancement of the electron velocity increases the collision frequency that results in more ionization of the neutral particles. Enhancement of the ionization ratio generates the new ionospheric layers. The results here indicate significant acceleration of the electrons along the magnetic field at the upper hybrid layer associated with the IA parametric decay instability which would appear to affirm the possible connection with the generation or triggering mechanism of the artificial ionospheric layers.

Figure 5.16 compares the electron kinetic energy along the magnetic field for $v_{osc}/v_{te} = 0.9$ and $\theta_E = 22.9$ for three pump frequencies: $\omega_0 = 2\Omega_{ce} - 5\Omega_{ci}$, $\omega_0 = 2\Omega_{ce} - 10\Omega_{ci}$ and $\omega_0 = 2\Omega_{ce} - 15\Omega_{ci}$. For all the three cases the IA parametric decay instability develops. For the $\omega_0 = 2\Omega_{ce} - 10\Omega_{ci}$ and $\omega_0 = 2\Omega_{ce} - 15\Omega_{ci}$, the IB parametric decay also develops which increases electron kinetic energy across the magnetic field as well. As the pump frequency approaches $2\Omega_{ce}$ electron heating reduces. This general trend has been reported in experimental observations for heating near higher harmonics of the electron gyro-frequency [*Honary et al.*, 1995].

It should be mentioned that for the offset frequencies $-10\Omega_{ci}$ and $-15\Omega_{ci}$ although the electron temperature enhancement is higher, the nonlinear caviton collapse process is not as strong as for the case with $-5\Omega_{ci}$ offset frequency. The caviton collapse process is dominant in the regimes where the ion Landau damping is high [*Dubois et al.*, 1990]. Enhancement of the electron temperature reduces ion Landau damping. Since heating reduces for the pump frequencies closer to $2\Omega_{ce}$, the caviton collapse process is more dominant.
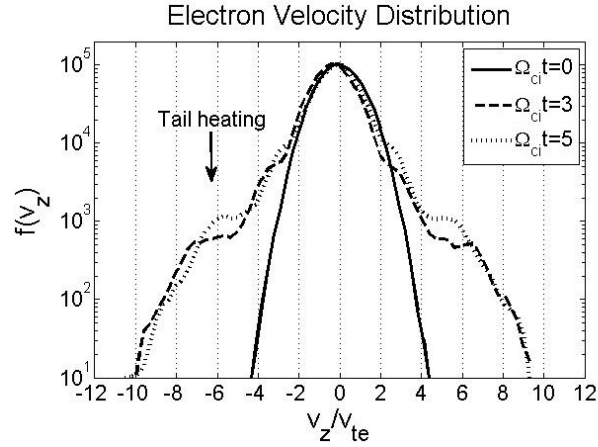
Figure 5.15: Time evolution of the distribution of the electron velocity along the magnetic field for the simulation of Figure 5.10. Note that the IA decay instability generates strong electron tail heating.

Note that in the absence of collisions, as expected, heating along the magnetic field is more significant. However, heating across the magnetic field is more efficient when collisions are included since electron-neutral collisions demagnetizes electrons and allows more efficient electron acceleration across the magnetic field. Therefore, in collisional simulations of the IA decay instability, the IB decay instability typically develops at the same time for sufficiently large shifts of the pump frequency from $2\omega_{ce}$.

It should be mentioned that the IA decay instability can be preferentially excited over the IB decay instability for stronger pump electric fields i.e. $v_{osc}/v_{te} \geq 1.5$ as well. As it was stated before, the analytical model also predicts that the stronger pump field excites the IA mode instead of the IB modes since the ions become unmagnetized due to large growth rate.

5.3   Summary

In this chapter results of the two-dimensional PIC-MCC simulation of the IB and IA parametric decay instabilities were presented. It was shown that both types of the parametric decay instabilities saturate in electron heating. The IB decay instability is associated with electron acceleration across the magnetic field. The IB spectral lines are generated simultaneously. As the pump frequency approaches $2f_{ce}$ the number of destabilized IB decay modes reduces. Heating across the magnetic field is also less than when the pump field has a small frequency offset relative to $2f_{ce}$. The IA parametric decay is associated with the electron acceleration along the magnetic field. There are evidences that the IA parametric decay instability is followed by a nonlinear caviton collapse process that enhances electron
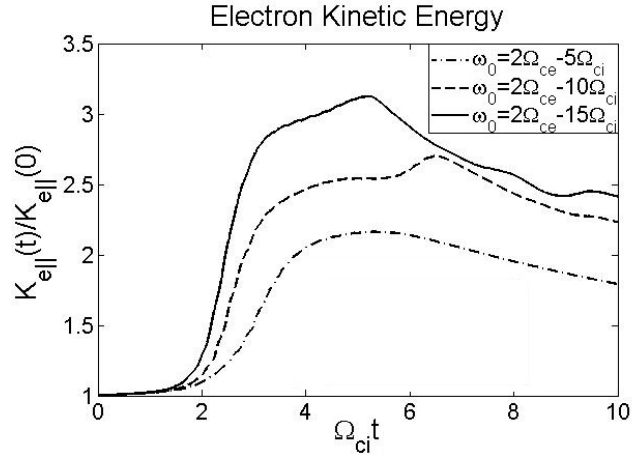
Figure 5.16: Evolution of the electron kinetic energy along the magnetic field for $v_{osc}/v_{te} = 0.9$ and $\theta_E = 22.9°$ for three simulations with $-5\Omega_{ci}$, $-10\Omega_{ci}$ and $-15\Omega_{ci}$ pump frequency offset relative to $2\Omega_{ce}$. Note that as the pump frequency approaches $2\Omega_{ce}$ heating reduces.

temperature more significantly. The IA parametric instability causes a strong tail heating in the electron velocity distribution function along the magnetic field. Electron heating reduces as the pump field approaches $2f_{ce}$.

Chapter 6

Discussion and Conclusions

In this study, new experimental observations of the discrete ion gyro-harmonic structures so called stimulated ion Bernstein scatter (SIBS) and the broadband spectral feature that maximizes near 500 Hz downshifted relative to the pump frequency named ion acoustic parametric decay (IAPD), are presented. These narrow band SEE spectral features are excited during heating around the second electron gyro-harmonic frequency. It is shown that the SIBS can be generated using low heater powers such as 0.8 MW (63 MW ERP). The IAPD feature appears in the power spectrum almost immediately after the heater turn-on which implies its faster growth in comparison to the discrete structures. It is also shown that during high power heating, i.e. $P_{heater} \geq 1.8$ MW (143MW ERP), in addition to the SIBS structures, another spectral line approximately 57 Hz downshifted from the pump appears in the spectrum. Different spectral features of this mode relative to the other structures, such as the threshold excitation transmission power, its strength, growth rate, bandwidth, frequency shift, damping and development time, are indicative of another generation mechanism, possibly magnetized stimulated Brillouin scatter (MSBS). The threshold transmission power for the generation of this spectral feature is 1.8 MW that is by a factor of two higher than SIBS. This emission line may be due to the parametric decay of the EM pump wave into an electrostatic ion cyclotron (EIC) wave and backscattered EM wave. This parametric decay process occurs in the longer wavelength regime, e. g. $k_\perp \rho_{ci} \ll 1$. Whereas, neutralized IB parametric decay waves have $k_\perp \rho_{ci} \geq 1$. In this case some of the characteristics could be explained. Note for longer wavelengths equation 4.5 reduces to

$$\omega \approx \Omega_{ci} \left(1 + \frac{k_\perp^2 c_s^2}{\Omega_{ci}^2} \right).$$ (6.1)

This would explain the narrowness of the emission bandwidth and the smaller frequency shift, i.e. 57 Hz, observed in the data. Currently no kinetic theory calculations exist for MSBS which are required for this application and it is beyond the scope of the current work. A potential framework exists [*Stenflo*, 1994] and this is perhaps the subject of a future study.

Parametric decay of the UH/EB pump field into another UH/EB and neutralized IB waves

in the upper hybrid altitude is considered as a viable process for generation of the SIBS in the SEE spectrum. It is shown that the direction of the electric field component of the pump wave is changing from almost perpendicular to the geomagnetic field in the upper hybrid altitude to parallel to the geomagnetic field in the reflection altitude that is around 15km above. It is consistent with the results of the previous studies [*Lundborg and Thidé*, 1986; *Leyser*, 1991; *Bernhardt et al.*, 2009]. Since Bernstein waves are propagating almost perpendicular to the magnetic field, occurrence of the process in the upper hybrid altitude seems more reasonable than the reflection altitude. It is also shown that at $\theta_E \geq 7°$, the UH/EB pump field decays into another UH/EB mode and a broadband oblique IA mode that is consistent with the generation mechanism of the IAPD spectral feature. Although θ_E depends on the density of the ionosphere, it also should be roughly related to the transmitter beam angle. The digital ionosonde data corresponding to times when the IAPD spectral feature is observed clearly shows that the ionospheric density is much higher than when the discrete structures were observed. The pump EM wave experiences more bending in the denser ionosphere, implying higher θ_E. The profile of the ionosphere is estimated from the digital ionosonde data for the times that SIBS and IAPD are observed. These profiles are used to estimate the strength and direction of the electric field in the source upper hybrid layer. This evaluation confirms that when the IAPD feature is observed, the angle of the pump electric field is more off-perpendicular to the geomagnetic field in comparison to when the SIBS structures are observed. The analytical model predicts the growth rate of the oblique IA mode is by a factor of two larger than the neutralized IB modes. This prediction is in line with the experimental observation of the IAPD feature growing faster than the discrete ion gyro-harmonic spectral features.

It is demonstrated that the threshold electric field intensity for the proposed mechanism is approximately 6 V/m. This is much less than the 250 V/m which was predicted for generation process at the reflection altitude [*Bernhardt et al.*, 2011].

It is observed that the maximum growth rate of the neutralized ion Bernstein modes occurs when the pump frequency is slightly above the second electron gyro-harmonic frequency. Whenever the pump frequency is above the second electron gyro-harmonic frequency, the first or second harmonic has the highest growth rate. Higher harmonics such as the third, fourth, and even up to the eighth mode, have the highest growth rates when the pump frequency is below the second electron gyro-harmonic frequency and its offset frequency increases. Since in the experimental observations the third and the fourth modes have the fastest growth, it may be concluded that the transmitter frequency is below $2\Omega_{ce}$ which is in line with the digital ionosonde estimation of the electron gyro-frequency. A stronger pump field destabilizes more harmonics. It may also influence on the most excited mode, but the frequency of the pump field has the dominant effect. As the off-perpendicular angle θ_E of the pump field relative to the background magnetic field increases, the threshold pump field intensity reduces, the number of destabilized neutralized IB modes increases and gradually an oblique IA wave mode is excited instead of neutralized IB modes. It is shown that for a certain angle of the electric field, the oblique IA wave can be excited at large oblique angle of

propagation $\theta_k \geq 40°$. At higher electron temperatures, the ion Landau damping is reduced and the oblique IA wave may propagate near parallel direction to the magnetic field. Finally it is important to note that the theory predicts these structures are all excited most strongly in the interaction region where the pump frequency is within several kHz of $2\Omega_{ce}$. Such behavior has been observed in experiments where the pump frequency was swept through $2\Omega_{ce}$ [*Fu et al.*, 2013]. It should be noted that much of the same behavior described here is also observed at experiments near $3\Omega_{ce}$ [*Mahmoudian et al.*, 2013].

As was mentioned before, the IAPD spectral feature is most likely due to parametric decay into an IA wave that is excited at higher θ_E. It should be noted that the threshold electric field intensity for excitation of the oblique IA mode is higher than the neutralized IB modes, thus even at higher θ_E in the low power heating experiments, the SIBS structures are expected to be observed. The experiments reported in this study were carried out at the HAARP facility. It is recently shown that the IAPD feature is equivalent to another prominent SEE feature, the Downshifted Peak DP [*Leyser*, 2001] which has most thoroughly been investigated at the EISCAT facility for higher gyro-harmonic heating ($n > 2$) [*Mahmoudian et al.*, 2013]. The IAPD feature observed here for second electron gyro-harmonic heating may ultimately allow at least similar diagnostic information as the DP [*Tereshchenko et al.*, 2006].

In order to study nonlinear wave-particle and wave-wave interactions during development of the IB and IA parametric decay instabilities, a two dimensional PIC-MCC computational model is developed. The results of the simulation of the IB parametric instability in the source upper hybrid layer shows all the IB spectral lines are generated at the same time rather than cascading which is consistent with the theory and experimental observations. Growth rate of the IB decay instability approximately linearly scales with the pump field strength. The IB decay instability saturates in electron heating across the magnetic field. The electron kinetic energy efficiently increases while the IB instability is growing. Enhancement of the kinetic energy across the field after the saturation time is negligible. As the pump field frequency approaches sufficiently close to $2f_{ce}$, heating across the magnetic field reduces and fewer of the IB modes are destabilized. Therefore, excitation of a larger number of the IB modes is associated with more heating across the magnetic field.

All the experimental observations of the SIBS structures are reported during nighttime or near sunset [*Bernhardt et al.*, 2011; *Samimi et al.* 2012; 2013; *Mahmoudian et al.*, 2013]. The D region is absent during this time period. Thus, electron temperature is enhanced more efficiently by the heater. Recent experimental investigation confirms simultaneous observation of artificial airglow and the SIBS structures in the SEE spectrum [*Mahmoudian et al.*, 2013]. SIBS in the SEE spectrum and the artificial airglow are observed when the transmitter frequency is below $2f_{ce}$ [*Mahmoudian et al.*, 2013]. Previous experimental investigations indicate that above $2f_{ce}$ the artificial airglow is enhanced [*Kosch et al.*, 2005; 2007]. This enhancement is attributed to the development of the parametric decay instability and the oscillating two stream instability (OTSI) at the same time [*Kosch et al.*, 2007]. The model of Chapter 4 also predicts that above $2f_{ce}$, the growth rate of the IB parametric

instability is larger. Computational study of the heating above $2f_{ce}$ will be the subject of future investigation.

The IA parametric decay saturates in electron heating along the magnetic field. The electron kinetic energy along the magnetic field grows significantly while the IA parametric decay is developing and causes tail heating in the electron velocity distribution along the magnetic field.

The electron kinetic energy and the electrostatic field energy show characteristic cyclical behavior of growth and saturation. The corresponding wavenumber spectrum shows that as the instability continues to evolve, the wavelength of the destabilized high frequency mode reduces. While the wavelength is reducing, this wavemode intensifies, then weakens and ultimately disappears from the wavenumber spectrum. The electrostatic field energy maximizes at the same time that the destabilized wavemode in the wavenumber spectrum intensifies. Next while the destabilized wavemode in the wavenumber spectrum weakens, the electrostatic field energy also decays, however, the electron kinetic energy reaches to its maximum. Contours of the electric field intensity right after the field energy is maximized shows the electric field intensifies inside the electron density depletions. It implies that the electric field is trapped inside the electron density cavities. As it was mentioned before, this implies that the energy of the destabilized wavemode is transferred to the electrons. Another long wavelength wavemode is generated and this cycle repeats.

Comparison of these results and the previous studies [*Nicholson and Goldman*, 1978; *Weatherall et al.* (1982); *Dubois et al.*, 1990; 1993; *Newman et al.*, 1990] provide evidence that this process is caviton collapse. The high frequency wavemode in this process is the UH/EB wave that is generated by the IA parametric decay instability. This nonlinear process enhances the tail heating and accelerates electrons along the magnetic field significantly. This may have connection with generation of the artificial ionospheric layers. Recent experiments show simultaneous observation of the IAPD structure and the artificial ionospheric layer [*Bernhardt et al.*, 2013]. In summary, the results of this study indicate that the IAPD would be consistent as a superior diagnostic for efficient electron heating along the magnetic field as opposed to SIBS.

The simulation shows that the destabilized IA waves are propagating nearly along the magnetic field. This instability develops when the electron temperature is high, i.e., $T_e/T_i \geq 3$ which reduces the ion Landau damping. The results of the simulation for strong pump field, e.g. $v_{osc}/v_{te} \geq 1.5$ (not shown) indicates that the IA parametric instability develops for initial ratio $T_e/T_i = 1$. However, the development of the instability starts after electron temperature increases which as stated before reduces ion Landau damping. The simulation results for such a large pump field strength shows that the IB parametric decay instability does not develop. The large growth rate of the IA instability makes ions unmagnetized and does not allow the IB modes to develop.

Comparing the results of the simulations of the IA parametric decay indicate that similar to the IB decay instability, at small offset frequencies of the pump field relative to $2f_{ce}$ heating

is more efficient. As the transmitter frequency approaches sufficiently close to $2f_{ce}$ the electron heating along the magnetic field reduces. Therefore, in general the simulation results show that sufficiently close to $2f_{ce}$ for the both types of the parametric instabilities heating reduces. It is consistent with the measurements of the electron temperature during heating near third harmonic of the electron gyro-frequency, $(3f_{ce})$ [*Honary et al.*, 1995]. Note that the SIBS and IAPD SEE features are observed for the transmitter frequencies approximately $(2f_{ce} - 10\text{kHz}) \leq f_0 \leq 2f_{ce}$ [*Mahmoudian et al.*, 2013; *Fu et al.*, 2013]. There is no direct measurement of the electron temperature during heating near $2f_{ce}$. As it was mentioned before, *Kosch et al* [2005; 2007] report enhancement of the artificial airglow when the transmitter frequency is slightly above $2f_{ce}$ that is subject of the future computational modeling. Another investigation that confirms more efficient heating when the heater frequency has a small offset relative to $2f_{ce}$ is radar measurements of the field aligned irregularities (FAIs) [*Hysell et al.*, 2010]. The field aligned irregularities (FAIs) are slightly suppressed very close to $2f_{ce}$ while small offset of the transmitter frequency relative to $2f_{ce}$ generates strong FAIs [*Hysell and Nossa*, 2009; *Hysell et al.*, 2010]. The suppression of the FAIs very close to $2f_{ce}$ is not comparable to the suppression of the FAIs during heating near the third or higher harmonics of electron gyro-frequency [*Hysell et al.*, 2010]. PIC simulation of the OTSI instability that is responsible for the conversion of the EM wave into an ES UH/EB wave will be the subject of future study since it is easily adaptable to the model framework used here. The FAIs are generated by the ES UH/EB waves [*Huang and Kuo*, 1994].

The current simulation model considers parametric decay instability in the source upper hybrid layer and is a local model. It is the first step in providing a global model for the generation of the SEE. The SEE received on the ground is an EM wave generated in the source region while the high frequency decay modes considered with the local model of this study are ES UH/EB waves. These ES waves must of course convert back to the downward-propagating EM waves. The nonlinear beat electric current that forms in the interaction region by the high frequency UH/EB decay mode ($\vec{J} = -en_e\vec{v_e}$) may work as an antenna as the source of the EM wave [*Zhou et al.*, 1994]. This nonlinear beat current can be obtained from the local PIC computational model. The vector potential and the electric and magnetic field of the down propagating EM wave can be easily calculated from the beat electric current [*Zhou et al.*, 1994].

6.1 Future Works

A number of unanswered questions still remain about the SEE spectral features discussed here and more experiments are warranted. At this time, the distinguishing observational characteristics of the SIBS and IAPD spectra are ionospheric density gradient related as described in Chapter 2. More systematic experiments, guided by the theoretical predictions here, are required to definitively determine the conditions for the transition from the SIBS to IAPD spectral features. The IAPD feature is equivalent to the DP observed during heat-

ing below $3f_{ce}$ [*Leyser*, 2001]. Previous experimental observations show that as the pump frequency goes above the harmonic of electron gyro-frequency, the BSS is excited instead of the DP [*Leyser*, 2001]. It is subject of further experiments if SIBS structures are observed for heating above $2f_{ce}$. Comparison of the SEE spectral features during heating below and above $2f_{ce}$ helps in understanding the physics of the instabilities. Recent experimental studies show simultaneous observation of the SIBS and the artificial airglow during heating below $2f_{ce}$ [*Mahmoudian et al.*, 2013]. On the other hand, it is reported that the artificial airglow enhances during heating above $2f_{ce}$ [*Kosch et al.*, 2005; 2007]. In order to study the association of the artificial airglow and the SIBS in the SEE spectrum, more experiments should be conducted to see if stronger SIBS structures will be observed during heating above $2f_{ce}$ as well. Careful experimental comparison of the artifcial airglow and the SEE in the future provides clue toward understanding the physics of these processes. It is found the IAPD feature is associated with the artificial airglow. In the future temporal characteristics of the IAPD feature while the artificial layers are evolving should be investigated to understand the generation mechanism of the artificial layers. The development of the OTSI and more importantly the resonance instability can cause wave trapping which results in the hysteresis behavior of the ionosphere called preconditioning [*Hysell and Nossa*, 2009; *Wright et al.*, 2009]. The preconditioning effects on the threshold and evolution of the SIBS SEE spectral features should be the subject of the future experiments.

The 2D computational model that is developed in this study should be used to look at other aspects of the heating as well. In the first step, heating above $2f_{ce}$ should be considered in the future. The results should be compared with the current investigation. It is reported that the FAIs and the artificial airglow are suppressed during heating near the third or higher harmonics of the electron gyro-frequency. On the other hand, during heating near $2f_{ce}$ these phenomena are enhanced [*Fialer*, 1974; *Djuth et al.*, 2005; *Kosch*, 2007; *Hysell and Nossa*, 2009]. Computational modeling of the heating near higher harmonics of the electron gyro-frequency should be considered in the future to understand these different behaviors of the ionosphere. There is of course potential for assessing the connection of other SEE features with airglow and artificial ionization layer formation at the higher electron gyro-harmonics.

In the current model, a simple elastic electron-neutral collision is included. In order to study the association of the SEE features, the artificial airglow and the generation of the artificial ionized layers, it is important in the future investigation to incorporate the electron-neutral excitation collision and the ionization collision in the model [*Birdsall*, 1991].

Furthermore, consideration of the multi-ion species in the model is appealing due to the recent experimental observations of the H^+ spectral lines in the SEE spectrum [*Bordikar et al.*, 2013]. Consideration of the density gradient in the model allows looking at the development of the parametric decay instability over an altitude range. It will provide a more accurate picture of the source region of the various SEE features. Two-dimensional modeling including density gradient and more realistic collisions is the next step that would lead us toward having a global model of the generation of SEE.

This model should be employed to study the OTSI as well. The OTSI is responsible for the conversion of the EM wave into an ES UH/EB wave that generates FAIs in the ionosphere. The conversion of the EM wave into an ES UH/EB wave is a prerequisite for the generation of some of the SEE spectral features [*Huang and Kuo*, 1994]. In the future, this model may be used to study the evolution of the OTSI and the IB and IA parametric decay instabilities at the same time. This computational modeling along with the experimental observation will determine the association of the FAIs and the narrow-band SEE characteristics.

Appendix A

Details of Experiments

In this appendix, procedure of all the conducted experiments in August 2011 and July 2012 at HAARP facilities are provided. Purposes of the experiments and the ionospheric conditions are briefly explained.

A.0.1 Effect of the Transmitter Duty Cycle

This experiment performed on July 21, 2011 at 10:02 UT - 10:25 UT which is local nighttime (02:02 AKT - 02:25 AKT) and July 23, 2011 at 04:38 UT - 04:58 UT which is local daytime (20:38 AKT - 20:58 AKT). The heater was working at full power, i.e., 3.6 MW. The heater beam was pointed to magnetic zenith with an azimuth of 202 degrees and a zenith angle of 14 degrees. In the first experiment the transmitter frequency was set to 2.85 MHz. The center frequency in the second experiment was 2.96 MHz. These frequencies were selected based on the digital ionosonde evaluation of the reflection altitude. Table A.1 shows the heater duty cycle in each experiment.

Figure A.1 shows two examples of the ionogram corresponding to the time period of these experiments. The SIBS in the SEE spectra were observed during the experiment on July 21. The reflection altitude as shown in Figure A.1 was roughly 250 km. The geomagnetic

Table A.1: Change of the heater duty cycle to study the effect of the heating time on the SEE characteristics.

Date	1	2	3	4	5	6
06/21/2011	30 s on/off	60 s on/off	90 s on/off	120 s on/off	180 s on/off	240 s on/off
06/23/2011	60 s on/off	90 s on/off	120 s on/off	150 s on/off	180 s on/off	
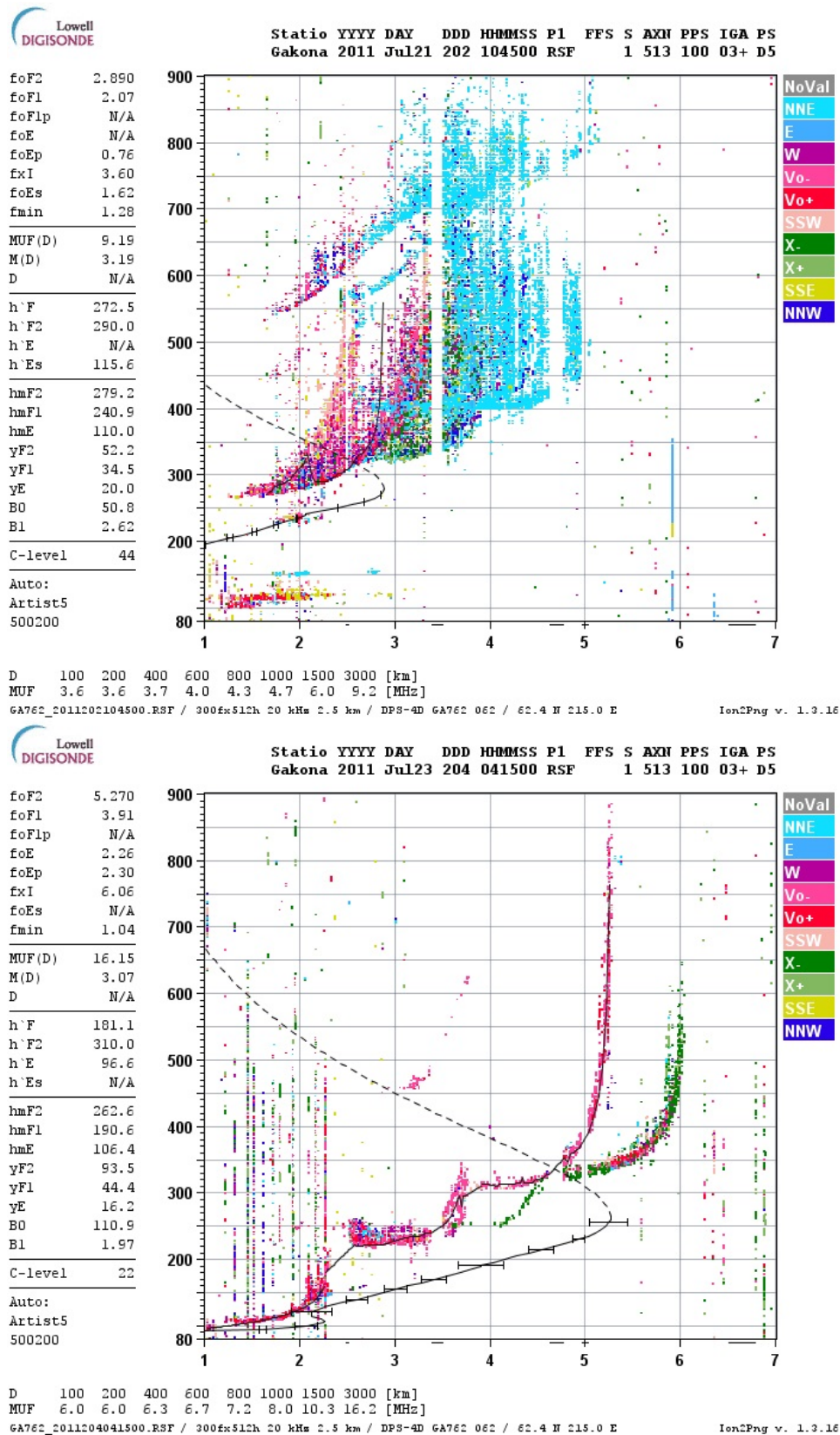
Figure A.1: Two sample ionograms corresponding to the time period of the experiments that study the heater duty cycle. The top panel is ionogram of July 21, 2011 at 10:45 UT and the bottom panel of July 23, 2013 at 04:15 UT.

field strength above HAARP is estimated to be $B_0 = 50524.8$ nT using the IGRF model. Correspondingly, the electron gyro-frequency is at $f_{ce} = 1.412$ MHz and ion gyro-frequency is at $f_{ci} = 48.07$ Hz. The SIBS structures were recorded in the experiments where the heater duty cycle was more than 90 sec on and 90 sec off. Furthermore, the power spectrum of the experiments with longer duty cycles shows sharper discrete structures. However, the digital ionosonde data did not show the ionosphere before 10:05 UT which may be due to strong absorption. The experiments for which the heater duty cycle was less than 90 sec and on 90 sec off were conducted before 10:07 UT. Therefore it was not possible to conclusively determine the correlation of the SIBS structures and the heating cycle.

A.0.2   Effect of the Transmitter Power and Preconditioning

This experiment was performed in both of the campaigns in 2011 and 2012. The first experiment was conducted on July 21, 2011 from 10:26 UT - 11:01 UT. The goal of this experiment was to simply measure the minimum transmitter power that is required to excite the SIBS structures. The transmitter frequency in this experiment was 2.85 MHz and the beam angle was toward magnetic zenith. The heater duty cycle was 2 minutes on and 2 minutes off. The ionospheric condition was quite similar to what is displayed in the top panel of Figure A.1. The frequency power spectrum recorded during this time period shows SIBS structures. The threshold transmitter power of 0.8 MW (63 MW ERP) was measured. In 2012, the purpose of the experiment was to study the ionospheric preconditioning effect on the SEE characteristics. Experimental studies show that the threshold power that generates the artificial field aligned irregularities (FAIs) is reduced after the FAIs were formed in the ionosphere [*Fialer*, 1974; *Erukimov et al.*, 1987; *Stubbe et al.*, 1982; *Jones et al.*, 1983; *Wright et al.*, 2006; *Nossa et al.*, 2009; *Wright et al.*, 2009]. The FAIs are generated by the upper hybrid wave through the thermal oscillating two stream instability (OTSI) which is also called thermal instability [*Grach et al.*, 1978; *Das and Fejer*, 1979; *Inhester et al.*, 1981; *Dysthe et al.*, 1983; *Huang and Kuo*, 1994]. In this process the pump wave converts to the UH waves and the purely growing modes [*Mishin et al.*, 2005; *Hysell et al.*, 2011]. This process develops in the order of a second [*Mishin et al.*, 2005]. The generated UH waves heat the plasma through collision. The differential thermal force that is produced in the heated plasma increases intensity of the FAIs. The UH waves are trapped in the depleted areas of the electron density which results in the development of the resonance instability [*Inhester*, 1982; *Dysthe et al.*, 1982; *Vaskov and Gurevich*, 1984] and consequently explosive growth of the FAIs. The hysteresis behavior of the FAIs are attributed to the resonance instability and trapping of the UH waves in the depleted areas [*Grach et al.*, 1978; *Dysthe et al.*, 1982; *Hysell and Nossa*, 2009]. Observation of the preconditioning effect for the SEE characteristics would be a strong evidence of the association of the FAIs and the SEE characteristics. The simultaneous coherent scatter radar measurements while the SEE characteristics are observed, is another method to study the association of the FAIs and the SEE characteristics. However, the HAARP facilities lack a strong coherent scatter radar to

Table A.2: Time table of the experiments investigating threshold excitation level and the preconditioning effect.

Date	Time Interval (UT)	Center Frequency (MHz)	Goal of Experiment
07/21/2011	10:26 - 11:01	2.85	Threshold Power
08/06/2012	02:05 - 02:22	2.98	Preconditioning
08/08/2012	02:37 - 02:48	2.95	Preconditioning
08/08/2012	02:48 - 02:59	3.05	Preconditioning
08/09/2012	10:01 - 10:03	2.80	Preconditioning
08/09/2012	10:23 - 10:25	4.30	Preconditioning

scan the ionosphere. The experiment that was designed had two phases. In the first phase, the transmitter power was reduced in 1 dB steps from the full power and the heating cycle was 45 seconds on and 45 seconds off. The off time lets the irregularities disappear. Then, in the second phase, after heating the ionosphere for 60 seconds, the transmitter power reduced in 1dB steps. However, there was no off time in between the power steps. If the upper hybrid waves and the corresponding FAIs are generated, the SEE characteristics must be sustained for the lower transmitter power. The preconditioning effects were investigated on August 6, 8 and 9, 2012. Table A.2 shows the time of each experiment and the transmitter frequency. The experiment on August 9, 2012 was only on the second phase in which the transmitter power reduced without off time in between the power steps. Figure A.2 shows evaluation of the digital ionosonde from the ionosphere on August 6 and 8, 2012. The ionosphere was quiet on August 6, 2012. However, the reflection altitude was around 100 km which is relatively low. In other words, the E region of the ionosphere was in fact heated. In the E region the collision frequency is high which increases the threshold excitation level of the parametric instability. Thus no SEE were observed during this experiment. On August 8, 2012, the ionosphere was absent and no SEE was excited. On August 9, 2012, as is shown in Figure A.3, a sporadic E layer existed at the time of the experiment. The EM wave is absorbed by the sporadic E layer. Under this circumstance, the F layer of the ionosphere is not exposed to a strong pump wave. Therefore, again no SEE were observed. In summary, the preconditioning experiments were not successful.

A.0.3   Effect of the Transmitter Beam Angle

Angle of the electric field relative to the geomagnetic field is one of the parameters that affects the parametric instability. This angle depends on the density profile of the ionosphere which is explained in Chapter 3. Direction of the propagation of the EM pump field also affects the angle of the electric field in the interaction region. A set of experiments was designed in both of the research campaigns in 2011 and 2012 to study the effect of the transmitter beam angle
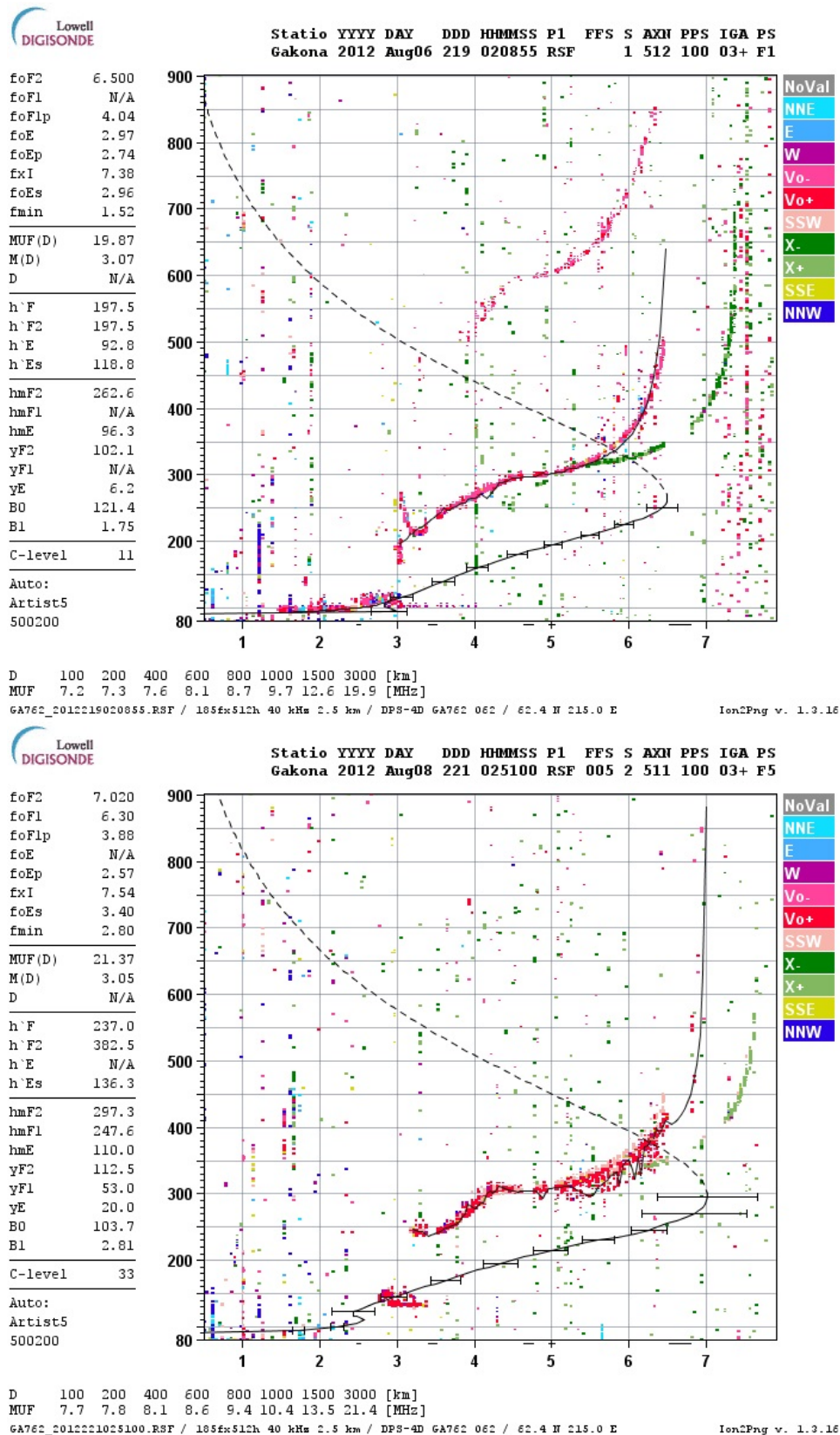
Figure A.2: The ionograms corresponding to the experiments investigating the ionospheric preconditioning effect. The top panel is ionogram of August 6, 2012 at 02:08 UT and the bottom panel of August 8, 2012 at 02:51 UT.

Table A.3: Time table, the transmitter frequency and beam angle of the antenna for the experiments investigating the effect of the direction of the propagation on the SEE characteristics.

Date	Time (UT)	Frequency (MHz)	ZA angle (degrees)	AZ angle (degrees)
07/25/2011	04:18 - 04:48	2.96	-4;0;4;8;12;14;16;20;24;28	202
07/25/2011	10:48 - 10:52	2.96	14	193;198;202;207;213
08/08/2012	10:43 - 10:48	2.80	2;7;12;14;16;21;26	200
08/08/2012	10:48 - 10:52	2.80	14	193;198;202;207;213
08/08/2012	10:52 - 10:57	2.90	2;7;12;14;16;21;26	200
08/08/2012	10:57 - 11:01	2.90	14	193;198;202;207;213
08/09/2012	10:03 - 10:08	2.80	2;7;12;14;16;21;26	200
08/09/2012	10:08 - 10:12	2.80	14	193;198;202;207;213
08/09/2012	10:13 - 10:15	2.90	2;7;12;14;16;21;26	200
08/09/2012	10:15 - 10:22	2.90	14	193;198;202;207;213

on the SEE characteristics. Table A.3 shows date, time, the transmitter frequency, the off zenith angle (ZA) and the azimuth angle (AZ) of the antenna beam during each experiment. The transmitter was working in full power, i.e. 3.6 MW.

The ionospheric condition at the time of these experiments is shown in Figure A.3. A sporadic E layer existed on August 8 and 9, 2012 at the time of these experiments. However, the classic SEE features such as the broad symmetric structure (BSS), the DM and the UM were observed. The SIBS structures characteristic which is the subject of interest in this study was not observed. Note that the BSS is generated when the pump frequency is above the harmonics of the electron gyro-frequency [*Leyser*, 2001]. The transmitter frequency was below the second electron gyro-frequency in the experiments where the SIBS structures were observed. Further experiments are required to determine if the SIBS are excited above the second electron gyro-harmonic. During the experiment on July 25, 2011, the ionosphere was very quite and the maximum critical frequency was 5.1 MHz according the digital ionosonde data. However, the only SEE characteristic observed in two occasions was spectral lines ordered near the harmonics of 800 Hz. These spectral lines are observed for the first time in these experiments. It is shown that these spectral lines are generated by Oxygen-Hydrogen (i.e. $O^+ - H^+$) (or Buchsbaum [*Buchsbaum*, 1960]) hybrid wave [*Bordikar et al.*, 2013]. It may be possible to estimate the density of the minor ion species, i.e. H^+, in the ionosphere by measuring the frequency shift of these spectral lines relative to the transmitter frequency [*Bordikar et al.*, 2013]. Under the normal ionospheric condition, the H^+ density is negligible at around 150 km reflection altitude. The only possibility of having enough H^+ species for the $O^+ - H^+$ hybrid mode, is the active ionospheric condition during which the proton precipitation is high. The riometer data, magnetometer measurements and satellite data

confirm the disturbed ionospheric condition at this time. It might be the reason that in spite of the picture of the quite ionosphere from the ionogram, none of the classic SEE features were observed during this time period.

A.0.4   Effect of the Transmitter Frequency

It has been observed from the beginning of the heating experiment that the SEE characteristics, the artificial FAIs and the artificial airglow are sensitive to the transmitter frequency. This sensitivity is very well reported when the transmitter frequency is near the harmonics of the electron gyro-frequency, i.e. $n\Omega_{ce}$ [*Sipler and Biondi*, 1972; *Haslett and Megill*, 1974; *Fialer*, 1974; *Leyser et al.*, 1992; *Honary et al.*, 1999; *Leyser*, 2001; *Kosch et al.*, 2007; *Hysell et al.*, 2010]. The goal of this experiment was to study the behavior of the narrow band SEE characteristics when the transmitter frequency is close to $2\Omega_{ce}$. Two types of experiments were designed. In one experiment, the transmitter frequency was changed in discrete steps and there was off time between the heating cycles. In the second type, the ionosphere was heated for 1 minute at a constant frequency and then the transmitter frequency was sweeping slowly and continuously to higher frequencies, i.e. FM modulation. The second type was similar to the experiment conducted by *Pedersen et al.* [2010; 2011] during which the artificial ionospheric layer was generated below the F layer. Since the altitude of the new layers is less than the reflection altitude, the corresponding electron gyro-frequency is higher. The frequency sweeping tunes the transmission frequency to the reflection altitude of the new layer. As the new layer is moving downward, the transmission frequency tunes to its reflection altitude and makes heating of the new layer more efficient. Thus, the frequency sweeping helps in sustaining the new layers for a longer time. The objects of the experiments were 1) to see if any of the SEE characteristics are associated with the artificial layer and 2) to investigate the capability of using the SEE characteristics for tracking the artificial layer while it is moving downward. Table A.4 shows the data, the time, the transmitter frequency, the heating cycle, and the type of the experiments. The transmitter points to magnetic zenith in all of these experiments.

The ionograms that are shown in Figure A.1- A.3 describe the ionospheric condition during these experiments as well. The other times that have not been discussed yet are August 6, 09:45 UT - 10:35 UT and August 7, 00:13 UT - 00:31 UT. Figure A.4 shows two examples of the ionosphere corresponding to the latter times. On August 6, 09:45 UT - 10:35 UT, there was a strong sporadic E layer in the ionosphere which as mentioned before absorbs the pump wave. The ionosphere was wiped out on August 7, 00:13 UT - 00:31 UT according to the ionogram. Therefore, no SEE characteristics were observed in these time periods.

Figure A.3: The ionograms corresponding to the experiments investigating the effect of the direction of the transmitter beam angle. a) July 25, 2011, 04:29 UT b) August 8, 2012, 10:42 UT, and c) August 9, 2012, 10:23 UT.

Table A.4: Time table, the transmitter frequency, the heating cycle and the type of the experiments investigating the effect of the transmitter frequency on the SEE characteristics.

Date	Time (UT)	Frequency (MHz)	Heating Cycle	Experiment Type
07/23/2011	03:56 - 04:11	4.24;4.25;4.26;4.27;4.28	90 s on/off	Discrete steps
07/23/2011	04:11 - 04:26	4:29;4.30;4.31;4.32;4.33	90 s on/off	Discrete steps
07/23/2011	04:26 - 04:37	4.34;4.35;4.36;4.37	90 s on/off	Discrete steps
07/25/2011	03:48 - 04:02	2.86;2.88;2.90;2.92;2.94	90 s on/off	Discrete steps
07/25/2011	04:02 - 04:17	2.96;2.98;3.00;3.02;3.04	90 s on/off	Discrete steps
08/06/2012	02:22 - 02:28	2.70;2.725;2.75;2.775	45 s on/off	Discrete steps
08/06/2012	02:28 - 02:34	2.80;2.825;2.85;2.875	45 s on/off	Discrete steps
08/06/2012	02:34 - 02:41	2.90;2.925;2.95;2.975;3.00	45 s on/off	Discrete steps
08/06/2012	02:41 - 02:47	4.10;4.125;4.15;4.175	45 s on/off	Discrete steps
08/06/2012	02:47 - 02:53	4.20;4.225;4.25;4.275	45 s on/off	Discrete steps
08/06/2012	02:53 - 02:59	4.30;4.325;4.35;4.375;4.40	45 s on/off	Discrete steps
08/06/2012	09:45 - 09:48	2.70;2.70-2.80	60 s;150 s on	FM sweep
08/06/2012	09:48 - 09:52	2.70;2.70-2.80	60 s;150 s on	FM sweep
08/06/2012	09:55 - 10:01	4.10;4.10-4.30	60 s;300 s on	FM sweep
08/06/2012	10:02 - 10:05	2.70;2.70-2.80	60 s;150 s on	FM sweep
08/06/2012	10:05 - 10:09	2.80;2.80-2.90	60 s;150 s on	FM sweep
08/06/2012	10:12 - 10:18	4.10;4.10-4.30	60 s;300 s on	FM sweep
08/06/2012	10:19 - 10:22	2.70;2.70-2.80	60 s;150 s on	FM sweep
08/06/2012	10:22 - 10:26	2.80;2.80-2.90	60 s;150 s on	FM sweep
08/06/2012	10:29 - 10:35	4.10;4.10-4.30	60 s;300 s on	FM sweep
08/07/2012	00:10 - 00:13	2.70;2.70-2.80	60 s;150 s on	FM sweep
08/07/2012	00:13 - 00:17	2.80;2.80-2.90	60 s;150 s on	FM sweep
08/07/2012	00:20 - 00:31	4.10;4.10-4.30	60 s;300 s on	FM sweep
08/08/2012	02:00 - 02:03	2.70;2.70-2.80	60 s;130 s on	FM sweep
08/08/2012	02:03 - 02:06	2.70;2.70-2.80	60 s;130 s on	FM sweep
08/08/2012	02:07 - 02:12	4.10;4.10-4.30	60 s;240 s on	FM sweep
08/08/2012	02:12 - 02:15	2.70;2.70-2.80	60 s;130 s on	FM sweep
08/08/2012	02:15 - 02:19	2.70;2.70-2.80	60 s;130 s on	FM sweep
08/08/2012	02:19 - 02:24	4.10;4.10-4.30	60 s;130 s on	FM sweep
08/08/2012	02:24 - 02:28	2.70;2.70-2.80	60 s;130 s on	FM sweep
08/08/2012	02:28 - 02:31	2.70;2.70-2.80	60 s;130 s on	FM sweep
08/08/2012	02:31 - 02:36	4.10;4.10-4.30	60 s;240 s on	FM sweep
08/08/2012	10:30 - 10:34	2.70;2.725;2.75;2.775	45 s on/20 s off	Discrete steps
08/08/2012	10:34 - 10:38	2.80;2.825;2.85;2.875	45 s on/20 s off	Discrete steps
08/08/2012	10:38 - 10:42	2.90;2.925;2.95;2.975	45 s on/20 s off	Discrete steps
08/09/2012	09:35 - 09:40	2.775;2.80;2.825;2.85;2.875	45 s on/20 s off	Discrete steps
08/09/2012	09:40 - 09:42	2.90;2.925;2.95;2.975	45 s on/20 s off	Discrete steps
08/09/2012	09:43 - 09:49	2.70;2.70-2.80	60 s;120 s on	FM sweep
08/09/2012	09:49 - 09:55	2.80;2.80-2.90	60 s;120 s on	FM sweep
08/09/2012	09:56 - 10:00	4.10;4.10-4.30	60 s;240 s on	FM sweep
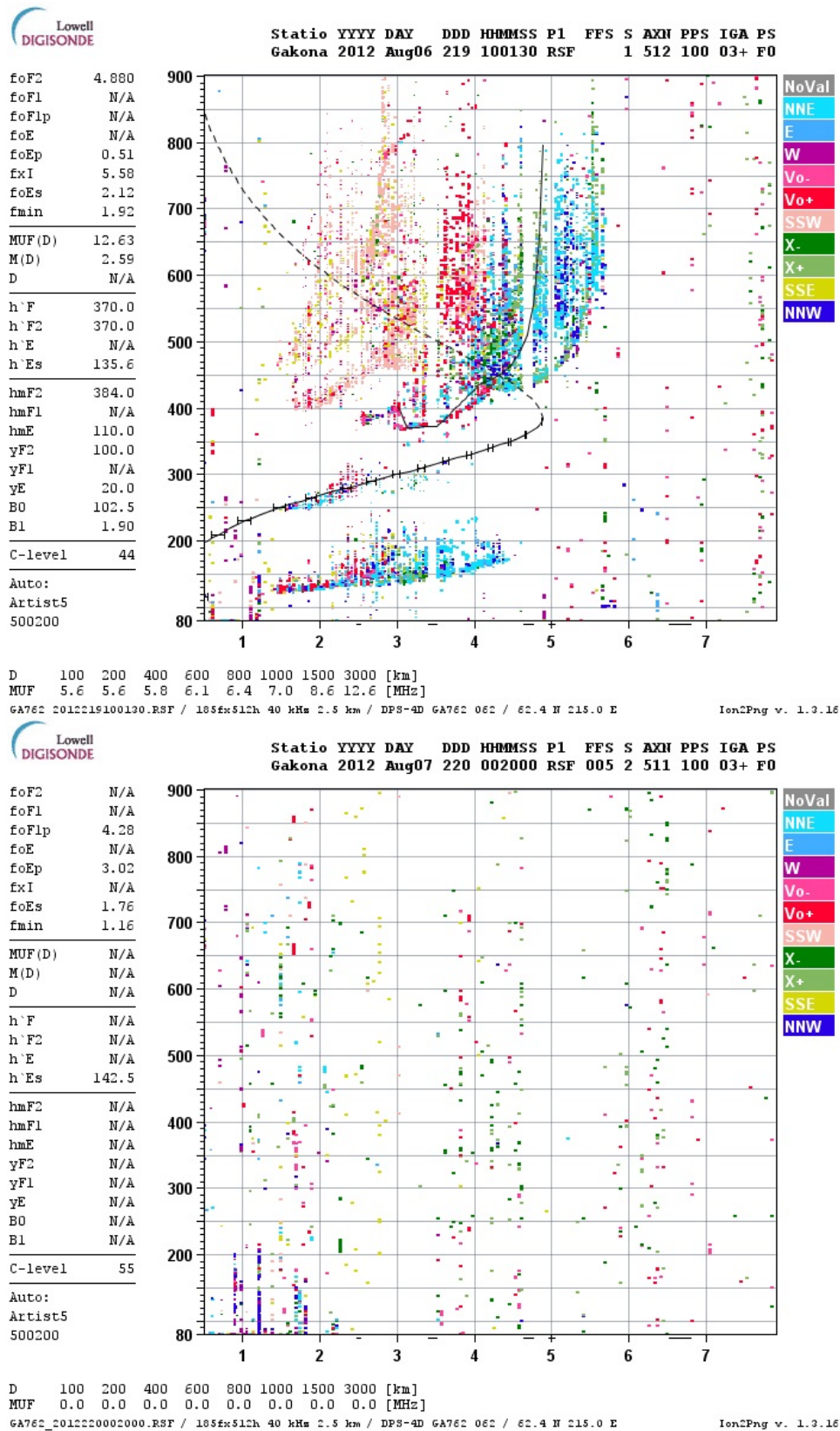
Figure A.4: The ionograms corresponding to the experiments investigating the effect of the transmitter frequency. The top panel is ionogram of August 6, 2012 at 10:13 UT and the bottom panel of August 7, 2012 at 00:20 UT.

Appendix B

Parametric Decay Instability

In this appendix, parametric decay instability in plasma is considered in more detail. The purpose of the first part is to explain the physics of the parametric instability. Fluid equations are used to explain the parametric decay instability in an unmagnetized plasma. It is a simple model that provides a good picture of the physics of the instability. Next, a more sophisticated kinetic model in the magnetized plasma using Vlasov equation is employed to derive the general dispersion relation (Equation 4.2) of the parametric decay instability.

B.1   Fluid description of the parametric decay instability in unmagnetized plasma

In this section, parametric decay instability in a uniform unmagnetized plasma medium is explained using fluid model. For simplicity a one dimensional model is considered. In the interaction region of the ionosphere, the wavelength of the EM pump wave is very long and dipole approximation ($k_0 = 0$) can be used.

$$E_p = E_0 \cos(\omega_0 t) \tag{B.1}$$

Fluid equation of motion, equation of continuity and Poisson's equation should be used to obtain the dispersion relation of the waves in plasma:

$$m_j n_j \left(\frac{\partial u_j}{\partial t} + (u_j.\nabla)u_j \right) = q_j n_j (E + E_0 \cos(\omega_0 t)) - \nabla p - m_j n_j (u_j - u_0)\nu \tag{B.2}$$

$$\frac{\partial n_j}{\partial t} + \nabla(n_j u_j) = 0 \tag{B.3}$$

$$\nabla.E = \frac{q(n_i - n_e)}{\epsilon_0} \tag{B.4}$$

where $p = n_j K T_j$ is pressure, K is Boltzmann constant and ν is collision frequency. The fluid velocity and density are superposition of the zero order terms due to the external pump field and perturbed first order terms:

$$
m_j(n_{j0} + n_{j1}) \left(\frac{\partial(u_{j0} + u_{j1})}{\partial t} + ((u_{j0} + u_{j1}).\nabla)(u_{j0} + u_{j1}) \right) =
$$
$$
q_j(n_{j0} + n_{j1})(E + E_0 \cos(\omega_0 t)) - \nabla(n_{j0} + n_{j1})KT_j - m_j(n_{j0} + n_{j1})((u_{j0} + u_{j1}) - u_0)\nu
$$
$$
\text{(B.5)}
$$

$$
\frac{\partial(n_{j0} + n_{j1})}{\partial t} + \nabla((n_{j0} + n_{j1})(u_{j0} + u_{j1})) = 0 \tag{B.6}
$$

Since the external pump field is high frequency, the ion species cannot oscillate at the same frequency and are stationary ($u_{i0} = 0$). Gradient of the zero order terms are zero ($\nabla u_{e0} = \nabla n_{e0} = 0$). Therefore, Equation B.5 and Equation B.6 can be broken into two equations as follows:

$$
m_j n_{j0} \frac{\partial u_{j0}}{\partial t} = q_j n_{j0} E_0 \cos(\omega_0 t) \Rightarrow m_j \frac{\partial u_{j0}}{\partial t} = q_j E_0 \cos(\omega_0 t) \Rightarrow u_{j0} = \frac{q_j E_0}{m_j \omega_0} \sin(\omega_0 t) \quad \text{(B.7)}
$$

$$
\frac{\partial n_{j0}}{\partial t} = 0 \tag{B.8}
$$

$$
m_j n_{j0} \frac{\partial u_{j1}}{\partial t} + m_j n_{j1} \frac{\partial u_{j0}}{\partial t} + m_j n_{j1} \frac{\partial u_{j1}}{\partial t} + m_j(n_{j0} + n_{j1}) \left((u_{j0}.\nabla)u_{j1} + (u_{j1}.\nabla)u_{j1} \right) =
$$
$$
q_j(n_{j0} + n_{j1})E + q_j n_{j1} E_0 \cos(\omega_0 t) - \nabla n_{j1} KT_j - m_j(n_{j0} + n_{j1})u_{j1}\nu
$$
$$
\text{(B.9)}
$$

$$
\frac{\partial n_{j1}}{\partial t} + \nabla(n_{j0}u_{j1} + n_{j1}u_{j0} + n_{j1}u_{j1}) = 0 \tag{B.10}
$$

Note that Equation B.7 is only valid for electrons and ions cannot oscillate at such a high frequency. Equation B.9 can be broken into two equations again:

$$
m_j n_{j1} \frac{\partial u_{j0}}{\partial t} = q_j n_{j1} E_0 \cos(\omega_0 t) \Rightarrow m_j \frac{\partial u_{j0}}{\partial t} = q_j E_0 \cos(\omega_0 t) \tag{B.11}
$$

$$
m_j n_{j0} \frac{\partial u_{j1}}{\partial t} + m_j n_{j1} \frac{\partial u_{j1}}{\partial t} + m_j(n_{j0} + n_{j1}) \left((u_{j0}.\nabla)u_{j1} + (u_{j1}.\nabla)u_{j1} \right) =
$$
$$
q_j(n_{j0} + n_{j1})E - \nabla n_{j1} KT_j - m_j(n_{j0} + n_{j1})u_{j1}\nu
$$
$$
\text{(B.12)}
$$

Note that Equation B.7 and Equation B.11 are equivalent. The second and third order terms in Equation B.10 and Equation B.12 should be neglected:

$$m_j n_{j0} \frac{\partial u_{j1}}{\partial t} + m_j n_{j0}(u_{j0}.\nabla)u_{j1} = q_j n_{j0} E - \nabla n_{j1} KT_j - m_j n_{j0} u_{j1} \nu \qquad (B.13)$$

$$\frac{\partial n_{j1}}{\partial t} + \nabla(n_{j0}u_{j1} + n_{j1}u_{j0}) = 0 \qquad (B.14)$$

If the spatial Fourier transform is defined by the e^{jkx} coefficient:

$$\nabla \rightarrow -jk \qquad (B.15)$$

Equation B.13 and Equation B.14 in the spatial Fourier domain have the following forms:

$$m_j n_{j0} \frac{\partial u_{j1}}{\partial t} - jk m_j n_{j0} u_{j0} u_{j1} = q_j n_{j0} E + jk n_{j1} KT_j - m_j n_{j0} u_{j1} \nu \qquad (B.16)$$

$$\frac{\partial n_{j1}}{\partial t} - jk n_{j0} u_{j1} - jk n_{j1} u_{j0} = 0 \qquad (B.17)$$

We should devide Equation B.16 by $m_j n_{j0}$.

$$\frac{\partial u_{j1}}{\partial t} - jk u_{j0} u_{j1} = \frac{q_j}{m_j}(1 + \frac{n_{j1}}{n_{j0}})E + jk \frac{n_{j1}}{m_j n_{j0}} KT_j - u_{j1} \nu \qquad (B.18)$$

Time derivative of Equation B.17 gives:

$$\frac{\partial^2 n_{j1}}{\partial t^2} - jk n_{j0} \frac{\partial u_{j1}}{\partial t} - jk n_{j1} \frac{\partial u_{j0}}{\partial t} = 0 \qquad (B.19)$$

Note that $n_{e0} = n_{i0} = n$ and $u_{i0} = 0$. Since frequency and timescales of the electrons and ions are different, each of them should be considered separately.

$$\frac{\partial u_{e1}}{\partial t} - jk u_{e0} u_{e1} = \frac{-q}{m_e}E + jk \frac{n_{e1}}{m_e n} KT_e - u_{e1} \nu \qquad (B.20)$$

$$\frac{\partial u_{i1}}{\partial t} = \frac{q}{m_i}E + jk \frac{n_{i1}}{m_i n} KT_i - u_{i1} \nu \qquad (B.21)$$

$$\frac{\partial^2 n_{e1}}{\partial t^2} - jk n \frac{\partial u_{e1}}{\partial t} - jk n_{e1} \frac{\partial u_{e0}}{\partial t} = 0 \qquad (B.22)$$

$$\frac{\partial^2 n_{i1}}{\partial t^2} - jk n \frac{\partial u_{i1}}{\partial t} = 0 \qquad (B.23)$$

Electrons have a high frequency terms due to the pump wave and a low frequency terms due to the ions that drag the electrons. Therefore, Equation B.20 can be broken into two equations representing the high and low frequency terms separately [*Chen*, 1983]:

$$\frac{\partial u_{eh1}}{\partial t} = \frac{-q}{m_e}E_h + jk\frac{n_{eh1}}{m_e n}KT_e - u_{eh1}\nu \tag{B.24}$$

$$-jku_{e0}u_{eh1} = \frac{-q}{m_e}E_l + jk\frac{n_{el1}}{m_e n}KT_e \tag{B.25}$$

Since u_{e0} and u_{eh1} are high frequency terms, their beating gives a low frequency electric field. Note that since ions drag the low frequency electrons, approximately $n_{el1} \approx n_{il}$ and $u_{el1} \approx u_{i1}$. In order to find the high frequency electron density fluctuations, Equation B.24 should be exerted into Equation B.22:

$$\frac{\partial^2 n_{eh1}}{\partial t^2} - jkn\left(\frac{-q}{m_e}E_h + jk\frac{n_{eh1}}{m_e n}KT_e - u_{eh1}\nu\right) = jkn_{el1}\frac{\partial u_{e0}}{\partial t} \tag{B.26}$$

In order to find the dispersion relation, u_{eh1} should be calculated from Equation B.17:

$$\frac{\partial n_{eh1} + n_{el1}}{\partial t} - jknu_{eh1} - jknu_{el1} - jkn_{eh1}u_{e0} - jkn_{el1}u_{e0} = 0$$

$$\frac{\partial n_{eh1}}{\partial t} - jknu_{eh1} - jkn_{el1}u_{e0} = 0 \Rightarrow u_{eh1} = -j\frac{1}{kn}\frac{\partial n_{eh1}}{\partial t} - \frac{n_{el1}u_{e0}}{n} \tag{B.27}$$

$$\frac{\partial n_{el1}}{\partial t} - jknu_{el1} - jkn_{eh1}u_{e0} = 0 \Rightarrow u_{el1} = -j\frac{1}{kn}\frac{\partial n_{el1}}{\partial t} - \frac{n_{eh1}u_{e0}}{n} \tag{B.28}$$

Equation B.27 should be exerted into Equation B.26:

$$\frac{\partial^2 n_{eh1}}{\partial t^2} - jkn\left(\frac{-q}{m_e}E_h + jk\frac{n_{eh1}}{m_e n}KT_e - (-j\frac{1}{kn}\frac{\partial n_{eh1}}{\partial t} - \frac{n_{el1}u_{e0}}{n})\nu\right) = jkn_{el1}\frac{\partial u_{e0}}{\partial t} \tag{B.29}$$

The high frequency electric field can be obtained from Poisson's equation, $E_h = \frac{-jn_{eh}q}{k\epsilon_0}$, thus:

$$\frac{\partial^2 n_{eh1}}{\partial t^2} - jkn\left(\frac{-q}{m_e}(\frac{-jn_{eh}q}{k\epsilon_0}) + jk\frac{n_{eh1}}{m_e n}KT_e + (j\frac{1}{kn}\frac{\partial n_{eh1}}{\partial t} + \frac{n_{el1}u_{e0}}{n})\nu\right) = jkn_{el1}\frac{\partial u_{e0}}{\partial t}$$

$$\frac{\partial^2 n_{eh1}}{\partial t^2} + \left(\frac{nq^2}{m_e\epsilon_0} + \frac{k^2 KT_e}{m_e}\right)n_{eh} + \frac{\partial n_{eh1}}{\partial t}\nu = jkn_{el1}\frac{\partial u_{e0}}{\partial t} - jkn\frac{n_{el1}u_{e0}}{n} \tag{B.30}$$

Electron thermal velocity is defined:

$$v_{te} = \sqrt{\frac{KT_e}{m_e}} \tag{B.31}$$

The dispersion relation of the electron plasma wave, also called Langmuir wave is:

$$\omega_L^2 = \omega_{pe}^2 + k^2 v_{te}^2 \tag{B.32}$$

Equation B.30 can be simplified by using the Langmuir wave dispersion relation:

$$\frac{\partial^2 n_{eh1}}{\partial t^2} + \omega_L^2 n_{eh} + \frac{\partial n_{eh1}}{\partial t}\nu = jkn_{el1}\frac{\partial u_{e0}}{\partial t} - jkn_{el1}u_{e0}\nu \tag{B.33}$$

This is a simple harmonic oscillator equation for the high frequency electron fluctuations that generates Langmuir waves. The right hand side of the equation represents beating of the pump wave with the low frequency ion fluctuations.

In order to complete the feedback loop that is required for the parametric decay instability, we should show how the low frequency fluctuations are driven by the beating of the pump wave and the high frequency fluctuations. It can be shown by inserting Equation B.21 into Equation B.23. Remember that $n_{i1} = n_{el1}$ and $u_{i1} = u_{el1}$.

$$\frac{\partial^2 n_{i1}}{\partial t^2} - jkn\left(\frac{q}{m_i}E_l + jk\frac{n_{i1}}{m_i n}KT_i - u_{i1}\nu\right) = 0 \tag{B.34}$$

The low frequency electric field E_l can be obtained from Equation B.25 and the low frequency velocity u_{i1} from Equation B.28. Thus:

$$\frac{\partial^2 n_{i1}}{\partial t^2} - jkn\left(\frac{q}{m_i}\frac{jm_e k u_{e0}u_{eh1} + jk\frac{n_{el1}}{n}KT_e}{q} + jk\frac{n_{i1}}{m_i n}KT_i - (-j\frac{1}{kn}\frac{\partial n_{el1}}{\partial t} - \frac{n_{eh1}u_{e0}}{n})\nu\right) = 0$$

The high frequency electron velocity, u_{eh1}, can be obtained from Equation B.27.

$$\frac{\partial^2 n_{i1}}{\partial t^2} + k^2\frac{KT_e + KT_i}{m_i}n_{i1} + \frac{m_e n k^2 u_{e0}(-j\frac{1}{kn}\frac{\partial n_{eh1}}{\partial t} - \frac{n_{el1}u_{e0}}{n})}{m_i} + \nu\frac{\partial n_{el1}}{\partial t} = +jkn\frac{n_{eh1}u_{e0}}{n}\nu$$

$$\frac{\partial^2 n_{i1}}{\partial t^2} + k^2\frac{KT_e + KT_i}{m_i}n_{i1} - \frac{m_e k^2 n_{i1}u_{e0}^2}{m_i} + \nu\frac{\partial n_{el1}}{\partial t} = \frac{jm_e k u_{e0}}{m_i}\frac{\partial n_{eh1}}{\partial t} + jkn\frac{n_{eh1}u_{e0}}{n}\nu \tag{B.35}$$

From Equation B.7, u_{e0}^2 can be calculated:

$$u_{e0}^2 = \left(\frac{-qE_0}{m_e\omega_0}\sin(\omega_0 t)\right)^2 = \left(\frac{-qE_0}{m_e\omega_0}\right)^2\left(\frac{1 - \cos(2\omega_0 t)}{2}\right) \tag{B.36}$$

Obviously ions cannot oscillate at $2\omega_0$, therefore, only the first term of Equation B.36 should be retained in Equation B.35.

$$\frac{\partial^2 n_{i1}}{\partial t^2} + k^2\frac{KT_e + KT_i}{m_i}n_{i1} - \frac{m_e k^2 n_{i1}\left(\frac{-qE_0}{m_e\omega_0}\right)^2}{m_i}\frac{1}{2} + \nu\frac{\partial n_{el1}}{\partial t} = \frac{jm_e k u_{e0}}{m_i}\frac{\partial n_{eh1}}{\partial t} + jkn\frac{n_{eh1}u_{e0}}{n}\nu$$

$$\frac{\partial^2 n_{i1}}{\partial t^2} + k^2 \left(\frac{KT_e + KT_i}{m_i} - \frac{m_e}{2m_i} \left(\frac{-qE_0}{m_e\omega_0} \right)^2 \right) n_{i1} + \nu \frac{\partial n_{el1}}{\partial t} = \frac{jm_e k u_{e0}}{m_i} \frac{\partial n_{eh1}}{\partial t} + jkn \frac{n_{eh1}u_{e0}}{n} \nu$$

$$(B.37)$$

Since $\frac{KT_e + KT_i}{m_i} >> \frac{m_e}{2m_i} \left(\frac{-qE_0}{m_e\omega_0} \right)^2$, Equation B.37 can be simplified:

$$\frac{\partial^2 n_{i1}}{\partial t^2} + k^2 \frac{KT_e + KT_i}{m_i} n_{i1} + \nu \frac{\partial n_{el1}}{\partial t} = \frac{jm_e k u_{e0}}{m_i} \frac{\partial n_{eh1}}{\partial t} + jkn \frac{n_{eh1}u_{e0}}{n} \nu$$

$$(B.38)$$

Ion sound speed is defined:

$$c_s = \sqrt{\frac{KT_e + KT_i}{m_i}}$$

$$(B.39)$$

The dispersion relation of the ion acoustic wave is:

$$\omega_{IA} = kc_s$$

$$(B.40)$$

Equation B.38 can be simplified by using the ion acoustic dispersion relation:

$$\frac{\partial^2 n_{i1}}{\partial t^2} + \omega_{IA}^2 n_{i1} + \nu \frac{\partial n_{el1}}{\partial t} = jk \frac{m_e}{m_i} u_{e0} \frac{\partial n_{eh1}}{\partial t} + jkn_{eh1}u_{e0}\nu$$

$$(B.41)$$

This is a simple harmonic oscillator equation for the low frequency ion fluctuations that generate ion acoustic wave. The frequency of the ion acoustic wave is determined by the beating of the high frequency fluctuations and the pump field.

In summary, Equation B.33 and Equation B.41 are two coupled equations:

$$\frac{\partial^2 n_{eh1}}{\partial t^2} + \omega_L^2 n_{eh} + \frac{\partial n_{eh1}}{\partial t}\nu = jkn_{el1} \frac{\partial u_{e0}}{\partial t} - jkn_{el1}u_{e0}\nu$$

$$\frac{\partial^2 n_{i1}}{\partial t^2} + \omega_{IA}^2 n_{i1} + \nu \frac{\partial n_{el1}}{\partial t} = jk \frac{m_e}{m_i} u_{e0} \frac{\partial n_{eh1}}{\partial t} + jkn_{eh1}u_{e0}\nu$$

Suppose that the ion fluctuations oscillate at ω. The low frequency ion fluctuations beat with the electrons oscillating at the pump frequency, i.e. ω_0, and generates a new Langmuir wave at $\omega_L = \omega_0 - \omega$. Note that $\omega_0 + \omega$ is out of the band of the electrons. On the other hand, the high frequency Langmuir wave beats with the electrons oscillating at the pump frequency and generate an ion acoustic wave at $\omega = \omega_0 - \omega_L = \omega_0 - (\omega_0 - \omega)$. If the pump field is strong enough to overcome the damping of the Langmuir and ion acoustic waves, these new wave modes grow exponentially [*Kuo*, 2001]. Detailed calculation of the threshold excitation level is out of the scope of this Appendix and can be found in the textbooks [*Chen*, 1984].

B.2   Kinetic description of the parametric decay instability

In this section, the general dispersion relation of the parametric decay instability (Equation 4.2) in the magnetized plasma is derived using kinetic equations.

Vlasov equation describes the position and velocity of each particle and the force exerted on the particles.

$$\frac{\partial f}{\partial t} + v_j.\nabla f + \frac{q_j}{m_j}(E + v_j \times B)\frac{\partial f}{\partial v_j} = 0 \tag{B.42}$$

The electric field is a superposition of the natural fluctuations, i.e., E, and an external pump field, i.e., $E_p = E_0 cos(\omega_0 t)$. Similarly the magnetic field includes the background magnetic field (in the ionosphere the geomagnetic field), the magnetic field fluctuation due to the motion of the particles and an external pump magnetic field. The distribution function is superposition of the zeroth and the first order distribution functions, i.e. $f(r, v, t) = f_0(r, v, t) + f_1(r, v, t)$. The zeroth order distribution, f_0, is the distribution function of the charged particles, i.e. electrons and ions, in the absence of any natural fluctuation, i.e. $E = 0$. The first order distribution is due to the natural fluctuations that can interact with the external pump field and start to grow. Therefore, the general form of the Vlasov equation is:

$$\frac{\partial(f_0 + f_1)}{\partial t} + v_j.\nabla(f_0 + f_1) + \frac{q_j}{m_j}(E + E_0 cos(\omega_0 t) + v_j \times (B + B0))\frac{\partial(f_0 + f_1)}{\partial v_j} = 0 \tag{B.43}$$

This equation can be broken into two equations:

$$\frac{\partial f_0}{\partial t} + v_j.\nabla f_0 + \frac{q_j}{m_j}(E_0 cos(\omega_0 t) + v_j \times B0)\frac{\partial f_0}{\partial v_j} = 0 \tag{B.44}$$

$$\frac{\partial f_1}{\partial t} + v_j.\nabla f_1 + \frac{q_j}{m_j}(E + E_0 cos(\omega_0 t) + v_j \times (B + B_0))\frac{\partial f_1}{\partial v_j} + \frac{q_j}{m_j}(E + v_j \times B)\frac{\partial f_0}{\partial v_j} = 0 \tag{B.45}$$

The magnetic field fluctuations and the external magnetic field are much smaller than the geomagnetic field and can be neglected. We also neglect the second order terms, i.e. $(q_j/m_j)E(\partial f_1/\partial v_j)$. Thus Equation B.45 is simplified:

$$\frac{\partial f_1}{\partial t} + v_j.\nabla f_1 + \frac{q_j}{m_j}(E_0 cos(\omega_0 t) + v_j \times B_0)\frac{\partial f_1}{\partial v_j} + \frac{q_j}{m_j}E\frac{\partial f_0}{\partial v_j} = 0 \tag{B.46}$$

Equation B.44 describes gyro-motion and drift velocity of the particles due to the external pump wave. Since collision is neglected in this model and no fluctuation is considered in the

zeroth order distribution function, the trajectory of the all particles will be the trajectory of a single particle in presence of the pump field and the magnetic field. This trajectory can be obtained from the well-known Lorentz force equation. Therefore, the zeroth order trajectory of the particles is described by the following equations:

$$v_{x0j} = \frac{\omega_0 \Omega_{cj} E_{x0} cos(\omega_0 t) + \Omega_{cj}^2 E_{y0} sin(\omega_0 t)}{B_0(\Omega_{cj}^2 - \omega_0^2)}$$

$$r_{x0j} = \frac{\Omega_{cj} E_{x0} sin(\omega_0 t) - \frac{\Omega_{cj}^2}{\omega_0} E_{y0} cos(\omega_0 t)}{B_0(\Omega_{cj}^2 - \omega_0^2)}$$

$$v_{y0j} = \frac{\omega_0 \Omega_{cj} E_{y0} cos(\omega_0 t) - \Omega_{cj}^2 E_{x0} sin(\omega_0 t)}{B_0(\Omega_{cj}^2 - \omega_0^2)}$$

$$r_{y0j} = \frac{\Omega_{cj} E_{y0} sin(\omega_0 t) + \frac{\Omega_{cj}^2}{\omega_0} E_{x0} cos(\omega_0 t)}{B_0(\Omega_{cj}^2 - \omega_0^2)}$$

$$v_{z0j} = \frac{q_j}{m_j \omega_0} E_{z0} cos(\omega_0 t)$$

$$r_{z0j} = \frac{q_j}{m_j \omega_0^2} E_{z0} sin(\omega_0 t) \tag{B.47}$$

where $\Omega_{cj} = q_j B_0/m_j$. We assumed that the geomagnetic field is in the z direction, $\vec{B}_0 = B_0\vec{z}$. Equation B.46 can be written in the following form:

$$\frac{\partial f_1}{\partial t} + v_j.\nabla f_1 + \frac{q_j}{m_j}(E_0 cos(\omega_0 t) + v_j \times B_0)\frac{\partial f_1}{\partial v_j} = -\frac{q_j}{m_j}E\frac{\partial f_0}{\partial v_j} \tag{B.48}$$

If we neglect the right hand side (RHS) of the equation, it is similar to Equation B.44. It means that right hand side of the equation works as a source for generating fluctuation in the distribution function which may produce new plasma waves. Thus, we can assume that the position and velocity of the particles are superposition of the position and velocity of the particles in the absence of the drive (i.e. RHS=0) and change of the position and velocity generated by the drive (i.e. RHS). The velocity and position are described in the following form:

$$v = v + v_d$$
$$r = r + r_d \tag{B.49}$$

where v_d and r_d are the velocity and position of the particles due to the external electric field which is described in Equation B.47. Since the effect of the external electric field on the position and velocity is considered in Equation B.49, we can write the Vlasov equation in the following form which is called Vlasov equation in the oscillating frame of reference [*Porkolab*, 1974]:

$$\frac{\partial f_1(r + r_{jd}, v_j + v_{jd}, t)}{\partial t} + v_j.\nabla f_1(r + r_{jd}, v_j + v_{jd}, t) +$$

$$\frac{q_j}{m_j}(v_j \times B_0)\frac{\partial f_1(r+r_{jd}, v_j+v_{jd}, t)}{\partial v_j} = -\frac{q_j}{m_j}E\frac{\partial f_0}{\partial v_j} \tag{B.50}$$

Note that by changing the velocity and position of the particles to the oscillating frame, the effect of $E_0 cos(\omega_0 t) + v_{dj} \times B_0$ is taken into account and the $v_{jd}.\nabla f_1(r+r_{jd}, v_j+v_{jd}, t) = 0$. Therefore, in Equation B.50, outside the distribution function, the velocity is only the disturbed velocity of the particles, i.e. v_j. It is easier to solve this equation in the Fourier domain. We define the time and spatial domain Fourier transform with the $e^{-j\omega t}$ and $e^{j\vec{k}.\vec{r}}$ coefficient respectively. Thus the following conversions can be easily derived:

$$\frac{\partial f(r,v,t)}{\partial t} \rightarrow +j\omega F(r,v,\omega)$$
$$\nabla f(r,v,t) \rightarrow -j\vec{k}F(k,v,r)$$
$$\nabla f(r+r_d,v,t) \rightarrow -j\vec{k}F(k,v,r)e^{-j\vec{k}.\vec{r_d}} \tag{B.51}$$

Equation B.50 in the spatial Fourier domain is:

$$\frac{\partial F_1(\vec{k_j}, v+v_{jd}, t)}{\partial t}e^{-j\vec{k}.\vec{r_{jd}}} - j\vec{k}.\vec{v_j}F_1(\vec{k}, v+v_{jd}, t)e^{-j\vec{k}.\vec{r_{jd}}} +$$
$$\frac{q_j}{m_j}(v_j \times B_0)\frac{\partial F_1(\vec{k_j}, v+v_{jd}, t)e^{-j\vec{k}.\vec{r_{jd}}}}{\partial v_j} = -\frac{q_j}{m_j}E\frac{\partial f_0}{\partial v_j} \tag{B.52}$$

Multiplying the both sides by $e^{j\vec{k}.\vec{r_{jd}}}$ results in:

$$\frac{\partial F_1(\vec{k_j}, v+v_{jd}, t)}{\partial t} - j\vec{k}.\vec{v_j}F_1(\vec{k}, v+v_{jd}, t) +$$
$$\frac{q_j}{m_j}(v_j \times B_0)\frac{\partial F_1(\vec{k_j}, v+v_{jd}, t)}{\partial v_j} = -\frac{q_j}{m_j}E\frac{\partial f_0}{\partial v_j}e^{j\vec{k}.\vec{r_{jd}}} \tag{B.53}$$

We should calculate the $e^{j\vec{k}.\vec{r_d}}$ coefficient.

$$\vec{k}.\vec{r_{jd}} = k_x r_{jx} + k_y r_{jy} + k_z r_{jz} = k_x\frac{\Omega_{cj}E_{x0}sin(\omega_0 t) - \frac{\Omega_{cj}^2}{\omega_0}E_{y0}cos(\omega_0 t)}{B_0(\Omega_{cj}^2 - \omega_0^2)}$$
$$+k_y\frac{\Omega_{cj}E_{y0}sin(\omega_0 t) + \frac{\Omega_{cj}^2}{\omega_0}E_{x0}cos(\omega_0 t)}{B_0(\Omega_{cj}^2 - \omega_0^2)} + k_z\frac{q_j}{m_j\omega_0^2}E_{z0}sin(\omega_0 t) \tag{B.54}$$

$$\vec{k}.\vec{r_{jd}} = \frac{q_j}{m_j}\left[\left(\frac{k_z E_z}{\omega_0^2} + \frac{k_x E_x + k_y E_y}{\omega_0^2 - \Omega_{cj}^2}\right)sin(\omega_0 t) + \left(\frac{\Omega_{cj}(k_x E_y - k_y E_x)}{(\omega_0^2 - \Omega_{cj}^2)\omega_0}\right)cos(\omega_0 t)\right] \tag{B.55}$$

Using a simple expression $\mu \sin(\omega_0 t + \beta) = \mu(\cos(\beta)\sin(\omega_0 t) + \sin(\beta)\cos(\omega_0 t))$, Equation B.55 will be written in the following form:

$$\vec{k}.\vec{r_{jd}} = \mu_j \sin(\omega_0 t + \beta_j) \tag{B.56}$$

where

$$\mu_j = \frac{q_j}{m_j}\left[\left(\frac{k_z E_z}{\omega_0^2} + \frac{k_x E_x + k_y E_y}{\omega_0^2 - \Omega_{cj}^2}\right)^2 + \left(\frac{\Omega_{cj}(k_x E_y - k_y E_x)}{(\omega_0^2 - \Omega_{cj}^2)\omega_0}\right)^2\right]^{1/2} \tag{B.57}$$

and

$$\beta_j = \tan^{-1}\left(\frac{\left(\frac{\Omega_{cj}(k_x E_y - k_y E_x)}{(\omega_0^2 - \Omega_{cj}^2)\omega_0}\right)}{\left(\frac{k_z E_z}{\omega_0^2} + \frac{k_x E_x + k_y E_y}{\omega_0^2 - \Omega_{cj}^2}\right)}\right) \tag{B.58}$$

Therefore:

$$e^{j\vec{k}.\vec{r_d}} = e^{j\mu_j \sin(\omega_0 t + \beta_j)} \tag{B.59}$$

Equation B.59 can be written in the form of the Bessel function:

$$e^{j\vec{k}.\vec{r_d}} = e^{j\mu_j \sin(\omega_0 t + \beta_j)} = \sum_{n=-\infty}^{\infty} J_n(\mu_j) e^{jn(\omega_0 t + \beta_j)} \tag{B.60}$$

Equation B.60 should be exerted into Equation B.53 to enable us to solve the equation.

$$\frac{\partial F_1(\vec{k_j}, v_j + v_{jd}, t)}{\partial t} - j\vec{k}.\vec{v_j}F_1(\vec{k}, v_j + v_{jd}, t) + \frac{q_j}{m_j}(v_j \times B_0)\frac{\partial F_1(\vec{k_j}, v_j + v_{jd}, t)}{\partial v_j} =$$
$$-\frac{q_j}{m_j}E\frac{\partial f_0}{\partial v_j}\sum_{n=-\infty}^{\infty} J_n(\mu_j)e^{jn(\omega_0 t + \beta_j)} \tag{B.61}$$

If the velocity is written in the cylindrical coordinate system, the derivatives with respect to velocity are simplified as follows:

$$v = v_j = v_{j\perp}\vec{r} + v_{j\parallel}\vec{z}$$
$$\frac{\partial}{\partial v} = \frac{\partial}{\partial v_\perp}\vec{r} + \frac{1}{v_\perp}\frac{\partial}{\partial \varphi}\vec{\varphi} + \frac{\partial}{\partial v_\parallel}\vec{z} \tag{B.62}$$

Note that the perturbation generated by the electric field, changes velocity of the particle across the magnetic field in r direction and along the magnetic field in z. Using Equation B.62, the term that contain derivative with respect to v is simplified:

$$\frac{q_j}{m_j}(-v_{j\perp}B_0\vec{\varphi})$$
$$\left(\frac{\partial F_1(\vec{k_j}, v_j + v_{jd}, t)}{\partial v_\perp}\vec{r} + \frac{1}{v_{j\perp}}\frac{\partial F_1(\vec{k_j}, v_j + v_{jd}, t)}{\partial \varphi}\vec{\varphi} + \frac{\partial F_1(\vec{k_j}, v_j + v_{jd}, t)}{\partial v_\parallel}\vec{z}\right) =$$
$$\left(-\frac{q_j}{m_j}v_{j\perp}B_0\frac{1}{v_{j\perp}}\frac{\partial F_1(\vec{k_j}, v_j + v_{jd}, t)}{\partial \varphi}\right) = \left(-\Omega_{cj}\frac{\partial F_1(\vec{k_j}, v_j + v_{jd}, t)}{\partial \varphi}\right) \tag{B.63}$$

Equation B.61 can be written as follows:

$$\frac{\partial F_1(\vec{k_j}, v_j + v_{jd}, t)}{\partial \varphi} - \frac{1}{\Omega_{cj}} \frac{\partial F_1(\vec{k}, v_j + v_{jd}, t)}{\partial t} + j\frac{\vec{k}.\vec{v_j}}{\Omega_{cj}} F_1(\vec{k}, v_j + v_{jd}, t) =$$

$$\frac{q_j}{m_j} \frac{E}{\Omega_{cj}} \frac{\partial f_0}{\partial v_j} \sum_{n=-\infty}^{\infty} J_n(\mu_j) e^{jn(\omega_0 t + \beta_j)} \tag{B.64}$$

Now, we should take the time domain Fourier transform of the equation:

$$\frac{\partial F_1(\vec{k_j}, v_j + v_{jd}, \omega)}{\partial \varphi} - j\frac{\omega - \vec{k}.\vec{v_j}}{\Omega_{cj}} F_1(\vec{k}, v_j + v_{jd}, \omega) =$$

$$\sum_{n=-\infty}^{\infty} J_n(\mu_j) e^{jn\beta_j} \frac{q_j}{m_j} \frac{E(\vec{k_j}, \omega - n\omega_0)}{\Omega_{cj}} \frac{\partial f_0}{\partial v_j} \tag{B.65}$$

Note that Fourier transform of $f(t)e^{j\omega_0 t}$ is $f(\omega - \omega_0)$. Note also that the zeroth order distribution function, i.e. f_0 is only function of velocity. This is the well know differential equation $df/dx + P(x)f = Q(x)$ that can be solved using an integration factor $\int P(x)dx$. The solution is $f(x) = e^{-\int P(x)dx} \int Q(x)e^{\int P(x)dx} dx$. In Equation B.65 the integration factor is:

$$\int j(\frac{\vec{k}.\vec{v_j} - \omega}{\Omega_{cj}})d\varphi = \int j(\frac{k_\parallel v_{j\parallel} - \omega}{\Omega_{cj}} + \frac{k_\perp v_{j\perp} \cos(\varphi)}{\Omega_{cj}})d\varphi =$$

$$j(\frac{k_\parallel v_{j\parallel} - \omega}{\Omega_{cj}}\varphi + \frac{k_\perp v_{j\perp} \sin(\varphi)}{\Omega_{cj}}) = j(A_j\varphi + B_j \sin(\varphi)) \tag{B.66}$$

where $\cos(\varphi)$ considers the angle between the $\vec{k}$ and $\vec{v}$ in the cylindrical coordinate system, $A_j = \frac{k_\parallel v_{j\parallel} - \omega}{\Omega_{cj}}$ and $B_j = \frac{k_\perp v_{j\perp}}{\Omega_{cj}}$. Therefore, solution of Equation B.65 is:

$$F_1(\vec{k_j}, v_j + v_{jd}, \omega) = e^{-j(A_j\varphi + B_j \sin(\varphi))}$$

$$\int \sum_{n=-\infty}^{\infty} J_n(\mu_j) e^{jn\beta_j} \frac{q_j}{m_j} \frac{E(\vec{k_j}, \omega - n\omega_0)}{\Omega_{cj}} \frac{\partial f_0}{\partial v_j} e^{j(A_j\varphi + B_j \sin(\varphi))} d\varphi \tag{B.67}$$

Electric field is $E = -\nabla\Phi$. In the spatial Fourier domain $E = jk\Phi$. Thus Equation B.67 can be written as follows:

$$F_1(\vec{k_j}, v_j + v_{jd}, \omega) = e^{-j(A_j\varphi + B_j \sin(\varphi))}$$

$$\int \sum_{n=-\infty}^{\infty} J_n(\mu_j) e^{jn\beta_j} \frac{q_j}{m_j} \frac{jk\Phi(\vec{k_j}, \omega - n\omega_0)}{\Omega_{cj}} \frac{\partial f_0}{\partial v_j} e^{j(A_j\varphi + B_j \sin(\varphi))} d\varphi$$

$$= \frac{q_j \Phi(\vec{k_j}, \omega - n\omega_0)}{m_j\Omega_{cj}} e^{-j(A_j\varphi + B_j \sin(\varphi))}$$

$$\sum_{n=-\infty}^{\infty} J_n(\mu_j) e^{jn\beta_j} \int \left(jk\frac{\partial f_0}{\partial v_j}\right) e^{j(A_j\varphi + B_j \sin(\varphi))} d\varphi \tag{B.68}$$

Once again the exponential term should be written in the form of Bessel functions, i.e. $e^{jB_j \sin(\varphi)} = \sum\limits_{m=-\infty}^{\infty} J_m(B_j)e^{jm\varphi}$:

$$F_1(\vec{k_j}, v_j + v_{jd}, \omega) = e^{-jA_j\varphi} \sum_{l=-\infty}^{\infty} J_l(B_j)e^{-jl\varphi}$$

$$\int \sum_{n=-\infty}^{\infty} J_n(\mu_j)e^{jn\beta_j} \frac{q_j}{m_j} \frac{jk\Phi(\vec{k_j}, \omega - n\omega_0)}{\Omega_{cj}} \frac{\partial f_0}{\partial v_j} e^{jA_j\varphi} \sum_{m=-\infty}^{\infty} J_m(B_j)e^{jm\varphi} d\varphi$$

$$= \frac{q_j\Phi(\vec{k_j}, \omega - n\omega_0)}{m_j\Omega_{cj}} \sum_{l=-\infty}^{\infty} J_l(B_j)e^{-j(A_j+l\varphi)}$$

$$\sum_{n=-\infty}^{\infty} J_n(\mu_j)e^{jn\beta_j} \int \left(jk\frac{\partial f_0}{\partial v_j} \right) \sum_{m=-\infty}^{\infty} J_m(B_j)e^{j(A_j+m)\varphi} d\varphi$$

$$(B.69)$$

The integral in Equation B.69 should be calculated:

$$I_1 = \int \left(jk\frac{\partial f_0}{\partial v_j} \right) e^{jA_j\varphi} \sum_{m=-\infty}^{\infty} J_m(B_j)e^{jm\varphi} d\varphi$$

$$= \sum_{m=-\infty}^{\infty} J_m(B_j) \int \left(jk\frac{\partial f_0}{\partial v_j} \right) e^{j(A_j\varphi + m\varphi)} d\varphi$$

$$= \sum_{m=-\infty}^{\infty} J_m(B_j) \int \left(jk_\parallel \frac{\partial f_0}{\partial v_{j\parallel}} \right) e^{j(A_j+m)\varphi} d\varphi$$

$$+ \sum_{m=-\infty}^{\infty} J_m(B_j) \int \left(jk_\perp \frac{\partial f_0}{\partial v_{j\perp}} \cos(\varphi) \right) e^{j(A_j+m)\varphi} d\varphi$$

$$= \sum_{m=-\infty}^{\infty} J_m(B_j) \left(jk_\parallel \frac{\partial f_0}{\partial v_{j\parallel}} \right) \frac{1}{j(A_j+m)} e^{j(A_j+m)\varphi}$$

$$+ \sum_{m=-\infty}^{\infty} J_m(B_j) \left(jk_\perp \frac{\partial f_0}{\partial v_{j\perp}} \right) \left(\frac{e^{j(A_j+m+1)\varphi}}{j2(A_j+m+1)} + \frac{e^{j(A_j+m-1)\varphi}}{j2(A_j+m-1)} \right)$$

$$(B.70)$$

Equation B.70 should be exerted into Equation B.69:

$$F_1(\vec{k_j}, v_j + v_{jd}, \omega) = \frac{q_j\Phi(\vec{k_j}, \omega - n\omega_0)}{m_j\Omega_{cj}} \sum_{l=-\infty}^{\infty} J_l(B_j)e^{-j(A_j+l\varphi)} \sum_{n=-\infty}^{\infty} J_n(\mu_j)e^{jn\beta_j} I_1$$

$$= \frac{q_j\Phi(\vec{k_j}, \omega - n\omega_0)}{m_j\Omega_{cj}} \sum_{n=-\infty}^{\infty} J_n(\mu_j)e^{jn\beta_j} \sum_{l=-\infty}^{\infty} J_l(B_j)e^{-j(A_j+l\varphi)} I_1$$

$$= \frac{q_j\Phi(\vec{k_j}, \omega - n\omega_0)}{m_j\Omega_{cj}} \sum_{n=-\infty}^{\infty} J_n(\mu_j)e^{jn\beta_j}$$

$$\sum_{l=-\infty}^{\infty}\sum_{m=-\infty}^{\infty} J_l(B_j)e^{-j(A_j+l\varphi)}J_m(B_j)\left(jk_\parallel\frac{\partial f_0}{\partial v_{j\parallel}}\right)\frac{1}{j(A_j+m)}e^{j(A_j+m)\varphi}$$

$$+\sum_{l=-\infty}^{\infty}\sum_{m=-\infty}^{\infty} J_l(B_j)e^{-j(A_j+l\varphi)}J_m(B_j)\left(jk_\perp\frac{\partial f_0}{\partial v_{j\perp}}\right)$$

$$\left(\frac{e^{j(A_j+m+1)\varphi}}{j2(A_j+m+1)}+\frac{e^{j(A_j+m-1)\varphi}}{j2(A_j+m-1)}\right)$$

(B.71)

Equation B.71 can be written in a simpler form:

$$F_1(\vec{k_j},v_j+v_{jd},\omega)=\frac{q_j\Phi(\vec{k_j},\omega-n\omega_0)}{m_j\Omega_{cj}}\sum_{n=-\infty}^{\infty}J_n(\mu_j)e^{jn\beta_j}$$

$$\sum_{l,m=-\infty}^{\infty}J_l(B_j)J_m(B_j)\left(jk_\parallel\frac{\partial f_0}{\partial v_{j\parallel}}\right)\frac{1}{j(A_j+m)}e^{j(m-l)\varphi}$$

$$+\sum_{l,m=-\infty}^{\infty}\frac{J_l(B_j)}{2}\left(jk_\perp\frac{\partial f_0}{\partial v_{j\perp}}\right)\left(\sum_{m=-\infty}^{\infty}J_m(B_j)\frac{e^{j(m-l+1)\varphi}}{j(A_j+m+1)}+\sum_{m=-\infty}^{\infty}J_m(B_j)\frac{e^{j(m-l-1)\varphi}}{j(A_j+m-1)}\right)$$

$$=\frac{q_j\Phi(\vec{k_j},\omega-n\omega_0)}{m_j\Omega_{cj}}\sum_{n=-\infty}^{\infty}J_n(\mu_j)e^{jn\beta_j}$$

$$\sum_{l=-\infty}^{\infty}J_l(B_j)J_m(B_j)\left(jk_\parallel\frac{\partial f_0}{\partial v_{j\parallel}}\right)\frac{1}{j(A_j+m)}e^{j(m-l)\varphi}$$

$$+\sum_{l,m=-\infty}^{\infty}\frac{J_l(B_j)}{2}\left(jk_\perp\frac{\partial f_0}{\partial v_{j\perp}}\right)\left(\sum_{s=-\infty}^{\infty}J_{s-1}(B_j)\frac{e^{j(s-l)\varphi}}{j(A_j+s)}+\sum_{t=-\infty}^{\infty}J_{t+1}(B_j)\frac{e^{j(t-l)\varphi}}{j(A_j+t)}\right)$$

(B.72)

Equation B.72 can be written as follows:

$$F_1(\vec{k_j},v_j+v_{jd},\omega)=\frac{q_j\Phi(\vec{k_j},\omega-n\omega_0)}{m_j\Omega_{cj}}\sum_{n=-\infty}^{\infty}J_n(\mu_j)e^{jn\beta_j}$$

$$\sum_{l,m=-\infty}^{\infty}J_l(B_j)J_m(B_j)\left(k_\parallel\frac{\partial f_0}{\partial v_{j\parallel}}\right)\frac{1}{(A_j+m)}e^{j(m-l)\varphi}$$

$$+\sum_{l,m=-\infty}^{\infty}\frac{J_l(B_j)(J_{m-1}(B_j)+J_{m+1}(B_j))}{2}\left(k_\perp\frac{\partial f_0}{\partial v_{j\perp}}\right)\frac{e^{j(m-l)\varphi}}{(A_j+m)}$$

(B.73)

By manipulating the Bessel function using $(J_{n-1}(x)+J_{n+1}(x))=\frac{2n}{x}J_n$ we have:

$$F_1(\vec{k_j},v_j+v_{jd},\omega)=\frac{q_j\Phi(\vec{k_j},\omega-n\omega_0)}{m_j\Omega_{cj}}\sum_{n=-\infty}^{\infty}J_n(\mu_j)e^{jn\beta_j}$$

$$\sum_{l,m=-\infty}^{\infty} J_l(B_j)J_m(B_j)\left(k_\parallel \frac{\partial f_0}{\partial v_{j\parallel}}\right)\frac{1}{(A_j+m)}e^{j(m-l)\varphi}$$

$$+\sum_{l,m=-\infty}^{\infty} \frac{mJ_l(B_j)J_m(B_j)}{B_j}\left(k_\perp \frac{\partial f_0}{\partial v_{j\perp}}\right)\frac{e^{j(m-l)\varphi}}{(A_j+m)}$$

(B.74)

Equation B.74 can be written in the following simple form:

$$F_1(\vec{k_j}, v_j + v_{jd}, \omega) = \frac{q_j\Phi(\vec{k_j},\omega-n\omega_0)}{m_j\Omega_{cj}}\sum_{n=-\infty}^{\infty} J_n(\mu_j)e^{jn\beta_j}\sum_{l,m=-\infty}^{\infty} J_l(B_j)J_m(B_j)$$

$$\left(k_\parallel \frac{\partial f_0}{\partial v_{j\parallel}} + \frac{mk_\perp}{B_j}\frac{\partial f_0}{\partial v_{j\perp}}\right)\frac{e^{j(m-l)\varphi}}{A_j+m}$$

(B.75)

The charge density of each species can be obtained from the distribution function:

$$\rho_j = q_j \int F_{1j}(\vec{k_j}, v_j + v_{jd}, \omega)dv_j$$

(B.76)

Therefore:

$$\frac{\rho_j}{\epsilon_0} = \frac{q_j^2}{\epsilon_0}\int \frac{\Phi(\vec{k_j},\omega-n\omega_0)}{m_j\Omega_{cj}}\sum_{n=-\infty}^{\infty} J_n(\mu_j)e^{jn\beta_j}\sum_{l,m=-\infty}^{\infty} J_l(B_j)J_m(B_j)$$

$$\left(\frac{k_\parallel\partial f_0}{\partial v_{j\parallel}} + \frac{mk_\perp}{B_j}\frac{\partial f_0}{\partial v_{j\perp}}\right)\frac{e^{j(m-l)\varphi}}{A_j+m}dv_j$$

(B.77)

The integral is in cylindrical coordinate, i.e. $dv_j = v_\perp d\varphi dv_{j\perp}dv_{j\parallel}$. The integral over φ in the range $[0\ 2\pi]$ is zero except for $m=l$ which equals 2π. Therefore Equation B.77 is simplified as follows:

$$\frac{\rho_j}{\epsilon_0} = \frac{2\pi q_j^2\Phi(\vec{k_j},\omega-n\omega_0)}{m_j\Omega_{cj}\epsilon_0}\sum_{n=-\infty}^{\infty} J_n(\mu_j)e^{jn\beta_j}\int v_{j\perp}\sum_{m=-\infty}^{\infty} \frac{J_m^2(B_j)}{A_j+m}$$

$$\left(\frac{k_\parallel\partial f_0}{\partial v_{j\parallel}} + \frac{mk_\perp}{B_j}\frac{\partial f_0}{\partial v_{j\perp}}\right)dv_{j\parallel}dv_{j\perp}$$

(B.78)

Now we can exert the A_j and B_j into Equation B.80: $A_j = \frac{k_\parallel v_{j\parallel}-\omega_j}{\Omega_{cj}}$ and $B_j = \frac{k_\perp v_{j\perp}}{\Omega_{cj}}$

$$\frac{\rho_j}{\epsilon_0} = \frac{2\pi q_j^2\Phi(\vec{k_j},\omega-n\omega_0)}{m_j\Omega_{cj}\epsilon_0}\sum_{n=-\infty}^{\infty} J_n(\mu_j)e^{jn\beta_j}\int v_{j\perp}\sum_{m=-\infty}^{\infty} \frac{J_m^2(\frac{k_\perp v_{j\perp}}{\Omega_{cj}})}{\frac{k_\parallel v_{j\parallel}-\omega_j}{\Omega_{cj}}+m}$$

$$\left(\frac{k_\parallel\partial f_0}{\partial v_{j\parallel}} + \frac{mk_\perp\Omega_{cj}}{\frac{k_\perp v_{j\perp}}{\Omega_{cj}}}\frac{\partial f_0}{\partial v_{j\perp}}\right)dv_{j\parallel}dv_{j\perp}$$

(B.79)

In a simpler form:

$$
\frac{\rho_j}{\epsilon_0} = \sum_{n=-\infty}^{\infty} J_n(\mu_j) e^{jn\beta_j} \frac{2\pi q_j^2 \Phi(\vec{k_j}, \omega - n\omega_0)}{m_j \epsilon_0} \int v_{j\perp} \sum_{m=-\infty}^{\infty} \frac{J_m^2(\frac{k_\perp v_{j\perp}}{\Omega_{cj}})}{k_\parallel v_{j\parallel} - \omega + m\Omega_{cj}}
$$
$$
\left(\frac{k_\parallel \partial f_0}{\partial v_{j\parallel}} + \frac{m\Omega_{cj}}{v_{j\perp}} \frac{\partial f_0}{\partial v_{j\perp}} \right) dv_{j\parallel} dv_{j\perp} \tag{B.80}
$$

The susceptibility of the species j in the magnetized plasma is defined as follows:

$$
\chi_j(k, \omega) = \frac{2\pi q_j^2}{k^2 m_j \epsilon_0} \sum_{m=-\infty}^{\infty} \int J_m^2(\frac{k_\perp v_{j\perp}}{\Omega_{cj}}) \frac{\left(\frac{k_\parallel \partial f_0}{\partial v_{j\parallel}} + \frac{m\Omega_{cj}}{v_{j\perp}} \frac{\partial f_0}{\partial v_{j\perp}} \right)}{\omega - m\Omega_{cj} - k_\parallel v_{j\parallel}} v_{j\perp} dv_{j\parallel} dv_{j\perp}
$$
$$
\tag{B.81}
$$

Thus, Equation B.80 in terms of the susceptibility function is:

$$
\frac{\rho_j}{k^2 \epsilon_0} = - \sum_{n=-\infty}^{\infty} J_n(\mu_j) e^{jn\beta_j} \Phi(\vec{k_j}, \omega - n\omega_0) \chi_j(k, \omega) \tag{B.82}
$$

Equation B.82 gives charge density. In this equation, the electric potential is in the frame of oscillation. The electric potential can be found from Poisson's equation:

$$
\nabla^2 \Phi = -\frac{\rho}{\epsilon_0} \tag{B.83}
$$

The electric potential in the frame of oscillation is required to find the dispersion relation, therefore:

$$
\nabla^2 \Phi = -\frac{\rho(r + r_{jd}, t)}{\epsilon_0} \tag{B.84}
$$

In the spatial Fourier domain:

$$
-k^2 \Phi(\vec{k}, t) = - \sum_j \frac{\rho_j(\vec{k}, t)}{\epsilon_0} e^{-j\vec{k}.\vec{r_{jd}}} = - \sum_j \frac{\rho_j(\vec{k}, t)}{\epsilon_0} e^{-j\mu_j \sin(\omega_0 t + \beta_j)} \Rightarrow
$$
$$
-k^2 \Phi(\vec{k}, t) = - \sum_j \frac{\rho_j(\vec{k}, t)}{\epsilon_0} \sum_{n=-\infty}^{\infty} J_n(-\mu_j) e^{jn(\omega_0 t + \beta_j)} \tag{B.85}
$$

Now the time domain Fourier transform of the equation should be calculated:

$$
\Phi(\vec{k}, \omega) = \sum_j \sum_{n=-\infty}^{\infty} J_n(-\mu_j) e^{jn\beta_j} \frac{\rho_j(\vec{k}, \omega - n\omega_0)}{k^2 \epsilon_0} \tag{B.86}
$$

Equation B.82 and EquationB.87 form a set of coupling equations:

$$\frac{\rho_j(\vec{k},\omega)}{k^2\epsilon_0} = -\sum_{n=-\infty}^{\infty} J_n(\mu_j)e^{jn\beta_j}\Phi(\vec{k_j},\omega - n\omega_0)\chi_j(k,\omega)$$

$$\Phi(\vec{k},\omega) = \sum_j \sum_{n=-\infty}^{\infty} J_n(-\mu_j)e^{jn\beta_j}\frac{\rho_j(\vec{k},\omega - n\omega_0)}{k^2\epsilon_0} \tag{B.87}$$

These equations should be combined to find the dispersion relation. The external pump field does not affect ions significantly because of the ion inertia, thus $\mu_i = \beta_i = 0$. Equation B.87 is simplified as follows:

$$\frac{\rho_i(\vec{k},\omega)}{k^2\epsilon_0} = -\Phi(\vec{k},\omega)\chi_i(k,\omega)$$

$$\frac{\rho_e(\vec{k},\omega)}{k^2\epsilon_0} = -\sum_{m=-\infty}^{\infty} J_m(\mu_e)e^{jm\beta_e}\Phi(\vec{k},\omega - m\omega_0)\chi_e(k,\omega)$$

$$\Phi(\vec{k},\omega - m\omega_0) = \sum_{n=-\infty}^{\infty} J_n(-\mu_e)e^{jn\beta_e}\frac{\rho_e(\vec{k},\omega - (n+m)\omega_0)}{k^2\epsilon_0} + \frac{\rho_i(\vec{k},\omega - m\omega_0)}{k^2\epsilon_0} \tag{B.88}$$

Now the electric potential should be exerted into the density equations:

$$\frac{\rho_i(\vec{k},\omega)}{k^2\epsilon_0} = -\left(\sum_{n=-\infty}^{\infty} J_n(-\mu_e)e^{jn\beta_e}\frac{\rho_e(\vec{k},\omega - n\omega_0)}{k^2\epsilon_0} + \frac{\rho_i(\vec{k},\omega)}{k^2\epsilon_0}\right)\chi_i(k,\omega)$$

$$\frac{\rho_e(\vec{k},\omega)}{k^2\epsilon_0} =$$

$$-\sum_{m=-\infty}^{\infty} J_m(\mu_e)e^{jm\beta_e}\left(\sum_{n=-\infty}^{\infty} J_n(-\mu_e)e^{jn\beta_e}\frac{\rho_e(\vec{k},\omega - (n+m)\omega_0)}{k^2\epsilon_0} + \frac{\rho_i(\vec{k},\omega - m\omega_0)}{k^2\epsilon_0}\right)\chi_e(k,\omega)$$

$$\tag{B.89}$$

In the second equation, inside the parenthesis, the $m = -n$ terms should be separated from rest of the terms:

$$\frac{\rho_i(\vec{k},\omega)}{k^2\epsilon_0} = -\left(\sum_{n=-\infty}^{\infty} J_n(-\mu_e)e^{jn\beta_e}\frac{\rho_e(\vec{k},\omega - n\omega_0)}{k^2\epsilon_0} + \frac{\rho_i(\vec{k},\omega)}{k^2\epsilon_0}\right)\chi_i(k,\omega)$$

$$\frac{\rho_e(\vec{k},\omega)}{k^2\epsilon_0} = -\sum_{m=-n=-\infty}^{\infty} J_m(\mu_e)e^{jm\beta_e}J_n(-\mu_e)e^{jn\beta_e}\frac{\rho_e(\vec{k},\omega)}{k^2\epsilon_0}\chi_e(k,\omega)$$

$$-\left(\sum_{m=-\infty}^{\infty}\sum_{n=-\infty,n\neq-m}^{\infty} J_m(\mu_e)J_n(-\mu_e)e^{j(n+m)\beta_e}\frac{\rho_e(\vec{k},\omega - (n+m)\omega_0)}{k^2\epsilon_0}\chi_e(k,\omega)\right)$$

$$-\left(\sum_{n=-\infty}^{\infty} J_m(-\mu_e)e^{jm\beta_e}\frac{\rho_i(\vec{k},\omega - m\omega_0)}{k^2\epsilon_0}\chi_e(k,\omega)\right) \tag{B.90}$$

By manipulating the Bessel functions using

$$\sum_{m=-n=-\infty}^{\infty} J_m(\mu_e)e^{jm\beta_e}J_n(-\mu_e)e^{jn\beta_e} = \sum_{m=-\infty}^{\infty} J_m(\mu_e)e^{jm\beta_e}\sum_{n=-\infty}^{\infty} J_n(-\mu_e)e^{jn\beta_e}$$

$$= e^{j\mu_e \sin(\beta_e)}e^{-j\mu_e \sin(\beta_e)} = 1 \tag{B.91}$$

Equation B.90 can be simplified:

$$\frac{\rho_i(\vec{k},\omega)}{k^2\epsilon_0}\epsilon_i(\vec{k},\omega) = -\left(\sum_{n=-\infty}^{\infty} J_n(-\mu_e)e^{jn\beta_e}\frac{\rho_e(\vec{k},\omega-n\omega_0)}{k^2\epsilon_0}\chi_i(k,\omega)\right)$$

$$\frac{\rho_e(\vec{k},\omega)}{k^2\epsilon_0}\epsilon_e(\vec{k},\omega) =$$

$$-\left(\sum_{m=-\infty}^{\infty}\sum_{n=-\infty,n\neq-m}^{\infty} J_m(\mu_e)J_n(-\mu_e)e^{j(n+m)\beta_e}\frac{\rho_e(\vec{k},\omega-(n+m)\omega_0)}{k^2\epsilon_0}\chi_e(k,\omega)\right)$$

$$-\left(\sum_{m=-\infty}^{\infty} J_m(-\mu_e)e^{jm\beta_e}\frac{\rho_i(\vec{k},\omega-m\omega_0)}{k^2\epsilon_0}\chi_e(k,\omega)\right) \tag{B.92}$$

where $\epsilon_j(\vec{k},\omega) = 1 + \chi_j(\vec{k},\omega)$. In the second equation, the first parenthesis can be simplified by assuming $p = n + m$:

$$\frac{\rho_i(\vec{k},\omega)}{k^2\epsilon_0}\epsilon_i(\vec{k},\omega) = -\left(\sum_{n=-\infty}^{\infty} J_n(-\mu_e)e^{jn\beta_e}\frac{\rho_e(\vec{k},\omega-n\omega_0)}{k^2\epsilon_0}\chi_i(k,\omega)\right)$$

$$\frac{\rho_e(\vec{k},\omega)}{k^2\epsilon_0}\epsilon_e(\vec{k},\omega) =$$

$$-\left(\sum_{p=-\infty,p\neq0}^{\infty}\sum_{m=-\infty}^{\infty} J_m(\mu_e)J_{p-m}(-\mu_e)e^{jp\beta_e}\frac{\rho_e(\vec{k},\omega-p\omega_0)}{k^2\epsilon_0}\chi_e(k,\omega)\right)$$

$$-\left(\sum_{m=-\infty}^{\infty} J_m(-\mu_e)e^{jm\beta_e}\frac{\rho_i(\vec{k},\omega-m\omega_0)}{k^2\epsilon_0}\chi_e(k,\omega)\right) \tag{B.93}$$

The two summations over p and m are now independent, thus:

$$\frac{\rho_i(\vec{k},\omega)}{k^2\epsilon_0}\epsilon_i(\vec{k},\omega) = -\left(\sum_{n=-\infty}^{\infty} J_n(-\mu_e)e^{jn\beta_e}\frac{\rho_e(\vec{k},\omega-n\omega_0)}{k^2\epsilon_0}\chi_i(k,\omega)\right)$$

$$\frac{\rho_e(\vec{k},\omega)}{k^2\epsilon_0}\epsilon_e(\vec{k},\omega) =$$

$$-\left(\sum_{p=-\infty,p\neq0}^{\infty} e^{jp\beta_e}\frac{\rho_e(\vec{k},\omega-p\omega_0)}{k^2\epsilon_0}\chi_e(k,\omega)\sum_{m=-\infty}^{\infty} J_m(\mu_e)J_{p-m}(-\mu_e)\right)$$

$$-\left(\sum_{m=-\infty}^{\infty} J_m(-\mu_e)e^{jm\beta_e}\frac{\rho_i(\vec{k},\omega-m\omega_0)}{k^2\epsilon_0}\chi_e(k,\omega)\right) \tag{B.94}$$

By manipulating with the Bessel functions using $\sum_{m=-\infty}^{\infty} J_m(a) J_{p-m}(b) = J_p(a+b)$, second equation is simplified:

$$\frac{\rho_i(\vec{k},\omega)}{k^2 \epsilon_0} \epsilon_i(\vec{k},\omega) = -\left(\sum_{n=-\infty}^{\infty} J_n(-\mu_e) e^{jn\beta_e} \frac{\rho_e(\vec{k},\omega-n\omega_0)}{k^2 \epsilon_0} \chi_i(k,\omega) \right)$$

$$\frac{\rho_e(\vec{k},\omega)}{k^2 \epsilon_0} \epsilon_e(\vec{k},\omega) =$$

$$-\left(\sum_{p=-\infty, p\neq 0}^{\infty} e^{jp\beta_e} \frac{\rho_e(\vec{k},\omega-p\omega_0)}{k^2 \epsilon_0} \chi_e(k,\omega) J_p(0) \right)$$

$$-\left(\sum_{m=-\infty}^{\infty} J_m(-\mu_e) e^{jm\beta_e} \frac{\rho_i(\vec{k},\omega-m\omega_0)}{k^2 \epsilon_0} \chi_e(k,\omega) \right) \tag{B.95}$$

Since $J_n(0) = 0$ for $n \neq 0$, Equation B.96 is further simplified.

$$\frac{\rho_i(\vec{k},\omega)}{k^2 \epsilon_0} \epsilon_i(\vec{k},\omega) = -\left(\sum_{n=-\infty}^{\infty} J_n(-\mu_e) e^{jn\beta_e} \frac{\rho_e(\vec{k},\omega-n\omega_0)}{k^2 \epsilon_0} \chi_i(k,\omega) \right)$$

$$\frac{\rho_e(\vec{k},\omega)}{k^2 \epsilon_0} \epsilon_e(\vec{k},\omega) = -\left(\sum_{m=-\infty}^{\infty} J_m(-\mu_e) e^{jm\beta_e} \frac{\rho_i(\vec{k},\omega-m\omega_0)}{k^2 \epsilon_0} \chi_e(k,\omega) \right) \tag{B.96}$$

Ions cannot oscillate at harmonics of ω_0, so only the low frequency term (ω) should be retained. On the other hand, electrons can only oscillate at ω and $\omega_0 - \omega$ and rest of the harmonics are out of the allowed frequency band of the electrons. By retaining the aforementioned harmonics in Equation B.96, we have:

$$\frac{\rho_i(\vec{k},\omega)}{k^2 \epsilon_0} \epsilon_i(\vec{k},\omega) = -\left(J_0(-\mu_e) \frac{\rho_e(\vec{k},\omega)}{k^2 \epsilon_0} + J_1(-\mu_e) e^{j\beta_e} \frac{\rho_e(\vec{k},\omega-\omega_0)}{k^2 \epsilon_0} \right) \chi_i(k,\omega)$$

$$\frac{\rho_e(\vec{k},\omega)}{k^2 \epsilon_0} \epsilon_e(\vec{k},\omega) = -\left(J_0(-\mu_e) \frac{\rho_i(\vec{k},\omega)}{k^2 \epsilon_0} \chi_e(k,\omega) \right)$$

$$\frac{\rho_e(\vec{k},\omega-\omega_0)}{k^2 \epsilon_0} \epsilon_e(\vec{k},\omega-\omega_0) = -\left(J_{-1}(-\mu_e) e^{-j\beta_e} \frac{\rho_i(\vec{k},\omega)}{k^2 \epsilon_0} \chi_e(k,\omega-\omega_0) \right) \tag{B.97}$$

In Equation B.97, the second and third equations should be exerted into the first equation to obtain the dispersion relation of the parametric decay instability:

$$\frac{\rho_i(\vec{k},\omega)}{k^2 \epsilon_0} \epsilon_i(\vec{k},\omega) = \quad -\left\{ J_0(-\mu_e) \left(-J_0(-\mu_e) \frac{\rho_i(\vec{k},\omega)}{k^2 \epsilon_0} \frac{\chi_e(k,\omega)}{\epsilon_e(\vec{k},\omega)} \right) \right.$$

$$\left. + J_1(-\mu_e) e^{j\beta_e} \left(-J_{-1}(-\mu_e) e^{-j\beta_e} \frac{\rho_i(\vec{k},\omega)}{k^2 \epsilon_0} \frac{\chi_e(k,\omega-\omega_0)}{\epsilon_e(\vec{k},\omega-\omega_0)} \right) \right\} \chi_i(k,\omega) \tag{B.98}$$

Note that $J_{-1}(-\mu_e) = -J_1(-\mu_e)$. The common terms on both sides of the equation should be canceled out:

$$\frac{\epsilon_i(\vec{k},\omega)}{\chi_i(k,\omega)} = \left\{ J_0^2(-\mu_e)\frac{\chi_e(k,\omega)}{\epsilon_e(\vec{k},\omega)} + J_1^2(-\mu_e)\frac{\chi_e(k,\omega-\omega_0)}{\epsilon_e(\vec{k},\omega-\omega_0)} \right\} \tag{B.99}$$

Equation B.99 is the dispersion relation of the parametric decay instability. In the ionospheric heating experiment, the external pump electric field is relatively weak. Thus, it is reasonable to assume the weak coupling condition, i.e. $\mu_e < 1$ for which $J_0(\mu_e) \cong 1 - \mu_e^2/4$ and $J_1(\mu_e) \cong \mu_e/2$. Under the weak coupling condition, the dispersion relation is further simplified:

$$\frac{\epsilon_i(\vec{k},\omega)}{\chi_i(k,\omega)} = \left\{ (1 - \mu_e^2/4)^2\frac{\chi_e(k,\omega)}{\epsilon_e(\vec{k},\omega)} + (-\mu_e/2)^2\frac{\chi_e(k,\omega-\omega_0)}{\epsilon_e(\vec{k},\omega-\omega_0)} \right\} \tag{B.100}$$

If only terms of order μ_e^2 are retained, Equation B.101 can be written as follows:

$$\frac{\epsilon_i(\vec{k},\omega)}{\chi_i(k,\omega)} = \left\{ (1 - \frac{\mu_e^2}{2})\frac{\chi_e(k,\omega)}{\epsilon_e(\vec{k},\omega)} + \frac{\mu_e^2}{4}\frac{\chi_e(k,\omega-\omega_0)}{\epsilon_e(\vec{k},\omega-\omega_0)} \right\}$$

$$\frac{\epsilon_i(\vec{k},\omega)}{\chi_i(k,\omega)} - \frac{\chi_e(k,\omega)}{\epsilon_e(\vec{k},\omega)} = \frac{\mu_e^2}{4}\left(-2\frac{\chi_e(k,\omega)}{\epsilon_e(\vec{k},\omega)} + \frac{\chi_e(k,\omega-\omega_0)}{\epsilon_e(\vec{k},\omega-\omega_0)} \right)$$

$$\frac{\epsilon_i(\vec{k},\omega)\epsilon_e(\vec{k},\omega) - \chi_i(k,\omega)\chi_e(k,\omega)}{\chi_i(k,\omega)\epsilon_e(\vec{k},\omega)} = \frac{\mu_e^2}{4}\left(\frac{\chi_e(k,\omega-\omega_0)\epsilon_e(\vec{k},\omega) - 2\chi_e(k,\omega)\epsilon_e(\vec{k},\omega-\omega_0)}{\epsilon_e(\vec{k},\omega)\epsilon_e(\vec{k},\omega-\omega_0)} \right)$$

$$\frac{\epsilon_i(\vec{k},\omega)\epsilon_e(\vec{k},\omega) - \chi_i(k,\omega)\chi_e(k,\omega)}{\chi_i(k,\omega)} = \frac{\mu_e^2}{4}\left(\frac{\chi_e(k,\omega-\omega_0)\epsilon_e(\vec{k},\omega) - 2\chi_e(k,\omega)\epsilon_e(\vec{k},\omega-\omega_0)}{\epsilon_e(\vec{k},\omega-\omega_0)} \right)$$

$$\tag{B.101}$$

Now $\epsilon_j(\vec{k},\omega) = 1 + \chi_i(k,\omega)$ should be exerted into Equation B.101:

$$\left(1 + \chi_i(\vec{k},\omega)\right)\left(1 + \chi_e(\vec{k},\omega)\right) - \chi_i(k,\omega)\chi_e(k,\omega) =$$
$$\frac{\mu_e^2}{4}\left(\frac{\chi_e(k,\omega-\omega_0)\epsilon_e(\vec{k},\omega) - 2\chi_e(k,\omega)\epsilon_e(\vec{k},\omega-\omega_0) - 2\epsilon_e(\vec{k},\omega-\omega_0) + 2\epsilon_e(\vec{k},\omega-\omega_0)}{\epsilon_e(\vec{k},\omega-\omega_0)} \right)$$

$$\left(1 + \chi_i(\vec{k},\omega) + \chi_e(\vec{k},\omega)\right) =$$
$$\frac{\mu_e^2}{4}\left(2 - \frac{-\chi_e(k,\omega-\omega_0)\epsilon_e(\vec{k},\omega) + 2\epsilon_e(\vec{k},\omega-\omega_0)(1 + \chi_e(k,\omega))}{\epsilon_e(\vec{k},\omega-\omega_0)} \right) \tag{B.102}$$

If we define $\epsilon(\vec{k}, \omega) = 1 + \chi_i(\vec{k}, \omega) + \chi_e(\vec{k}, \omega)$ and again use $\epsilon_j(\vec{k}, \omega) = 1 + \chi_j(k, \omega)$, Equation B.102 can be written in the following form:

$$\epsilon(\vec{k}, \omega) = \frac{\mu_e^2}{4} \left(2 - \frac{-\chi_e(k, \omega - \omega_0)\epsilon_e(\vec{k}, \omega) + 2\epsilon_e(\vec{k}, \omega - \omega_0)\epsilon_e(k, \omega)}{\epsilon_e(\vec{k}, \omega - \omega_0)} \right)$$

$$\epsilon(\vec{k}, \omega) = \frac{\mu_e^2}{4} \left(2 - \frac{(1 - \epsilon_e(k, \omega - \omega_0))\,\epsilon_e(\vec{k}, \omega) + 2\epsilon_e(\vec{k}, \omega - \omega_0)\epsilon_e(k, \omega)}{\epsilon_e(\vec{k}, \omega - \omega_0)} \right)$$

$$\epsilon(\vec{k}, \omega) = \frac{\mu_e^2}{4} \left(2 - \frac{\left(\epsilon_e(\vec{k}, \omega) + \epsilon_e(\vec{k}, \omega)\epsilon_e(k, \omega - \omega_0) \right)}{\epsilon_e(\vec{k}, \omega - \omega_0)} \right)$$

$$\epsilon(\vec{k}, \omega) = \frac{\mu_e^2}{4} \left(2 - \epsilon_e(\vec{k}, \omega) - \frac{\epsilon_e(\vec{k}, \omega)}{\epsilon_e(\vec{k}, \omega - \omega_0)} \right) \tag{B.103}$$

$\epsilon_e(\vec{k}, \omega)$ can be neglected because $\epsilon_e(\vec{k}, \omega) < \frac{\epsilon_e(\vec{k}, \omega)}{\epsilon_e(\vec{k}, \omega - \omega_0)}$, thus the dispersion relation (Equation B.103) can be written in the following form:

$$\epsilon(\vec{k}, \omega) - \frac{\mu_e^2}{4} \left(\frac{\epsilon_e(\vec{k}, \omega)}{\epsilon_e(\vec{k}, \omega - \omega_0)} - 2 \right) = 0 \tag{B.104}$$

where:

$$\mu_e = \frac{q_e}{m_e} \left[\left(\frac{k_z E_z}{\omega_0^2} + \frac{k_x E_x + k_y E_y}{\omega_0^2 - \Omega_{ce}^2} \right)^2 + \left(\frac{\Omega_{ce}(k_x E_y - k_y E_x)}{(\omega_0^2 - \Omega_{ce}^2)\omega_0} \right)^2 \right]^{1/2} \tag{B.105}$$

This is in fact Equation 4.2 that was used to calculate the IB and IA parametric decay instability [*Aliev and Silin*, 1965; *Amano and Okamato*, 1969; *Porkolab*, 1972; 1974; *Gurevich*, 1978].

Bibliography

[1] Aliev, Yu. M., and V. P. Silin (1965), Plasma oscillations in a high-frequency electric field, *J. Theoret. Phys., 48*, 901-912.

[2] Amano, T. and M. Okamoto (1969), Parametric Effects of an Alternating Field on Inhomogeneous Plasmas, *J. Phys. Soc. Japan, 26*, 2, 529.

[3] André, M. (1985), Dispersion surfaces, *Journal of Plasma Physics, 33* 1-19 doi:10.1017/S0022377800002270.

[4] Bailey, V. A., and D. F. Martyn (1934), Interaction of Radio Waves, *Nature , 133*, 218-218, doi:10.1038/133218a0.

[5] Bernhardt, P. A., L. M. Duncan, and C. A. Tepley (1989a), Artificial Airglow Excited by High-Power Radio Waves (1988), *Science, 18*, 242, 4881, 1022-1027, DOI: 10.1126/science.242.4881.1022.

[6] Bernhardt, P. A., L. M. Duncan, and C. A. Tepley (1989a), Heater-induced cavities as optical tracers of plasma drifts, *J. Geophys. Res., 94*(A6), 7003-7010, doi:10.1029/JA094iA06p07003.

[7] Bernhardt, P. A., C. A. Tepley, and L. M. Duncan (1989b), Airglow enhancements associated with plasma cavities formed during Ionospheric Heating Experiments, *J. Geophys. Res., 94*(A7), 9071-9092, doi:10.1029/JA094iA07p09071.

[8] Bernhardt, P. A., L. S. Wagner, J. A. Goldstein, V. Yu. Trakhtengerts, E. N. Ermakova, V. O. Rapoport, G. P. Komrakov, and A. M. Babichneko (1994), Enhancement of stimulated electromagnetic emission during two frequency ionospheric heating experiments, *Phys. Rev. Lett., 72*, 18, 2879-2882, doi:10.1103/PhysRevLett.72.2879.

[9] Bernhardt, P. A., C. A. Selcher, R.H. Lehmberg, J. Rodriguez, J. Thomason, M. McCarrick, and G. Frazer (2009), Determination of the electron temperature in the modified ionosphere over HAARP using the HF pumped stimulated Brillouin scatter (SBS) emmision lines , *Ann. Geophys., 27*, 4409-4427, doi:10.5194/angeo-27-4409-2009.

[10] Bernhardt, P. A., C. A. Selcher, R. H. Lehmberg, S. P. Rodriguez, J. F. Thomason, K. M. Groves, M. J. McCarrick, and G. J. Frazer (2010), Stimulated Brillouin Scatter in a Magnetized Ionospheric Plasma , *Phys. Rev. Lett., 104*, 16, 165004, doi:10.1103/PhysRevLett.104.165004.

[11] Bernhardt, P. A., C. Selcher, and S. Kowtha (2011), Electron and ion Bernstein wave excited in the ionosphere by high power EM waves at the second harmonic of the electron cyclotron frequency, *Geophys. Res. Lett., 38*, L19107, doi:10.1029/2011GL049390

[12] Bernhardt, P. A., S. J. Briczinski, C. L. Siefring, S. M. Han, T. Pedersen, W. A. Scales, H. Fu, A. Mahmoudian, A. Samimi, E. G. Kendall, R. Marshall, B. Watkins, (2013), Artificial Interactions in the High Latitude Ionosphere, *Proceedings of the RF Ionospheric Interactions Workshop,* Arecibo, Puerto Rico.

[13] Birdsall, C. K. and A. B. Langdon (1991), *Plasma physics via computer simulation*, New York.

[14] Bordikar M. R., W. A. Scales, A. R. Samimi, P. A. Bernhardt, S. Brizcinski, and M. J. McCarrick (2013), First observations of minority ion (H+) structuring in stimulated radiation during second electron gyroharmonic heating experiments, *Geophys. Res. Lett., 40*, 1479-1483, doi:10.1002/grl.50327.

[15] Bordikar, M. R., W. A. Scales, A. Mahmoudian, H. Kim, P. A. Bernhardt, R. Redmon, A. Samimi, S. Brizcinski, and M. J. McCarrick (2013), Impact of active geomagnetic conditions on stimulated radiation during ionospheric second electron gyro-harmonic heating, Submitted to *J. Geophys. Res.*

[16] Budden, K. G.,(1966), Radio waves in the ionosphere, *Cambridge University Press,* New York.

[17] Buchsbaum, S. J. (1960), Resonance in a plasma with two ion species, *Phys. Fluids, 3*, 418-420, doi:10.1063/1.1706052.

[18] Chen, F. F.,(1984), Introduction to plasma physics and controlled fusion. Volume 1, Plasma physics, *Springer, 2nd* edition.

[19] Das, A. C., and J. A. Fejer (1979), Resonance Instability of Small-Scale Field-Aligned Irregularities, *J. Geophys. Res., 84*, (A11), 6701-6704, doi:10.1029/JA084iA11p06701.

[20] DuBois, D. F., H. A. Rose, and D. Russell (1990), Excitation of strong Langmuir turbulence in plasmas near critical density: Application to HF heating of the ionosphere, *J. Geophys. Res., 95*(A12), 2122121272, doi:10.1029/JA095iA12p21221.

[21] DuBois, D. F., A. Hansen, H. A. Rose, and D. Russell (1993), Excitation of strong Langmuir turbulence in the ionosphere: Comparison of theory and observations@f, *Phys. Fluids, B*5, 2616, DOI:10.1063/1.860699

[22] Dysthe, K. B., E. Mjølhus, H. Pécseli and K. Rypdal (1982), Thermal Cavitons, *Phys. Scr., 26*, 548 doi:10.1088/0031-8949/1982/T2B/040.

[23] Dysthe, K. B., E. Mjølhus, H. L. Pécseli, and K. Rypdal (1983), A thermal oscillating two-stream instability, *Phys. Fluids, 26*, 146, doi: http://dx.doi.org/10.1063/1.863993.

[24] Fialer, P. A. (1974), Field-aligned scattering from a heated region of the ionosphere-observations at HF and VHF, *Radio Sci., 9*, (11), 923-940, doi:10.1029/RS009i011p00923.

[25] Förstrling, K (1942), Über die Ausbreitung Elelctromagnetischer Wellen in einem Magnetisierten Medium bei Senkrechter Incidencz, *Hochfr. Elek. 59*, 10-22.

[26] Fu, H., W. A. Scales, P. A. Bernhardt, A. Samimi, A. Mahmoudian, S.J. Briczinski and M. McCarrick (2013), Stimulated Brillouin Scatter and Stimulated Ion Bernstein Scatter During Electron Gyro-harmonic Heating Experiments, submitted to *Radio Sci.*

[27] Grach, S. M., A. N. Karashtin, N. A. Mityzkov, V. O. Rapoport,and V. Y. Trakhtengerts (1978), Theory of thermal parametric instability in an inhomogenous plasma, *Sov. J. Plasma Phys., Engl. Transl. 4*, 4, 737-741.

[28] Grach, S. (1979), Thermal parametric instability in ionospheric plasma at frequencies close to ω_{He} and $2\omega_{He}$, *Radiophys. Quantum Electron., English Transl. 22*, 357.

[29] Grach, S. M., E. S. Sergeev, A. V. Shindin, E. V. Mishin, P. A. Bernhardt, S. J. Briczinski, C. Selcher, M. Broughton (2012), Results of SEE observations and probing wave sounding at HAARP in March-April 2011, *RF ionospheric interaction workshop, Santa Fe.*

[30] Gordon, W. E., and H. C. Carlson Jr. (1974), Arecibo heating experiments, *Radio Sci. 9*(11), 1041-1047, doi:10.1029/RS009i011p01041.

[31] Gurevich, A. V. (1978), Nonlinear phenomena in the ionosphere, *Radio Sci. 9*(11), New York, Springer-Verlag New York, Inc. (Physics and Chemistry in Space. Volume 10), 1978. 380 p. Translation.

[32] Gurevich, A.V., (2007), Nonlinear effects in the ionosphere, *Phys.-Usp., 50* 1091 doi:10.1070/PU2007v050n11ABEH006212.

[33] Gustavsson, B. and Leyser, T. B. and Kosch, M. and Rietveld, M. T. and Steen, Å. and Brändström, B. U. E. and Aso, T. (2006), Electron Gyroharmonic Effects in Ionization and Electron Acceleration during High-Frequency Pumping in the Ionosphere, *Phys. Rev. Lett. 97*, 19, 195002, doi: 10.1103/PhysRevLett.97.195002.

[34] Haslett, J. C., and L. R. Megill (1974), A model of the enhanced airglow excited by RF radiation, *Radio Sci., 9* (11), 1005-1019, doi:10.1029/RS009i011p01005.

[35] Honary, F., A. J. Stocker, T. R. Robinson, T. B. Jones, and P. Stubbe (1995), Ionospheric plasma response to HF radio waves operating at frequencies close to the third harmonic of the electron gyrofrequency, *J. Geophys. Res., 100*(A11), 21489-21501, doi:10.1029/95JA02098.

[36] Honary, F., Robinson, T. R., Wright, D. M., Stocker, A. J., Rietveld, M. T., and McCrea, I. (1999), Letter to the Editor: First direct observations of the reduced striations at pump frequencies close to the electron gyroharmonics, *Ann. Geophys., 17*, 1235-1238, doi:10.1007/s00585-999-1235-6, 1999.

[37] Isham, B., W. Birkmayer, T. Hagfors, and W. Kofman (1987), Observations of small-scale plasma density depletions in Arecibo HF Heating Experiments, *J. Geophys. Res., 92*(A5), 4629-4637, doi:10.1029/JA092iA05p04629.

[38] Huang, J. and S. P. Kuo (1994), Cyclotron harmonic effect on the thermal oscillating two-stream instability in the high latitude ionosphere, *J. Geophys. Res. 99*, A2, 2173-2181, doi:10.1029/93JA02668.

[39] Huang, J., and S. P. Kuo (1994), A theoretical model for the broad upshifted maximum in the stimulated electromagnetic emission spectrum, *J. Geophys. Res., 99*(A10), 19569-19576, doi:10.1029/94JA01261.

[40] Huang, J., and S. P. Kuo (1995), A Generation Mechanism for the Downshifted Peak in Stimulated Electromagnetic Emission Spectrum, *J. Geophys. Res. 100*, A11, 21,433-21,438, doi:10.1029/95JA02302.

[41] Hussein, A. A. (1997), Simulation Studies of Parametric Processes Associated with Ionospheric Stimulated Electromagnetic Radiation, *PhD dissertation*, Virginia Tech.

[42] Hussein, A. A., and W. A. Scales (1997), Simulation studies of parametric decay processes associated with ionospheric stimulated radiation, *Radio Sci. 32*, 5, 2099-2107, doi:10.1029/97RS01349.

[43] Hussein, A. A., W. A. Scales, and J. Huang (1998), Theoretical and simulation studies of broad up-shifted sideband generation in ionospheric stimulated radiation, *Geophys. Res. Lett. 25*, (7), doi:10.1029/98GL50568.

[44] Hysell, D. L., and E. Nossa (2009), Artificial E region field-aligned plasma irregularities generated at pump frequencies near the second electron gyroharmonic, *Ann. Geophys. 27*, 2711-2720.

[45] Hysell, D. L., E. Nossa, and M. McCarrick (2010), Excitation threshold and gyroharmonic suppression of artificial E region field-aligned plasma density irregularities, *Radio Sci. 45*, RS6003, doi:10.1029/2010RS004360.

[46] Inhester, B. (1982), Thermal modulation of the plasma density in ionospheric heating experiments, *J. Atmos. Terr. 44*, 12, 21,1049-1059, doi:10.1016/0021-9169(82)90017-4.

[47] Kindel, J. M. and C. F. Kennel (1971), Topside current instabilities, *J. Geophys. Res.*, *76* 13, 3055-3078, doi:10.1029/JA076i013p03055.

[48] Kosch, M. J., Pedersen, T., Hughes, J., Marshall, R., Gerken, E., Senior, A., Sentman, D., McCarrick, M., and Djuth, F. T.: Artificial optical emissions at HAARP for pump frequencies near the third and second electron gyro-harmonic, *Ann. Geophys.*, *23*, 1585-1592, doi:10.5194/angeo-23-1585-2005, 2005.

[49] Kosch, M. J., T. Pedersen, E. Mishin, S. Oyama, J. Hughes, A. Senior, B. Watkins, and B. Bristow (2007), Coordinated optical and radar observations of ionospheric pumping for a frequency pass through the second electron gyroharmonic at HAARP, *J. Geophys. Res.*, *112* , A06325, doi:10.1029/2006JA012146.

[50] Leyser, T. B., B. Thidé, H. Derblom, , Å. Hedberg, B. Lundborg, P. Stubbe, and H. Kopka (1990), Dependence of stimulated electromagnetic emission on the ionosphere and pump wave, *J. Geophys. Res., 95*, (A10), 17,233-17,244, doi:10.1029/JA095iA10p17233.

[51] Leyser, T. B. (1991), Parametric interaction between upper hybrid and lower hybrid waves in heating experiments, *Geophys. Res. Lett., 18*, 3, 408-411, doi:10.1029/91GL00136.

[52] Leyser, T. B., B. Thidé, S. Goodman, M. Waldenvik, E. Veszelei, S. M. Grach, A. N. Karashtin,G. P. Komrakov, and D. S. Kotik (1992), Narrow cyclotron harmonic absorption resonances of stimulated electromagnetic emission in the ionosphere, *Phys. Rev. Lett., 68*, 22, 3299-3302, doi:10.1103/PhysRevLett.68.3299.

[53] Leyser, T. B. (2001), Stimulated electromagnetic emission by high-frequency electromagnetic pumping of the ionospheric plasma, *Space Science Reviews, 98*, 223-328, doi:10.1023/A:1013875603938.

[54] Lundborg, B., and B. Thidé (1985), Standing wave pattern of HF radio waves in the ionospheric reflection region 1. General formulas, *Radio Sci., 20*, 4, 947-957, doi:10.1029/RS020i004p00947.

[55] Lundborg, B., and B. Thidé (1986), Standing wave pattern of HF radio waves in the ionospheric reflection region 2. Applications, *Radio Sci., 21*, 3, 486-500, doi:10.1029/RS021i003p00486.

[56] Mahmoudian, A., W. A. Scales, P.A. Bernhardt, A. Samimi, E. Kendall, J. M. Ruohoniemi, B. Isham and M. Bordikar (2013), Ion gyro-harmonic structuring in the stimulated radiation spectrum and optical emissions during electron gyro-harmonic heating, *J. Geophys. Res., Space Physics,*, doi: 10.1002/jgra.50167

[57] Mishin, E., T. Hagfors, B. Isham (2001), A generation mechanism for topside enhanced incoherent backscatter during high frequency modification experiments in Tromsø, *Geophys. Res. Lett., 28*, 3, DOI: 10.1029/2000GL000122.

[58] Newman, D. L., R. M. Winglee, P. A. Robinson, J. Glanz, and M. V. Goldman (1990), Simulation of the collapse and dissipation of Langmuir wave packets, *Phys. Fluids, B 2*, 2600, DOI:10.1063/1.859385

[59] Nicholson, D. R. and and M. V. Goldman (1978), Cascade and collapse of Langmuir waves in two dimensions, *Phys. Fluids, 21*, 1766, DOI:10.1063/1.862093.

[60] Norin, L., T. B. Leyser, E. Nordblad, B. Thidé, and M. McCarrick (2009), Unprecedentedly Strong and Narrow Electromagnetic Emissions Stimulated by High-Frequency Radio Waves in the Ionosphere, *Phys. Rev. Lett., 102*, 6, 065003, doi:10.1103/PhysRevLett.102.065003.

[61] Pedersen, T., B. Gustavsson, E. Mishin, E. Kendall, T. Mills, H. C. Carlson, and A. L. Snyder (2010), Creation of artificial ionospheric layers using high-power HF waves, *Geophys. Res. Lett., 102*, 37, L02106, doi:10.1029/2009GL041895.

[62] Pedersen, T., M. McCarrick, B. Reinisch, B. Watkins, R. Hamel, and V. Paznukhov (2011), Production of artificial ionospheric layers by frequency sweeping near the 2nd gyroharmonic, *Ann. Geophys., 102*, 29, 47-51, doi:10.5194/angeo-29-47-2011.

[63] Porkolab, M. (1972), Parametric instabilities in a magnetic field and possible applications to heating of plasmas, *Nucl. Fusion, 12* 329 doi:10.1088/0029-5515/12/3/007.

[64] Porkolab, M. (1974), Theory of parametric instability near the lower-hybrid frequency, *Phys. Fluids, 17*, 1432-1442, doi:10.1063/1.1694910.

[65] Robinson, T. R.,(1989) The heating of the high latitude ionosphere by high power radio waves, *Physics Reports, 179*, Issues 2-3, 79-209, ISSN 0370-1573, doi:10.1016/0370-1573(89)90005-7.

[66] Samimi, A., Scales, W. A., Bernhardt, P. A., Briczinski, S. J., Selcher, C. A., and McCarrick, M. J., (2012) On ion gyro-harmonic structuring in the stimulated electromagnetic emission spectrum during second electron gyro-harmonic heating, *Ann. Geophys., 30*, 1587-1594, doi:10.5194/angeo-30-1587-2012.

[67] Samimi, A., W. A. Scales, H. Fu, P. A. Bernhardt, S. J. Briczinski, and M. J. McCarrick (2013), Ion gyroharmonic structures in stimulated radiation during second electron gyroharmonic heating: 1. Theory, *J. Geophys. Res: Space Physics, 118*, doi:10.1029/2012JA018146.

[68] Scales, W. A., K. T. Cheng, S. Srivastava (1997) Simulation studies of processes associated with stimulated electromagnetic emission (SEE) in the ionosphere, *J. of Atmospheric and Solar-Terrestrial Phys., 59*, 8, 2373-2381, ISSN 1364-6826, 10.1016/S1364-6826(96)00131-9.

[69] Scales, W. A., and H. Xi (1974), Theoretical and Numerical Simulation Investigation of Parametric Processes Associated with Up-shifted Ionospheric Stimulated Radiation, *Phys. Scr., 184*, doi:10.1238/Physica.Topical.084a00184

[70] Scales, W. A., M. R. Bordikar, A. Samimi, P. A. Bernhardt, S. Briczinski, C. A. Selcher, and M. McCarrick (2011), Observations and theory of ion gyro-harmonic structures in the stimulated radiation spectrum during second electron gyro-harmonic heating, *General Assembly and Scientific Symposium, URSI*, doi:10.1109/URSIGASS.2011.6051126.

[71] Sipler, D. P., and M. A. Biondi (1972), Measurements of O(1D) quenching rate in the F region, *J. Geophys. Res., 77*, 6202-6212.

[72] Sharma, R. P., A. Kumar, and R. Kumar (1993), Excitation of ion-Bernstein waves in ionospheric modification experiment, *Radio Sci. 28*, 6, 951-957, doi:10.1029/93RS01374.

[73] Stenflo, L., and J. Trulsen (1978), Stimulated Resonance Line Scattering in the Ionosphere, *J. Geophys. Res., 83*(A3), 1154, doi:10.1029/JA083iA03p01154.

[74] Stenflo, L. (1999), Theory of stimulated scattering of large-amplitude waves, *J. Plasma Phys. 61*, pp 129-134, doi: http://dx.doi.org/

[75] Stubbe, P., H. Kopka, B. Thidé, and H. Derblom (1984), Stimulated electromagnetic emission: A new technique to study the parametric decay instability in the ionosphere, *J. Geophys. Res., 89*(A9), 7523-7536, doi:10.1029/JA089iA09p07523.

[76] Tellegen, B. D. H., (1933) Interaction between Radio-Waves?, *Nature, 131*, 840, doi:10.1038/131840a0.

[77] Tereshchenko, E. D., R. Yu. Yurik, B. Z. Khudukon, M. T. Rietveld, B. Isham, V. Belyey, A. Brekke, T. Hagfors, and M. Grill (2006), Directional features of the downshifted peak observed in HF-induced stimulated electromagnetic emission spectra obtained using an interferometer, *Ann. Geophys., 61*, 24, 1819-1827, doi:10.5194/angeo-24-1819-2006.

[78] Thidé, B., H. Kopka, and P. Stubbe (1982), Observation of stimulated scattering of a strong high frequency radio wave in the ionosphere, *Phys. Rev. Lett., 49*, 1561-1564, doi:10.1103/PhysRevLett.49.1561.

[79] Vahedi, V. and M. Surendra (1995), A Monte Carlo collision model for the particle-in-cell method: applications to argon and oxygen discharges, *Computer Physics Communications, 87*, 1-2, 179-198, http://dx.doi.org/10.1016/0010-4655(94)00171-W.

[80] Vaskov, V. V., and A. V. Gurevich (1977), Resonance instability of small-scale plasma perturbations, *Sov. Phys. JETP Engl. Trans., 46*, 487.

[81] Weatherall, J. C., J. P. Sheerin, D. R. Nicholson, G. L. Payne, M. V. Goldman, and P. J. Hansen (1982), Solitons and ionospheric heating, *J. Geophys. Res., 87*, (A2), 823832, doi:10.1029/JA087iA02p00823.

[82] Xi, H. and W. A. Scales (2001), Numerical simulation studies on the broad upshifted maximum of ionospheric stimulated electromagnetic emission, *J. Geophys. Res., 106* (A7), 12, doi:10.1029/2000JA000322.

[83] Zhou, H. L. , J. Huang, and S. P. Kuo (1994), Cascading of the upper hybrid/electron Bernstein wave in ionospheric heating experiments, *Phys. Plasmas, 1*, 9, 3044-3052, doi:http://dx.doi.org/10.1063/1.870929.